Doctoral Dissertation
Doctoral Program in Mechanical Engineering (35th Cycle)

Electric kick scooter assessment from vehicle dynamics to rider perspective

Angelo Domenico Vella

******

Supervisor:
Prof. Alessandro Vigliani

Doctoral Examination Committee:
Prof. Michele Vignati, Referee, Politecnico di Milano
Prof. Francesca Garescì, Referee, Università degli Studi di Messina
Prof. Silvio Sorrentino, Università degli Studi di Modena e Reggio Emilia
Prof. Stefano Mauro, Politecnico di Torino
Prof. Giovanni Bracco, Politecnico di Torino

Politecnico di Torino
2023

Declaration

I hereby declare that the contents and organization of this dissertation constitute my own original work and does not compromise in any way the rights of third parties, including those relating to the security of personal data.

Angelo Domenico Vella

05/05/2023

* This dissertation is presented in partial fulfilment of the requirements for **Ph.D. degree** in the Graduate School of Politecnico di Torino (ScuDo).

Abstract

In the last years, urban mobility has been globally forced towards the reduction of vehicles powered by fossil fuels. The target pursued by governments through driving restrictions is to limit pollutants, greenhouse-gas emission and traffic congestion. Incentive programmes and sharing mobility services have meanwhile encouraged the quick spread of a new category of urban vehicle, i.e., the electric micro-vehicles. This segment, which is extremely suitable for short urban travels of single road users, is undoubtedly driven in popularity by electric kick scooters. The main peculiarities which distinguish electric kick scooters from other motorized two-wheeled vehicles stand in the small mass and the standing position of the driver. Since the advent of these vehicles on the market is quite recent, scientific research aiming at assessing their dynamics and targeting safety and comfort improvements is still in development.

The purpose of this PhD project is to enhance the knowledge of electric kick scooters focusing on the longitudinal and the vertical dynamics, with a special emphasis on comfort and vehicle-rider interaction. Two commercial vehicles characterised by different design solutions (dimensions, motor, braking system, suspensions, tyres) are considered. Their main technical specifications are collected, and the unknown parameters related to vehicle inertias and tyre characteristics are evaluated, adapting well known methodologies. On-road tests are carried out to assess the performance in longitudinal manoeuvres such as standing start, braking and coasting. Operating parameters such as the tyre pressure and the motor settings are varied during the tests. Lumped parameter models are developed and validated on the basis of the experimental evidence in order to highlight the rider influence during the standing start and the braking manoeuvres.

A comparison between the two vehicles focused on comfort analysis is carried out in a second experimental campaign driving on artificial bumps and homogeneous surfaces (asphalt and pavé) at several constant velocities. Tests on the bumps are repeated by a sample of fourteen riders, monitoring the kinematics of the main human body segments and statistically evaluating the vibration transmissibility from vehicle to driver. A detailed multibody model is finally developed to analyse the human body response in heavy braking and driving on uneven roads.

Contents

List of Figures

List of Tables

Chapter 1

Introduction

The trend towards light, more affordable and eco-friendly vehicles has led to the recent spread of a new segment in the urban mobility framework, i.e., the electric personal mobility vehicles (e-PMVs) [1–3]. Electric kick scooters (e-scooters) and electric bikes (e-bikes) are just two examples of a wide variety of vehicle belonging to this category. As underlined by e-PMV acronym, they are all designed for the transportation of a single person. An alternative way of referring to e-PMV strengthening their small dimensions is electric micro-vehicle (e-MV). Many topological aspects differentiate e-PMVs from each other, among which the most important is the rider posture. On the other hand, the common characteristics consist of the extreme compactness and the integration of an electric wheel motor which serves to partially or fully assist the ride. The compact size, guaranteed also by the presence of small wheels, is often combined with the possibility to fold the vehicle into itself, simplifying the portability and the storage in limited spaces. Among this segment, e-scooters have undoubtedly experienced the largest popularity. The reasons at the basis of the widespread of micro-vehicles and mostly e-scooters are connected to a large number of aspects which characterise the current urban mobility framework and its evolution [4].

In the last decade, the deep urbanisation has brought out the so called first and last mile problem, which is related to the distance to reach the closer transportation stations (bus, train, ferry) from the house and the workplace. Generally speaking, the “first and last mile gap” groups all the distances which are too long to be walked but too short to justify the usage of a car. One of the

advantages of e-scooters is their capability to smoothen this issue since they can be easily integrated with the public transport [5,6]. The idea of a transportation service as a multimodal journey relying on Internet-based technologies is commonly named Mobility-as-a-Service (MaaS) [7]. Another general leading factor for e-PMVs is the effort towards the reduction of urban congestion and environmental problems caused by the fossil fuel-powered vehicles (pollutions and greenhouse gases): many countries are encouraging alternative transportation systems through incentive policies and new infrastructures. The environmental impact and the potential benefits of e-PMVs in terms of global warming and air quality in big cities have been already investigated and presented [8–11]. The final overtaking of e-scooters with respect to other e-PMVs occurred when dock-less sharing services have been integrated in the urban mobility system. As already occurred with shared cars and mopeds, the first e-scooter rental service in the world started in 2017 in the United States [12,13]. It is estimated that the number of trips in the first year was 38.5 million [14] involving more than 100 cities and 85000 shared vehicles [15]. Following the US example, the introduction of shared e-scooters into European metropolises started in 2018 [1]. The strength of dock-less service consists of providing the possibility to rent, pick up and drop off a vehicle by a mobile application, with low fees, in any point of the urban area [16]. Studies conducted in US [17,18] showed that the majority of e-scooter trips on shared vehicles is less than 1 mile long. The peak of the rides occurred in the weekend in the middle of the day, suggesting that a lot of trips are related to social and recreational purposes and not only to working commutes. Kopplin et al. [19] highlighted the different motivations in the e-scooter usage between owner and non-owner. Moreover, it is found that shared e-scooter trips tend to substitute walking over short distance rather than the usage of motorised vehicles. Finally, in 2020, all the micro-mobility sector was indirectly boosted by the coronavirus pandemic disease. COVID-19 brought indeed a decreased use of public transport due to restrictions and incentives in favour of e-PMVs in some European countries [6,20–22].

The e-scooter ultimately represents a unique opportunity to improve urban life since it represents a user-accepted solution to several criticalities connected to environment and logistics [23–25]. On the other hand, the number of vehicles together with limited regulations and lack of risk awareness have led to an increasing number of e-scooter related accidents [26,27]. The high potential risk is connected to the interaction with other road users (cars, motorbikes, pedestrians), bad driving habits (road rule braking, alcohol use, etc.) and inadequate infrastructure (lack of specific path, road wear, etc.). Lee et al. [28] conducted a 3-

week study to evaluate the factors which increase the accident probability in the daily life experience. The potential risks are clustered according to the perceived danger level and the relative frequency. Todd et al. [29] monitored by video recording the rider behaviour of rented e-scooters from August to October 2018 in west Los Angeles, a beachside area characterised by high vehicle density and large presence of tourists. A low percentage of riders wore the helmet (almost 10%) and a relevant percentage (almost 7%) drove against the traffic flow. Other bad behaviours consist of the usage of the e-scooter by two people at the same time and the travelling of a street intersection on a red light. E-scooter accidents can be distinguished in two main categories, the single-vehicle event and the collision between two vehicles. The majority of e-scooter accidents belongs to the first group, they are due to rider loss of balance and falling. The loss of balance can be reconducted to poor handlebar controllability, road unevennesses and wrong usage. Injury gravity and potential risk for human health are well-documented by medical publications [30–38]. A multicentre retrospective study which involved two emergency department in Southern California between September 2017 and October 2018 recorded 249 patients related to e-scooter accidents [39]. Among them, 228 people were rider. Almost 10% of the riders is younger than 18 years old and only 5% of them wore the helmet. The most typical injuries were fractures (32%), head injuries (40%) and soft-tissue injuries (28%). A similar study was conducted in Indianapolis [40]. In the monitoring period (61 days), 92 patients (2.73/1000 visits) related to e-scooters required laceration repair (26%) and fracture reduction or fixation (24%): 8% of patients required hospital admission. In both the studies, most riders were male, and the average age was between 30 and 35 years. One of the accident causes is related to poor, non-specific and country-dependent regulations. Since the majority of riders' injuries are the consequence of a falling, the usage of additional safety devices needs to be encouraged or made compulsory such as the elbow and knee pads and the airbag vest to wear over usual clothes. In Europe, BS EN 1728 [41] has been applied since 2020 to define the basic requirements of light motorised vehicles. Safe Micromobility report, presented by the International Transport Forum, aimed at collecting all the available information on injury statistics and risk factor, suggesting improvements for micro-vehicle safety [42]. Even scientific community have started studying this new kind of vehicles to enhance the understanding and provide indications with the purpose of improving comfort and safety. Before presenting the recent research work on e-scooter dynamics, it must be emphasised that electric kick scooters differ a lot from other well-studied two-wheeled vehicles such as bikes and motorbikes. Experimental and numerical

analyses conducted on other two-wheeled systems are therefore not sufficient to achieve a full understanding of e-scooter dynamics. An important difference with respect to motorbikes is the inertia ratio which is shifted towards the rider. Considering average vehicle and rider masses respectively of 15 kg and 80 kg, the inertia ratio is almost equal to five. An aspect which distinguishes e-scooter both from bike and motorbikes is the rider standing position: the sitting surface is missing and the interfaces between the rider and the vehicle are provided only by the handlebar and the deck floor. The last point to be mentioned stands in tyre dimension: small radius and width influence both stability and control. In the following, a literature summary of the recent research works from a mechanical point of view is proposed.

- Garman et al. [43] experimentally analysed the e-scooter/rider performances under controlled and repeatable conditions. Urban environment (obstacle to avoid) and typical manoeuvre (starting, braking, unexpected events) are studied through the design of a specific test course. Several riders are tested and measurements on the vehicle and the human body are taken.
- Brunner et al. [44] collected data in a controlled testing facility to evaluate the vehicle stability and the rider driving gestures. The research activity highlighted that even beginner riders are able to perform complex manoeuvre and progressively increase their driving skills in a very short amount of time.
- Paudel [45,46] studied in his PhD research activity the stability of small wheel single-track vehicle, including the e-scooters, putting in evidence the effect of the tyre size. The handling analysis took into account self-stability property, steady-state turning performance and the effect of the load transfer due to acceleration.
- Ma et al. [47] evaluated the safety risks riding e-scooters in different environments. Several road surfaces such as sidewalks, concrete roads and lumped unevennesses are tested monitoring vibrations. A cumulated frequency grid of close object is created exploiting a LiDAR sensor in the experimental setup. The same authors developed a multibody model [48] to quantitively analyse the ride comfort for different types of wheels and suspensions.
- Cano-Moreno et al. [49] experimentally investigated the comfort quality of a commercial e-scooter on two different road surfaces, adopting different velocities and tyre pressures. Moreover, the

influence of the rider's mass is analysed. A very poor comfort level is generally detected, further deteriorated at high velocity and driving on cobblestones.

- Boglietti et al. [50] conducted an experimental comparison between e-scooters and bikes in terms of ride comfort driving on different road surfaces. ISO 2631 frequency filtering procedure and statistical Z-tests remarked significant differences between the vehicles and a strong dependency of e-scooter vibrations on the path, the rider and the velocity.
- Asperti et al. [51,52] analysed through a lumped parameter model the rider comfort and the road holding capability driving on lumped obstacles and random road input. The tyre envelope profiles are calculated by a dedicated test bench varying the vertical load and the tyre pressure. Rider's impedance is also taken into account considering the human body as a 3 DOF system.
- Arslan et al. [53] developed a multibody model in Matlab/Simulink to study the force exchanged between the vehicle and the rider driving over curbs; the influence of the tyre size, the velocity and the rider's mass was also taken into account. The rider is modelled as a unique body which stands for the torso while upper and lower limbs are considered as translational spring-damper systems. Tyre-road model is represented by a contact force.
- Gulino et al. [54] studied different materials for the deck component in order to improve ride comfort and reduce the vehicle inertia. The experimental tests underlined that adopting a bamboo deck leads to a mass reduction of almost 65% and better vibration performances with respect to an aluminium deck equipped with suspensions.
- Leoni et al. [13] experimentally analysed and compared the comfort quality and the stability performance of seven different e-scooters in Milan city.

The main theme of this PhD dissertation is the investigation on the longitudinal and the vertical dynamics of electric kick scooters from an experimental and numerical point of view giving a special focus on human-vehicle interaction. For this purpose, two commercial vehicles are taken into account. The e-scooters are selected first in order to assess the effect of different design solutions (vehicle dimensions, tyre characteristics, suspension, motor and braking system) on the system dynamics. The investigation is limited to two

models as compromise between variety of vehicle characteristics, purchasing costs and experimental testing efforts. In the following, the main novelties of the research work with respect of the state of the art and the organisation of the thesis are provided.

Original contributions

Novelties of the presented research activity and advances with respect to the state of the art are here highlighted.

- A deep investigation focusing on components and assemblies is carried out with the purpose of identifying the main features of e-scooter category. Experimental techniques and CAD tools are exploited to estimate the inertial properties. Tyre vertical stiffness is evaluated in laboratory varying load conditions and considering different tyre models. An experimental and numerical analysis dealing with longitudinal manoeuvres allows to evaluate the electric motor characteristics in driving and regeneration; moreover, braking performance and resistance force are assessed.
- An experimental comparison focused on vertical dynamics is carried out between two e-scooters. The study is conducted on lumped univenesses and homogeneous surfaces; it follows procedures based on International Standards and aims at evaluating the effect of velocity and different design solutions on ride comfort.
- Rider motion is evaluated from an experimental point of view in typical driving conditions such as standstill start, braking and overcoming small road obstacles. In this context, a statistical analysis involving a heterogeneous population and focusing on the vertical dynamics allows to objectively assess the effect of anthropometric features and velocity on vibrations and vehicle-to-rider transmissibility.
- A detailed multibody model is developed as support of the experimental analyses. An advanced tyre model (MF-Tyre/MF-Swift) which takes into account high frequency phenomena and short wavelength road obstacles is integrated. The model also includes a parametric dummy able to reproduce the real kinematics of the human body.

Organisation of the thesis

The dissertation is organised in seven chapters and three appendices.

- *Chapter 1.* In the following of the current chapter, a global overview on the category of electric kick scooters is given, underlining the main components and the different design solutions.
- *Chapter 2.* The attention is focused on two specific models which are experimentally and numerically assessed. Their technical specifications are first shown. Then, some preliminary analyses aiming at identifying unknown characteristics such as inertias and tyre vertical stiffness are presented.
- *Chapter 3.* The experimental tests for the longitudinal dynamics characterisation are presented; furthermore, the development of a lumped parameter model is discussed to highlight the dynamic influence of rider motion on the global system in standing start and braking manoeuvres.
- *Chapter 4.* An experimental ride comfort assessment with the purpose of comparing the e-scooters on lumped unevennesses and homogeneous surfaces is presented.
- *Chapter 5.* Rider's motion is analysed. A statistical analysis conducted on a sample of fourteen people to study the vehicle-to-rider vibration transmissibility is proposed.
- *Chapter 6.* A multibody model including the vehicle and the rider systems is described and exploited to simulate the braking manoeuvres and the dynamic response driving over road bumps.
- *Chapter 7.* The main conclusions and insights on future developments of the activity are presented.
- *Appendixes A.* Details on the sensors used in the experimental campaigns are given.
- *Appendixes B.* The algorithm used for the vehicle velocity estimation in the longitudinal tests is described.
- *Appendix C.* The advances on Pacejka's tyre model known as MF-Tyre/MF-Swift, which is included in the vehicle multibody model, are reported.

Overview on electric kick scooters

According to vehicle classification, electric kick scooters are part of the macro-category of light two-wheeled vehicles (L1e). In particular, they are included in the L1e-b category, i.e., the light mopeds. The nominal power must be lower than 350 W and the driving torque must be interrupted at 25 km/h. The e-scooters are formally different from the pedal assisted bikes, whose category is named L1e-a: the main differences are the maximum nominal power of the motor, equal to 250 W, and the motor assistance only in case of rider pedalling. On the other hand, e-scooters are considered as traditional bikes according to the road traffic code. Front and rear lights, as well an acoustic signal, are mandatory. Moreover, they can be driven only on cycle paths or, if not present, at the far right of urban roads. It is strictly forbidden the usage on the roads with speed limit higher than 50 km/h. In pedestrian areas, the speed limit is decreased to 6 km/h. For this reason, most e-scooter models include an electric motor setting, in order to automatically limit their maximum velocity. Electric scooters can be used by people that are at least 14 years old and do not require any driving licence. The users under 18 years must wear a bike helmet. Figure 1 represents a generic electric standing scooter with the most common components.

Figure 1 - E-scooter components

The main structural components of e-scooters are the deck and the steering column. The deck is the board extended in length on which the rider places his feet. The rear tail of the deck houses the supporting elements of the rear wheel.

The steering column is hinged on the front part of the deck; the supporting element of the front wheel is housed at the bottom and the handlebar at the top of the steering column. On some models, the steering column can be divided into two parts, connected with a hinge, to allow folding the vehicle. This hinge is generally next to the steering joint and must be locked in the normal vehicle usage. The steering column is always inclined with respect to the vertical axis such that the top end is toward the vehicle back (as in all the two-wheeled vehicles). The handlebar is the bar transversal to the vehicle plane on which the rider holds his hands. Different tasks are carried out by this component:

- providing the steering command from the rider hands to the front wheel through the steering column;
- ensuring the hand hold, essential for the rider balance;
- ensuring the vehicle control thanks to the accelerator, the braking lever, the display, etc.

The accelerator (left panel in Figure 2) is typically placed on the right while the braking lever (right panel in Figure 2) on the left. The display provides information relative to the vehicle velocity, the battery state of charge and other settings.

Figure 2 - Accelerator (left) and braking lever (right)

In more complex architectures, very simple suspension systems can be included. At the front, a couple of shock absorbers are installed between the end of the steering column and the wheel (left panel in Figure 3). At the rear, a suspension with a trailing link is commonly used (right panel in Figure 3).

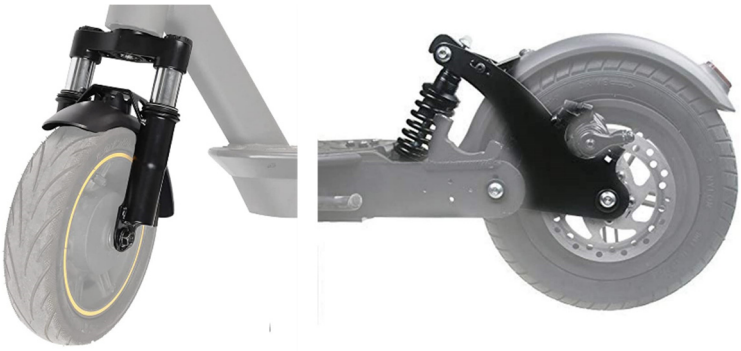

Figure 3 - Front (left) and rear (right) suspension systems

As regards the propulsion system, the electric motor is mounted at the front or at the rear instead of the traditional wheel. An example of electric motor integrated in an e-scooter wheel is reported in Figure 4.

Figure 4 - Electric motor integrated in the wheel assembly

In advanced e-scooters, the electric motor generally works not only in driving but also in coasting and braking. The kinetic energy is recovered and stored to increase the travel range if the battery is not fully charged[1]. The battery pack (left panel in Figure 5) and the vehicle control unit (right panel in Figure 5) are placed inside the deck. In some cases, the battery can be also externally docked, on the deck or the steering column, to simplify the replacement. This solution is generally adopted in the e-scooter fleet belonging to the sharing services. The exchange of the discharge battery with a fully charged battery is preferred to the traditional recharge because of time and logistic constraints.

[1] Kinetic Energy Recovery System (KERS)

Figure 5 - Battery pack (left) and control unit (right)

If the electric motor is on the front wheel, a mechanical braking system is mounted on the rear wheel; vice versa the braking system is on the front wheel, if the motor is on the rear wheel. The mechanical braking system is seldom on both the wheels: two different braking levers are mounted on the handlebar, like on bikes. Two braking systems are commonly adopted, i.e., disc (left panel in Figure 6) or drum brake (right panel in Figure 6). Both systems are directly actuated by the braking lever by means of a wire.

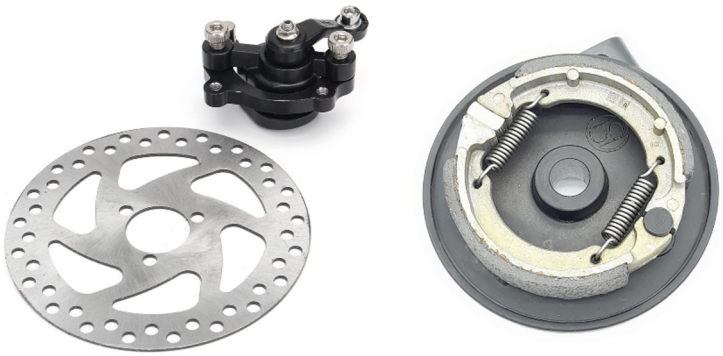

Figure 6 - Disc and drum brake

It is worth to mention that a braking sensor is mounted inside the braking lever, so that the driving torque is instantaneously cut when the braking lever is pulled. When the motor works as braking, its torque follows the command of the braking lever. E-scooter tyres belong to two main categories: pneumatic and solid rubber tyres. Among the first group, the tyre can be equipped an inner tube or be tubeless. More details are provided in paragraph 2.3. Other common accessories of electric scooters are lights and mudguards, respectively mounted at the bottom

of the steering column and on the rear part of the deck. In light of the several design solutions available on commercial electric kick scooters, a market survey is conducted with the purpose of selecting some electric kick scooters to be investigated from an experimental and numerical point of view. Table 1 reports some examples of potential vehicles with their characteristics. It is preliminarily decided to limit the analyses on two models due to the purchasing costs and the amount of time necessary to adapt the sensor setup, conduct the tests and process the data. The selection criterion consists of identifying two vehicles characterised by many differences in terms of design solutions in order to assess their impact on the system dynamics. Since the main focus of the research activity is on ride comfort, priority is given to tyres and suspensions: it is expected that these components have a direct impact on vehicle vertical dynamics and ride comfort perceived by the rider. Secondary aspects to be considered in the selection are related to the motor (nominal and peak power, position), the mechanical braking system (type and position), the main dimensions (wheelbase, handlebar height) and the mass. In light of the abovementioned considerations and balancing the purchasing costs, it is decided to take into account Aprilia ESR2 and Xiaomi Pro II. Contrary to Xiaomi Pro II, Aprilia ESR2 is equipped with front and rear suspensions. Moreover, the tyres of Aprilia ESR2 are larger and inflated with a lower pressure with respect to the ones of Xiaomi Pro II. Motor and mechanical braking system are positioned in an opposite way. As a general comment, Aprilia ESR2 is larger, heavier and more solid than Xiaomi Pro II. More details on the two vehicles are given in paragraph 2.1.

Table 1 - Examples of commercial electric scooters and their characteristics

Vehicle	Motor		Mechanical braking		Tyre		Suspension	
	Power [W]	Position	Type	Position	Diameter [in]	Type	Front	Rear
Aprilia ESR1	350	Front	Disc	Rear	10	Tubeless	×	×
Aprilia ESR2	350	Rear	Drum	Front	10	Tubeless	✓	✓
Argento EVO	350	Rear	Drum	Front	10	Tubeless	×	×
Argento Sport	500	Front	Disc	Rear	10	Tubeless	✓	✓
Ducati City Cross-E	350	Front	Disc	Rear	10	Tubeless	×	×
Ducati Sport Cross-E	500	Rear	Disc	Front/Rear	10	Tubeless	×	×
Jeep Sentinel	350	Front	Disc	Rear	10	Tubeless	✓	×
Jeep Adventurer	350	Front	Disc	Rear	10	Tubeless	✓	✓
Jeep Camou	500	Front	Disc	Rear	10	Tubeless	✓	✓
Lamborghini ALext	500	Rear	Disc	Front/Rear	11	Tubeless	✓	✓
Lancia Ypsilon	250	Rear	Electric	Front/Rear	8.0	Solid	×	×
Nilox X-Drive M1	350	Front	Disc	Rear	8.5	Inner tube	×	×
Xiaomi Pro II	300	Front	Disc	Rear	8.5	Inner tube	×	×

Chapter 2

Preliminary analyses

In this chapter some preliminary analyses aimed at characterizing the electric scooters involved in the experimental campaign and numerical modelling are discussed. As already discussed in Chapter 1, the investigation is focused on two different vehicles, i.e., Xiaomi Pro II and Aprilia ESR2. These two electric scooters are selected in order to analyse vehicles characterised by different topological solutions which may impact on longitudinal and vertical dynamics. Among the main features, a particular emphasis is given to the presence of suspension systems and the tyre size which can have an influence on vibrations and ride comfort. Secondly, differences related to electric motor, mechanical braking system, dimensions and inertias are considered.

Paragraph 2.1 reports data from the technical specifications; paragraph 2.2 deals with the identification of the inertial properties adapting methodologies described in literature; paragraph 2.3 is focused on the evaluation of tyre radial stiffness through compression tests; paragraph 2.4 reports the main data of the rider who conducted the majority of the experimental tests.

2.1 Starting data

Figure 7 shows the main dimensions of the two e-scooters under analysis. Xiaomi Pro II is in the left panel while Aprilia ESR2 is in the right panel. Overall dimensions, in black, are reported from the technical specifications; the inclination of the steering column and the wheelbase are measured in laboratory.

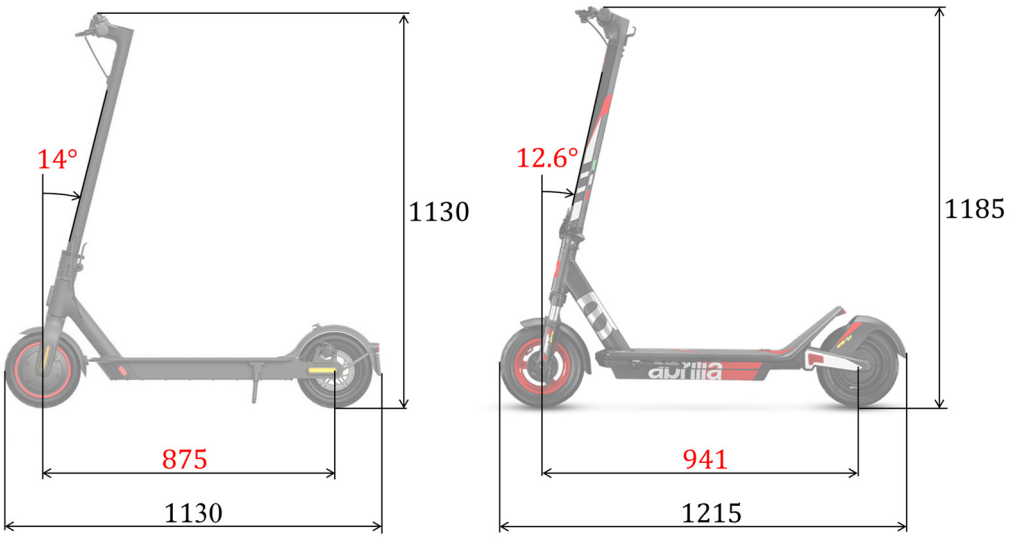

Figure 7 - Dimensions of Xiaomi Pro II (left) and Aprilia ESR2 (right)

As evidenced by Figure 7, Aprilia ESR2 is slightly larger than Xiaomi Pro II. The mass of the two e-scooters from the relative technical specifications are reported in Table 2.

Table 2 - Mass from technical specifications

	E-scooter	
	Xiaomi Pro II	**Aprilia ESR2**
Nominal mass [kg]	14.2	16.5

Aprilia e-scooter is almost 2 kg heavier than Xiaomi e-scooter. As regards the propulsion system, both the e-scooters are equipped with a DC brushless motor, Xiaomi Pro II at the front wheel, Aprilia ESR2 at the rear wheel.

Table 3 - Motor data

	E-scooter	
	Xiaomi Pro II	**Aprilia ESR2**
Nominal power [W]	300	350
Peak power [W]	600	600

A slight difference can be remarked in the nominal power. Peak power is the same for both the vehicle. The battery pack is placed inside the deck of both the e-scooter. The battery characteristics are reported in Table 4.

Table 4 - Battery data

	E-scooter	
	Xiaomi Pro II	**Aprilia ESR2**
Nominal voltage [V]	36	36
Capacity [Ah]	12.4	8.0
Mass [kg]	3	1.8

The nominal voltage of the battery is the same in both the vehicle while the capacity is smaller in Aprilia ESR2 with impact on its mass and travel range.

Both e-scooters mount pneumatic tyres with inner tube. The tyres have different size and nominal pressure, as reported in Table 5.

Table 5 - Tyre sizes and nominal air pressure

Tyre characteristic	E-scooter	
	Aprilia ESR2	**Xiaomi Pro II**
Diameter [in]	10	8.5
Width [mm]	55	50
Pressure [bar]	2.5	3.5

Differently from Xiaomi Pro II, Aprilia Pro II presents the suspension system both at the front and at the rear.

Figure 8 - Aprilia ESR2 front (left) and rear (right) suspension systems

Other relevant information from the technical specifications on the vehicles is reported in Table 6.

Table 6 - Other data

	Xiaomi Pro II	**Aprilia ESR2**
Travel range [km]	45	25
Maximum slope [%]	20	23

The maximum payload is equal to 100 kg for both vehicles; Xiaomi recommends the usage by riders whose height is between 1.2 and 2 m.

2.2 Characterisation of the inertias

The identification of the inertial properties is divided as follow. Firstly, the mass of the two e-scooters and the mass of some components are measured. Secondly, the centre of mass is evaluated applying two methodologies from literature. Finally, CAD tools are exploited to estimate the inertial properties of the single components as well the moments of inertia of the whole assemblies.

2.2.1 Mass

The analysis of the masses deals with the single parts and the whole vehicles. To do so, a precision balance with accuracy equal to 0.001 kg is used. Some of the main components belonging to Xiaomi Pro II are disassembled and weighted first: they are reported in Table 7.

Table 7 - Measured masses of some components of Xiaomi Pro II

Component	Mass [kg]
Tyre	0.479
Rear wheel	0.657
Braking disc	0.110
Electric motor	3.131

Then, the mass of the two vehicles is measured: they are reported in Table 8.

Table 8 - Measured masses of the two e-scooters

	Xiaomi Pro II	**Aprilia ESR2**
m_s [kg]	14.450	16.423

The measured mass of the two e-scooters is in agreement with the technical specifications.

2.2.2 Centre of mass

The second step of the inertial characterisation consists of the identification of the location of the centre of mass of the two e-scooters. Figure 9 represents the convention adopted in the procedure for the centre of mass identification. The reference system is placed in the front wheel centre in correspondence of the middle plane of the vehicle; x axis corresponds to the longitudinal direction and looks backwards; z axis corresponds to the vertical direction and looks upwards; y axis corresponds to the lateral direction and looks leftwards. w is the vehicle wheelbase, l_s is the longitudinal component of the distance between the front wheel centre and the e-scooter centre of mass, h_s is the vertical component of the distance between the front wheel centre and the e-scooter centre of mass.

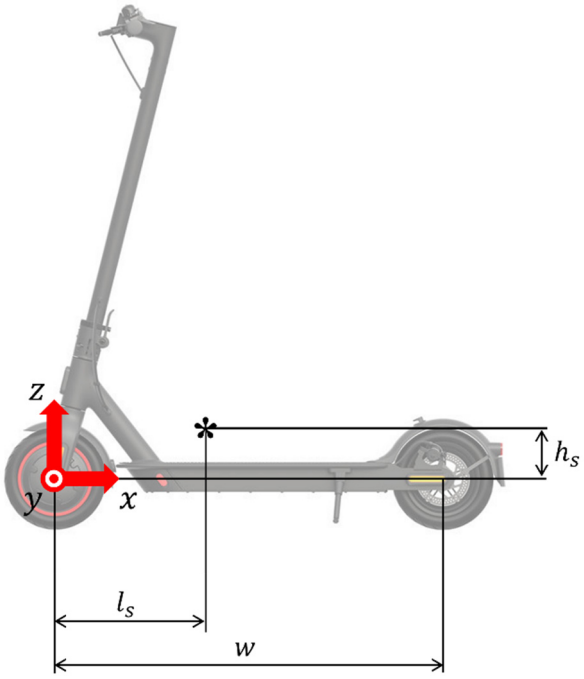

Figure 9 - Reference frame and symbols adopted for the centre of mass identification

Due to the symmetry of the vehicle, the centre of mass is supposed to be in xz plane, so the centre of mass identification is reduced to find l_s and h_s. The suspension method described in [55] is exploited first. This method prescribes that the test specimen must be suspended at different points. The location of the centre of mass is given by the intersection of the projections of the suspension wire. At least two different suspension points are required to correctly identify the centre of mass. This method is commonly used and approved even though its accuracy is low due to the difficulties of identifying the coordinates only from geometrical information. In order to overcome this critical issue, the deck upper surface is used as reference. It is preliminary checked that this surface is completely flat and parallel to the ground for both the e-scooters. A digital inclinometer with accuracy equal to $0.5°$ is used to measure the angle between the reference surface and the ground surface in each suspension configuration. The projection of the suspension wire is recreated after the test starting from known data (suspension point, vehicle geometry, deck surface inclination). Figure 10 refers to the suspension test performed on Xiaomi Pro II. Two different suspension points are adopted:

- the middle point of the handlebar;
- the rear wheel hub.

Red and blue solid line represent the suspension wire projections while dash-dot lines are just construction axes.

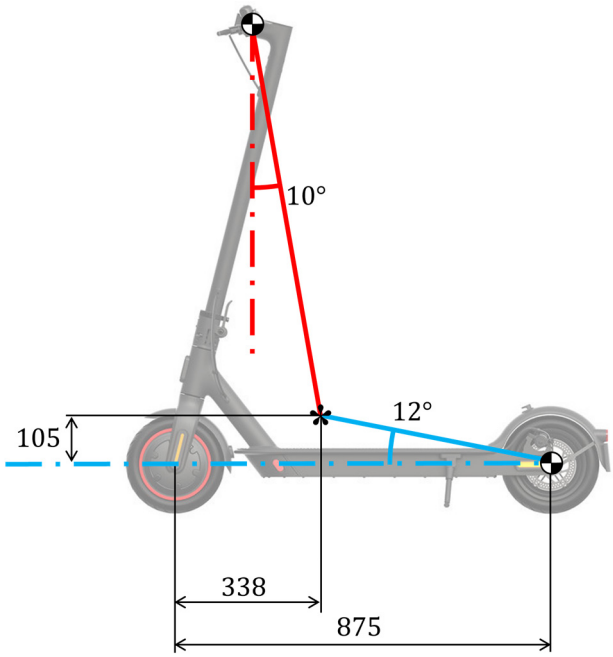

Figure 10 - Xiaomi Pro II centre of mass identification (suspension method)

The same procedure is repeated for Aprilia ESR2, as shown in Figure 11. In this case, three suspension points are used:

- the middle point of the handlebar;
- the front wheel hub;
- the rear wheel hub.

The suspension wire projections are respectively represented by red, green and blue solid line.

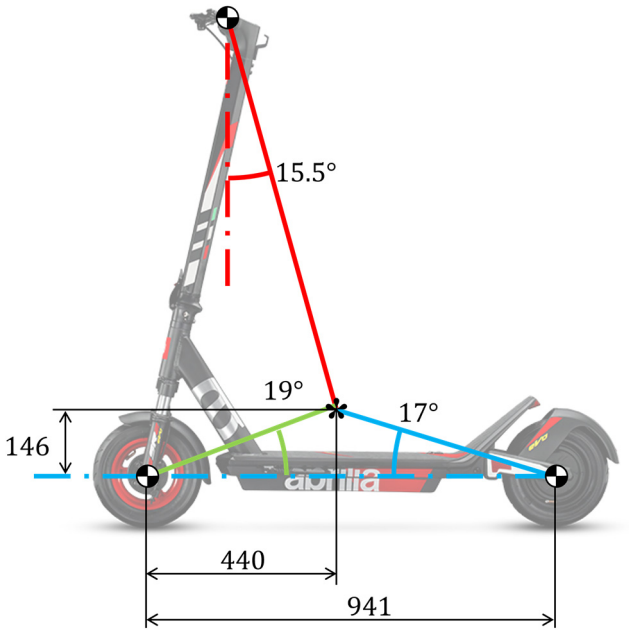

Figure 11 - Aprilia ESR2 centre of mass identification (suspension method)

Suspending the system at one more point increases the accuracy of the identification. The distance between the front wheel centre and the centre of mass split along x and z axis is reported in Table 9.

Table 9 - Centre of mass coordinates (suspension method)

Distance	**E-scooter**	
	Xiaomi Pro II	**Aprilia ESR2**
l_s [m]	0.338	0.440
h_s [m]	0.105	0.150

l_s is similar between the vehicles. Larger difference occurs in terms of h_s. l_s of Xiaomi Pro II is also verified exploiting interface force measurement method [55]. Knowing the mass of the test specimen and the location of the external forces, the coordinates of the centre of mass is determined. In this test, the external forces are nothing but the tyre vertical reactions $F_{z,f/r}$: they are evaluated

in static condition by a balance with accuracy equal to 1 N. The forces are reported in Table 10.

Table 10 - Vertical force on the tyres of Xiaomi Pro II

$F_{z,f}$ [N]	92
$F_{z,r}$ [N]	56

Using Eq. (1), l_s is computed.

$$l_s = \frac{F_{z,r}}{F_{z,f} + F_{z,r}} w \tag{1}$$

The comparison between the results obtained by the suspension method and the interface force measurement method is reported in Table 11.

Table 11 - Centre of mass x coordinate (suspension and interface force measurement method)

Method	l_s [m]
Suspension	0.338
Interface force	0.331

The difference is less than 0.01 m. Since the small gap between the two estimations, the interface force measurement method is not repeated on Aprilia ESR2. Interface force measurement method is also used to determine the longitudinal coordinate of the centre of mass of the system composed by Xiaomi Pro II and the rider. The mass of the rider, m_r, is equal to 80.0 kg while the height, H_ρ, is equal to 1.80 m. The rider positioning is monitored by the location of his foot tips. Two different configurations, P_{x1} and P_{x2}, are tested. The rider configurations are sketched in Figure 12.

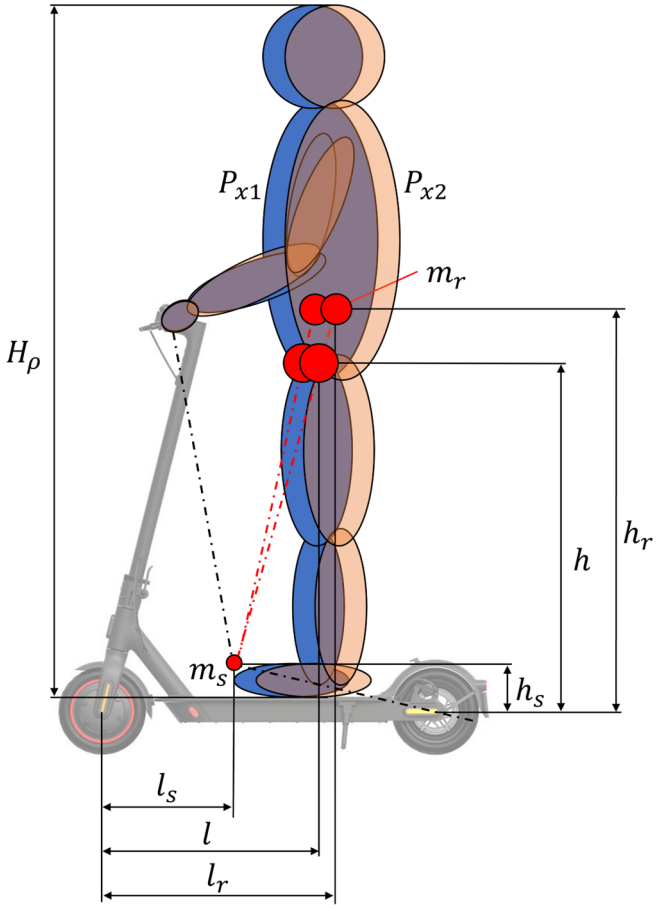

Figure 12 - Rider configurations

The two rider configurations in terms of distance between the front wheel centre and foot tips are also reported in Table 12.

Table 12 - Rider configurations on Xiaomi Pro II

Configuration	**Front wheel centre to foot tip distance [m]**
P_{x1}	0.345
P_{x2}	0.400

The measured vertical forces acting on the front and the rear tyres are reported in Table 13.

Table 13 - Vertical tyre forces of Xiaomi Pro II with rider on in two configurations

Force	**Rider position**	
	P_{x1}	P_{x2}
$F_{z,f}$ [N]	391	344
$F_{z,r}$ [N]	503	540

Following Eq. (1) the centre of mass coordinate of the whole system along x axis is determined. As regards the coordinate along z axis, a first raw evaluation is computed. The height from the ground of the centre of mass of the human body generally corresponds to the navel; it is commonly assumed at the 60% of his whole height. h_r, i.e., the distance along z axis between the human body centre of mass and the tyre wheel centre, is computed according to Eq. (2).

$$h_r = 0.6\, H_\rho + h_d - r_t \tag{2}$$

h_d is the height of the deck floor from the ground and is equal to 0.145 m; r_t is the tyre radius and is equal to 0.108 m. h is just computed as the weighted sum according to Eq. (3).

$$h = \frac{h_r m_r + h_s m_s}{m_r + m_s} \tag{3}$$

Results in terms of centre of mass location of the whole system are reported in Table 14.

Table 14 - Front wheel centre to centre of mass of the whole system distance (Xiaomi Pro II)

Configuration	l [m]	h [m
P_{x1}	0.493	0.963
P_{x2}	0.535	

For sake of completeness, the rider center of mass location with respect to the front wheel center along x and z axes are reported in Table 15.

Table 15 - Front wheel centre to centre of mass of the rider distance (Xiaomi Pro II)

Configuration	l_r [m]	h_r [m
P_{x1}	0.521	1.117
P_{x2}	0.571	

l_r is computed according to Eq.,

$$l_r = \frac{(m_r + m_s)l - m_s l_s}{m_r} \tag{4}$$

Results in terms of longitudinal location of the human body center of mass (l_r) for the different foot configurations are coherent: a shift towards the rear of the deck of the foot tip equal to 0.055 m implies a backwards shift of the center of mass of the rider equal to 0.05 m. As evidenced by Table 14 and Table 15, the inertial contribution of the rider is relevant with respect to the one of the e-scooter due to his mass which is approximately six times the mass of the vehicle.

2.2.3 Moments of inertia

The last phase in the inertia identification is the estimation of the moments of inertia of the main e-scooter components. This critical step is particularly important in the perspective of developing a model composed by rigid bodies for dynamic simulations. To do so, the experimental information which are discusses in paragraph 2.2.1 and 2.2.2, are exploited together with CAD tools. SolidWorks 2015 is used as CAD software. The first step consists of building CAD models of the two e-scooters. Xiaomi Pro II CAD model consists of eight parts, as shown in Figure 13.

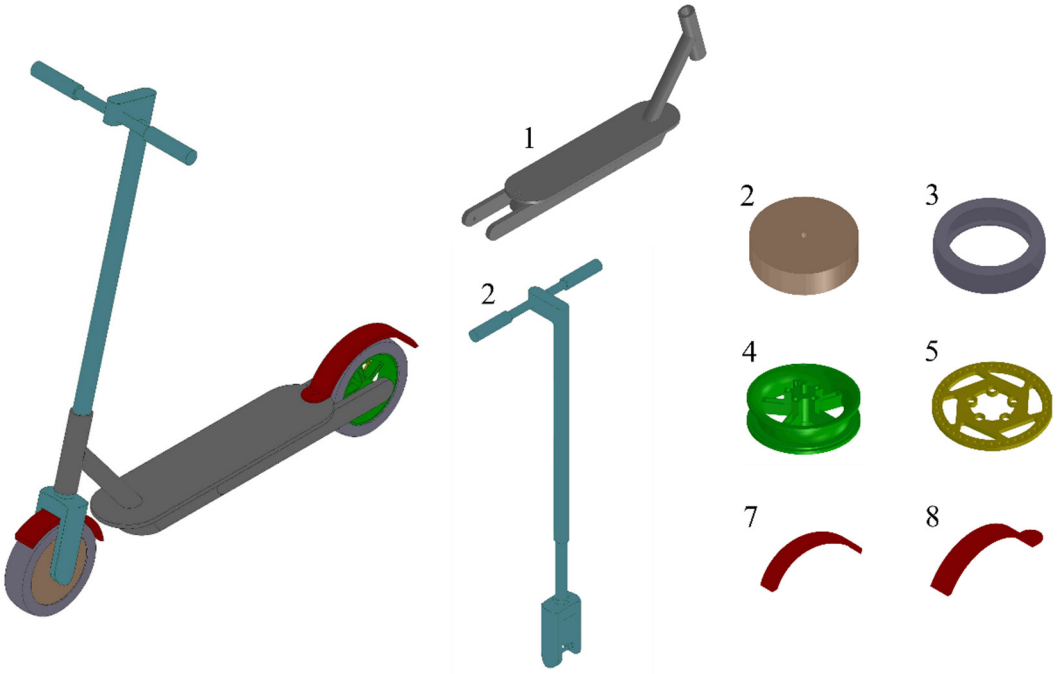

Figure 13 - Xiaomi Pro II CAD model

Apart from the steering column and the deck which are hollow, all the parts are modelled as solid geometries characterised by homogeneous densities. The presence of the battery pack inside the deck is neglected. Equivalent density values are assigned to the components whose weight is experimentally measured, i.e., the electric motor, the tyre, the rear wheel and the braking disc. Front and rear mudguard are supposed to be made of plastic. Deck and steering column equivalent densities and thicknesses are varied to match the experimental mass and centre of mass location of the whole e-scooter. The mass of the Xiaomi Pro II parts is reported in Table 16.

Table 16 - Mass of Xiaomi Pro II CAD parts

Part	**Marker**	**Mass [kg]**
Deck	1	6.969
Steering column	2	2.482
Electric motor	3	3.084
Tyre	4	0.482
Rear wheel	5	0.550
Braking disc	6	0.225
Front mudguard	7	0.051
Rear mudguard	8	0.177

The location of the centre of mass and the orientation of the principal axes of inertia of Xiaomi Pro II CAD assembly is represented in Figure 14.

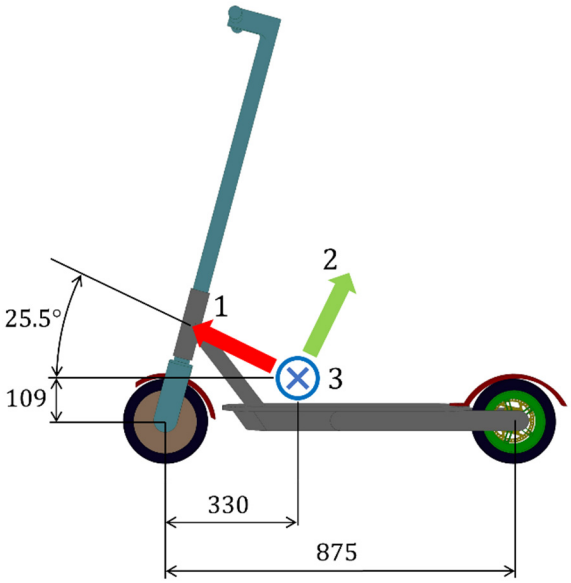

Figure 14 - Centre of mass and principal axes of inertia of Xiaomi Pro II CAD assembly

As evidenced by Figure 14, the gap in terms of centre of mass location between the CAD model and the experimental results (Table 9) is less than 0.01 m. The mass and the principal moments of inertia of Xiaomi Pro II CAD assembly are reported in Table 17.

Table 17 - Inertias of Xiaomi Pro II CAD assembly

m [kg]	14.503
J_1 [kgm^2]	0.931
J_2 [kgm^2]	1.477
J_3 [kgm^2]	2.372

The difference between the mass of the CAD assembly (Table 17) and the measured mass (Table 8) is equal to 0.05 kg. Moments of inertia of the whole assembly obtained by the CAD model (Table 17) are in line with the ones reported by Cano-Moreno et al. [48].

The procedure described for Xiaomi Pro II is also applied to Aprilia ESR2. Differently from the previous e-scooter, the geometry is more complex due to the presence of suspension systems. The CAD modelling requires ten parts as shown in Figure 15.

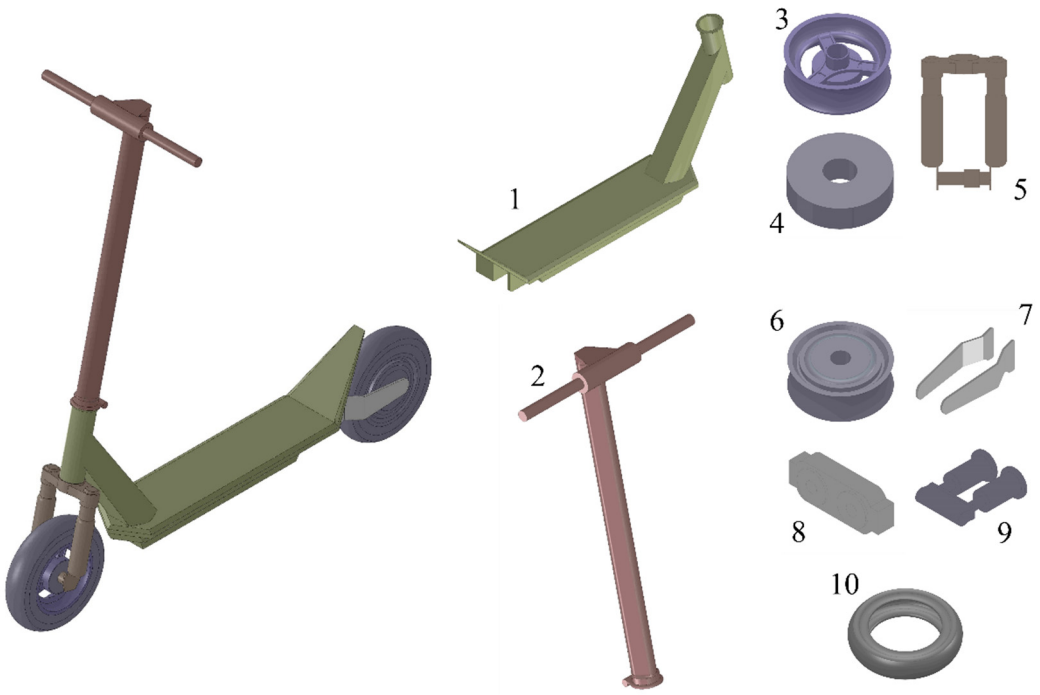

Figure 15 - Aprilia ESR2 CAD model

The experimental data which are available for Aprilia ESR2 are the mass (Table 8) and the centre of mass coordinates of the entire assembly (Table 9). In the attempt of reducing the number of unknowns, densities belonging to the wheel, the electric motor and the tyre are supposed to be equal to the densities identified for the same components of the other e-scooter. Drum brake and suspension systems are supposed to be made of aluminium and steel. Finally deck and steering column are tuned in order to achieve the experimental mass and the location of the centre of mass of the entire assembly. Table 18 collects the masses of the parts belonging to the Aprilia ESR2.

Table 18 - Mass of Aprilia ESR2 CAD parts

Part	Marker	Mass [kg]
Deck	1	7.285
Steering column	2	2.118
Front wheel	3	0.634
Drum brake	4	0.554
Front suspension	5	0.697
Electric motor	6	3.030
Rear fork	7	0.148
Rear suspension plate	8	0.293
Rear springs	9	0.496
Tyre	10	0.568

Figure 16 represents the location of the centre of mass and the orientation of the principal axes of inertia.

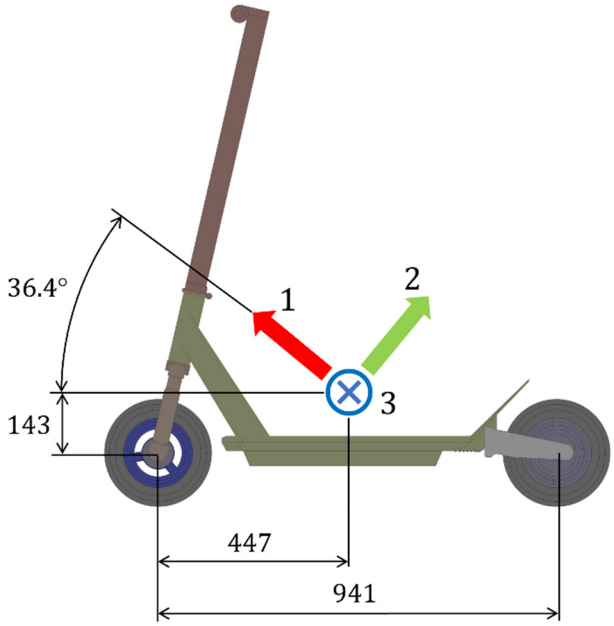

Figure 16 - Centre of mass and principal axes of inertia of Aprilia ESR2 CAD assembly

The mass and the principal moments of inertia of Aprilia ESR2 CAD assembly are reported in Table 19.

Table 19 - Inertias of Aprilia ESR2 II CAD assembly

m [kg]	16.390
J_1 [kgm^2]	1.144
J_2 [kgm^2]	2.364
J_3 [kgm^2]	3.468

2.3 Tyre stiffness

Tyre radial stiffness represents an important parameter for vehicles from the perspective of ride comfort. This aspect is even more significant for the e-scooters lacking in suspension systems, where the road filtering effect is obtained only by the tyre. Three different tyres are analysed:

- Xiaomi Pro II pneumatic tyre (original part);
- Xiaomi Pro II solid rubber tyre (replacement part);
- Aprilia ESR2 pneumatic tyre (original part).

The three tyres are shown in Figure 17.

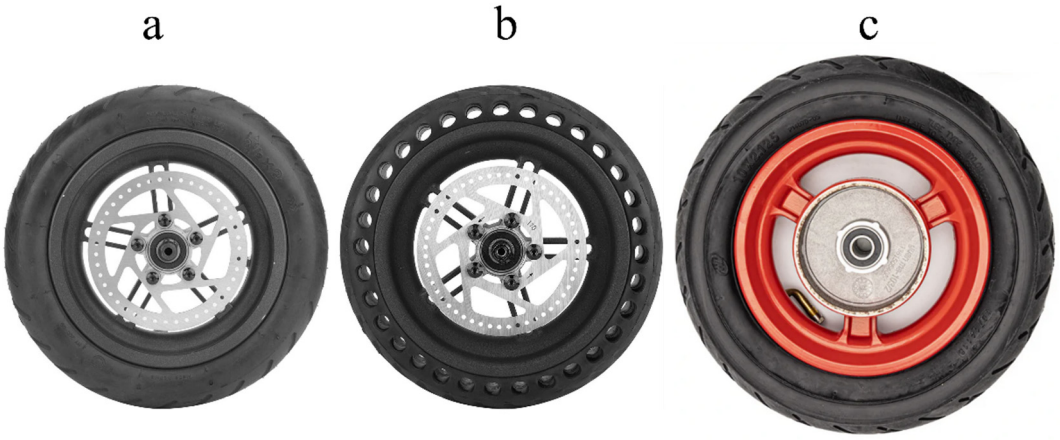

Figure 17 - Xiaomi Pro II rear wheel with the pneumatic tyre (a) and with the solid rubber tyre (b), Aprilia ESR2 front wheel with the pneumatic tyre (c).

The common characteristic of the pneumatic tyre is the presence of the inner tube between the wheel rim and the tyre carcass. On the other hand, the differences stand in the tyre size and the nominal air pressure (Table 5). During the tests, the tyres are mounted respectively on Xiaomi Pro II rear wheel without braking disc and Aprilia ESR2 front wheel without drum brake. The clamping system is realised exploiting the wheel hub, a U-shaped bracket with wing distance equal to 100 mm, M6/M8 bolts, nuts and washers. The tests are conducted on MTS QTest/10 Elite machine.

Figure 18 - MTS QTest/10 Elite testing machine with Aprilia tyre

The tyre is vertically loaded moving the crossbar of the testing machine: the crossbar is driven in displacement control. A load cell with full-scale equal to 10 kN is mounted between the cross bar and the tyre. Assuming that the displacement of the crossbar is equal to the tyre deflection, the tyre stiffness can be computed deriving the force-displacement curve. Moreover, a digital dial indicator with accuracy equal to 0.001 mm is used to evaluate the deflection of the wheel support elements. The dial indicator is mounted with an inclination of 48° with respect to the vertical axis.

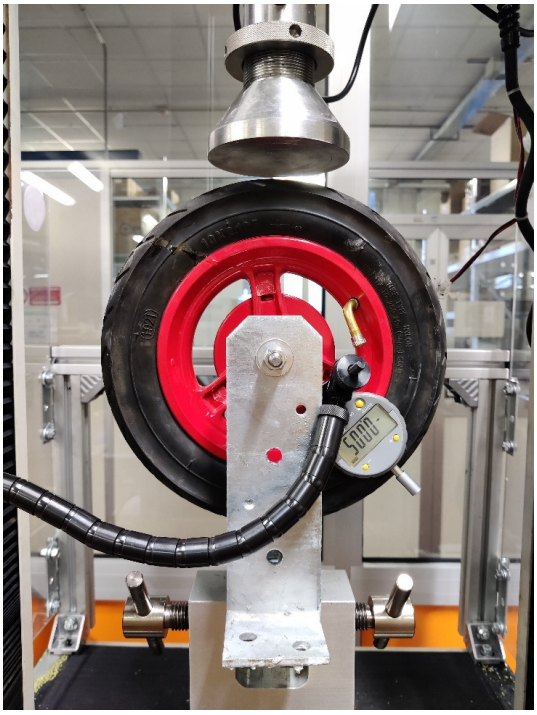

Figure 19 - Clamping system and dial indicator on the wheel hub

The testing procedure and the data processing are presented for the Aprilia tyre. The same procedure is applied to the pneumatic and solid rubber tyre of the Xiaomi e-scooter. Three tests for each tyre are performed. TestWorks 4 Software is used to control the machine and acquire the signals. The crossbar is moved downwards in order to compress the tyre, increasing the vertical force from 0 to 1 kN. Time, crossbar displacement Δ and force F are exported and analysed in Matlab R2022b. In order to reset the static offsets, displacement and force are set to 0 in correspondence of a measured force of 0.6 N.

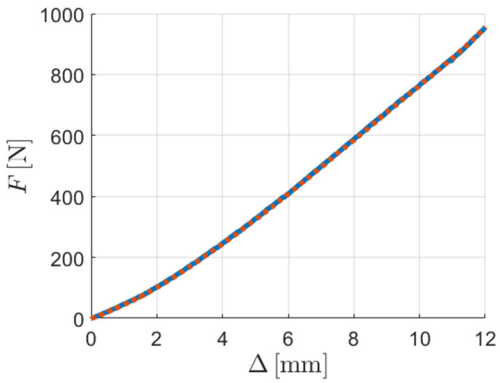

Figure 20 - Force against crossbar displacement, offset corrected signals.

As evidenced by Figure 20, the results are sufficiently repeatable in the entire force range. Thus, a single test is selected for the identification of the tyre stiffness. First, the experimental signals are fitted with a least squares regression between 0 and 900 N. The most suitable degree of the polynomial is identified forcing the regression through the origin. Figure 21 plots the comparison between the experimental force-displacement characteristic and the resulting polynomials.

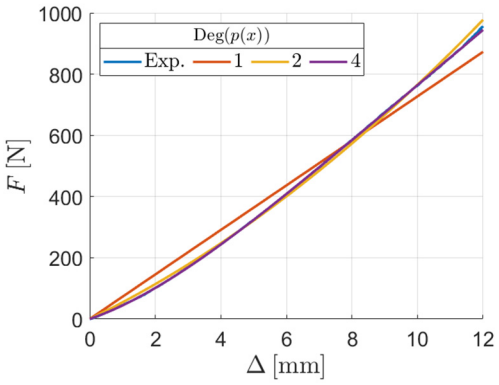

Figure 21 - Polynomial fitting of the force-displacement data

Table 20 presents the least squares errors of the regression adopting different degree for the fitting polynomials.

Table 20 - Least squares error of the polynomial fitting

$P(x)$ degree	**E-scooter**		
	Aprilia ESR2	**Xiaomi Pro II**	
	Pneumatic	Pneumatic	Solid
1	1152.8	866.5	1172.3
2	85.1	10.0	164.6
4	0.6	1.8	10.8

As highlighted by Figure 21 and Table 20, the polynomial of fourth degree is the most suitable to represent the force-displacement characteristic. Figure 22 shows the comparison in terms of stiffness adopting the different polynomials.

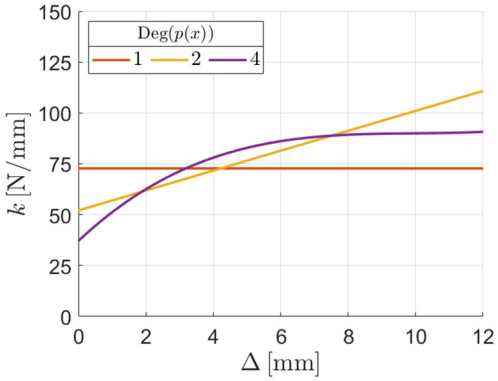

Figure 22 - Estimated stiffness fitting force-displacement data with polynomials of 1st, 2nd and 4th degree

In order to achieve a more accurate estimation of the tyre stiffness, the wheel hub displacement read on the dial indicator at the end of the test, $\delta_{s,max}$, is used. Indeed, the displacement of the crossbar is the sum of the deflections of the tyre and the deflection of the support elements. In other words, the bolts used to clamp the wheel cannot be considered infinitely rigid. Firstly, the real vertical displacement of the wheel hub is computed.

$$z_{s,max} = \frac{\delta_{s,max}}{\cos(48°)}$$

(5)

It is reasonably assumed a constant stiffness of the support elements, k_s, and so a linear increase of the support element deflection with the vertical force.

$$k_s = \frac{\max(F)}{z_{s,max}}$$

(6)

Table 21 - Stiffness of the tyre support

	E-scooter		
	Aprilia ESR2	**Xiaomi Pro II**	
	Pneumatic	Pneumatic	Solid
k_s [N/mm]	3668	25786	1742

Different values of stiffnesses are calculated since the clamping system used in the several configurations is different. The corrected tyre deflection Δ is computed in Eq.(7).

$$\Delta_0 = \Delta - F/k_s$$

(7)

Figure 23 represents the comparison between the force-tyre deflection characteristics assuming the support element as infinitely rigid or elastic.

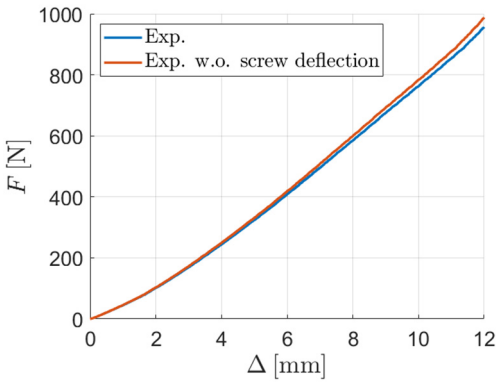

Figure 23 - Force against deflection considering the flexibility of the support

The tyre stiffness is again computed and plotted against the vertical force in Figure 24.

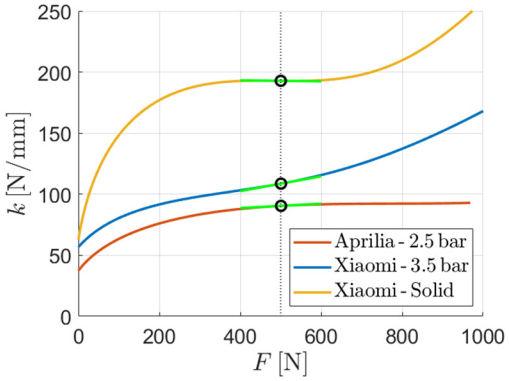

Figure 24 - Stiffness comparison

In Figure 24 the reference vertical force of 500 N and the relative stiffnesses are highlighted. Aprilia tyre is characterised by the smallest stiffness: it increases less than linearly for low values of force and tends to an asymptote. Xiaomi pneumatic tyre is characterised by an increasing stiffness in the analysed force range. In correspondence of the reference vertical force, the stiffness is almost linear. Xiaomi solid rubber tyre stiffness rapidly increases at the beginning; the stiffness is almost constant in correspondence of the reference vertical load; then it starts growing again. Xiaomi pneumatic tyre is also tested adopting the air pressure of 2.5 bar. The comparison in terms of stiffness with respect to the nominal air pressure is reported in Figure 25.

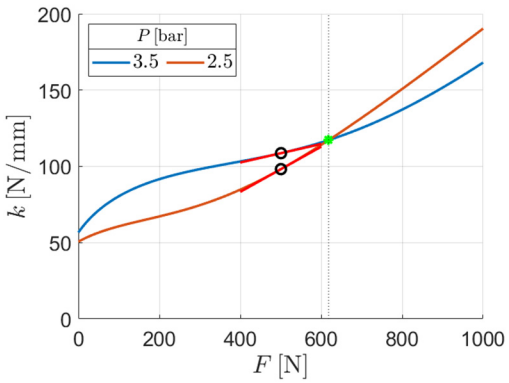

Figure 25 - Xiaomi pneumatic tyre stiffness for two different air pressures

At the reference vertical force of 500 N, the stiffness at 2.5 bar is lower than at 3.5 bar; at the same time the increasing rate is larger. The stiffness becomes higher for 2.5 bar with vertical force higher than 618.5 N. Eqs (8) and (9) are the polynomials used to represent respectively the vertical force and the stiffness against the tyre deflection.

$$F = f_1 + f_2\Delta + f_3\Delta^2 + f_4\Delta^3 + f_5\Delta^4 \tag{8}$$

$$k = f_2 + 2f_3\Delta + 3f_4\Delta^2 + 4f_5\Delta^3 \tag{9}$$

Table 22 reports the coefficients included in Eqs (8) and (9).

Table 22 - 4th polynomial coefficients for force and stiffness computation

$P(x)$ degree	E-scooter			
	Aprilia ESR2	**Xiaomi Pro II**		
P_t [bar]	2.5	2.5	3.5	Solid
f_1 [N]	0	0	0	0
f_2 [N/mm]	37.373	50.597	56.6540	62.784
f_3 [N/mm^2]	8.154	3.750	10.746	64.592
f_4 [N/mm^3]	−0.541	−0.445	−1.293	−14.175
f_5 [N/mm^4]	0.014	0.043	0.076	1.160

Tests are repeated assigning a constant crossbar velocity for the Xiaomi pneumatic tyre. Figure 26 represents the resulting stiffnesses versus the vertical force for different crossbar velocities.

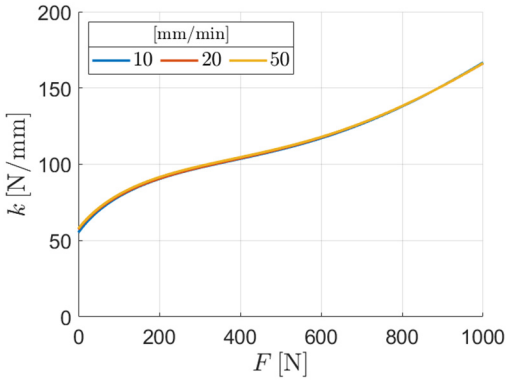

Figure 26 - Xiaomi tyre stiffness (3.5 bar) for different crossbar velocities

As evidenced by Figure 26, a very small stiffening effect occurs increasing the velocity of the load application. Similar results are obtained with the air pressure of 2.5 bar.

2.4 Rider data

If not differently specified, the experimental tests are conducted by a reference rider whose main data are reported in Table 23.

Table 23 - Reference rider data

Height [m]	1.80
Mass [kg]	80
BMI [kg/m^2]	24.69
Age	27
Gender	M

The rider has good experience in driving electric kick scooters and is right-handed.

Chapter 3

Longitudinal dynamics

In this chapter the experimental analyses and the numerical modelling aimed at characterizing the longitudinal behaviour of the electric scooter are described [56]. The presented research work is conducted taking into account Xiaomi Pro II electric scooter and the reference rider.

Paragraph 2.1 is dedicated to the experimental setup and the common part of the data processing. Paragraph 2.1 is focused on the three longitudinal manoeuvres, i.e., the standing start, the coasting and the braking. Paragraph 2.3 deals with the development of a simplified lumped parameter model used to demonstrate the influence of the rider motion on vehicle performance. A sensitivity analysis on the main model parameters follows.

3.1 Sensor setup and data processing

Figure 27 represents the sensor setup involved in the experimental campaign.

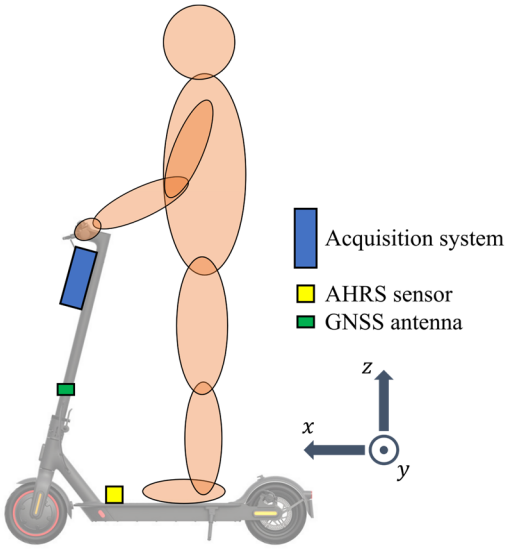

Figure 27 - Experimental setup for the longitudinal experimental tests

The experimental setup is constituted by:

- Siemens SCADAS XS as acquisition system;
- SBG Ellipse A AHRS inertial unit;
- GNSS antenna.

The acquisition system is Siemens SCADAS XS. It is placed together with the cables and the LiPo battery which powers SBG Ellipse A inside a dedicated plastic case fixed on the steering handlebar and column by velcro strips. This device synchronously acquires the signals coming from SBG Ellipse A and the GNSS antenna. The first sensor is clamped on the deck of the e-scooter; it integrates a tri-axial accelerometer, a tri-axial gyroscope and a tri-axial magnetometer. Thus, the device is able to directly measure the acceleration and angular velocity components along its three reference axes as well estimate its global orientation. In this experimental campaign, SBG Ellipse A is used to monitor the vehicle longitudinal acceleration $\ddot{x}_S$ with a sampling frequency of 200 Hz. The connection to the acquisition system is achieved via Controller Area Network (CAN) protocol with a rate of 10^6 baud. A Global Navigation Satellite System (GNSS) antenna, belonging to Siemens SCADAS XS accessories, is used

to record the position of the vehicle in terms of latitude $\Delta\phi_G$ and longitude $\Delta\lambda_G$ with a sampling frequency of 4 Hz. The acquisition system uses the global position to provide a raw estimation of the velocity v_G. Since the tests involve only longitudinal dynamics, the vehicle velocity exactly corresponds to the longitudinal velocity $\dot{x}_G$. The antenna is mounted on a secondary handlebar placed in the middle of the steering column. The total mass of the devices and mounting accessories is smaller than 2 kg, equal to 2.5 % of the mass represented by rider-vehicle system; hence, it is neglected in the post-processing and in the numerical simulations. The signal acquisitions are manually started and stopped (Free-run mode) using a Tablet (SCADAS tablet mode). Tests are conducted by two people, the rider and a person who is responsible of the signal recording. More details on the devices used during this experimental campaign are provided in Appendix A. The data processing is conducted in Matlab R2022a. A digital low-pass band filter is used to reduce the signal noise of $\ddot{x}_S$. The cut-off frequency is equal to 6 Hz. Figure 28 represents the original longitudinal acceleration detected by SBG Ellipse A and the filtered one.

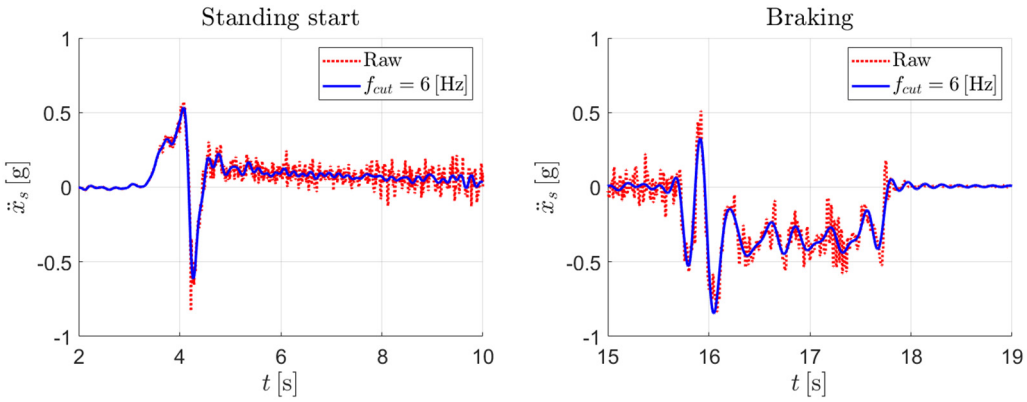

Figure 28 - Raw and filtered longitudinal acceleration in two different manoeuvres

$\Delta\phi_G$ and $\Delta\lambda_G$ are provided to Matlab Mapping Toolbox in order to compute the cumulative travelled distance x_G. Figure 29 represents the track based on $\Delta\phi_G$ and $\Delta\lambda_G$ (left panel) and the corresponding cumulative travelled distance (right panel).

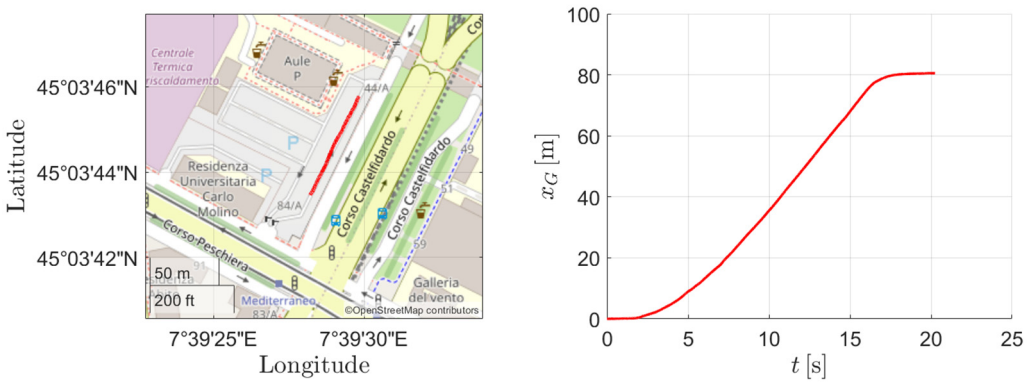

Figure 29 - Track (left) and cumulative travelled distance (right) of a generic acquisition

It is noticed that the GNSS antenna sampling frequency, which represents a fixed parameter of the acquisition system, is not suitable to measure the phenomena of interests. Moreover, x_G and $\dot{x}_G$ seems delayed respect to the real vehicle distance and velocity and affected by relevant error at very low velocity. Direct integration of $\ddot{x}_S$ to compute a longitudinal velocity estimation is not possible because of consistent signal drift. For the abovementioned reasons, a linear Kalman filter [57,58] is designed and fed with raw experimental measurement $[x_G\ \dot{x}_G\ \ddot{x}_S]^T$ to compute more precise results. Process and measurement covariances are set to penalise x_G and $\dot{x}_G$.

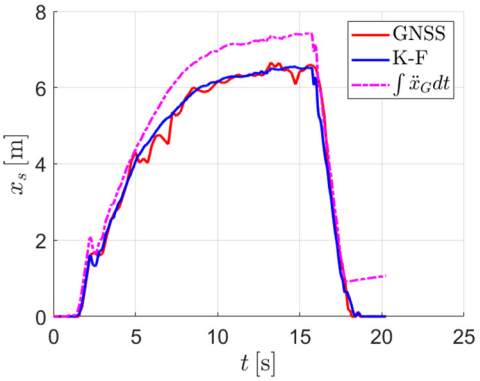

Figure 30 - Cumulative travelled distance computed from GNSS signals, after Kalman Filter application, by integration of the longitudinal acceleration

Output signals of the Kalman filter are finally triggered to assess the manoeuvre. More details on Kalman filter application in this case study are provided in Appendix B. From this point on in this chapter, the output velocity of

the Kalman filter will be named as $\dot{x}_s$ and subscript $_s$ will refer to all e-scooter magnitudes.

3.2 Test procedure and experimental results

The experimental tests conducted to analyse the longitudinal dynamics of the electric kick scooter can be divided into three main categories:

- standing start and acceleration;
- coasting;
- braking.

In this paragraph the test protocol and the most relevant results related to the three test categories are discussed.

3.2.1 Standing start and acceleration

The purpose of these tests is to investigate the electric motor performance in the driving modalities M_d and the gestures which characterise the standstill start. At the beginning of the manoeuvre, the rider is at the left of the vehicle, with his right foot on the deck floor and the left foot on the ground. The left foot is pushed onto the ground in order to increase the vehicle velocity till overcoming the threshold of almost to 1.4 m/s. The left lower limb is brought onto the deck and the accelerator is pushed in order to activate the motor. In most electric scooters, it is not possible to accelerate the vehicle from standstill or when the velocity is under a certain threshold for safety reasons, i.e., pushing the accelerator lever when the vehicle is completely stopped does not produce any effect.

Figure 31 - Five snapshots of the standing start manoeuvre

The standing start manoeuvre is tested varying two different parameters:

- the electric motor modes M_d, i.e., Eco mode (E) and Sport mode (S);
- rider foot position, P_{x1} and P_{x2}.

It is preliminary assumed that:

- M_d could influence not only the maximum velocity (equal to 20 km/h and 25 km/h in E and S modes according to the technical specifications) but also the vehicle acceleration;
- varying the rider foot position, and consequently the rider centre of mass longitudinal location, could impact the longitudinal performance due to the different load distribution.

Each configuration is tested five times in order to check result repeatability. Tests are synchronized on the basis of the maximum of the longitudinal acceleration. Figure 33 represent the longitudinal acceleration and velocity of the e-scooter adopting E (blue dash-dot lines) and S (red solid lines) motor modalities.

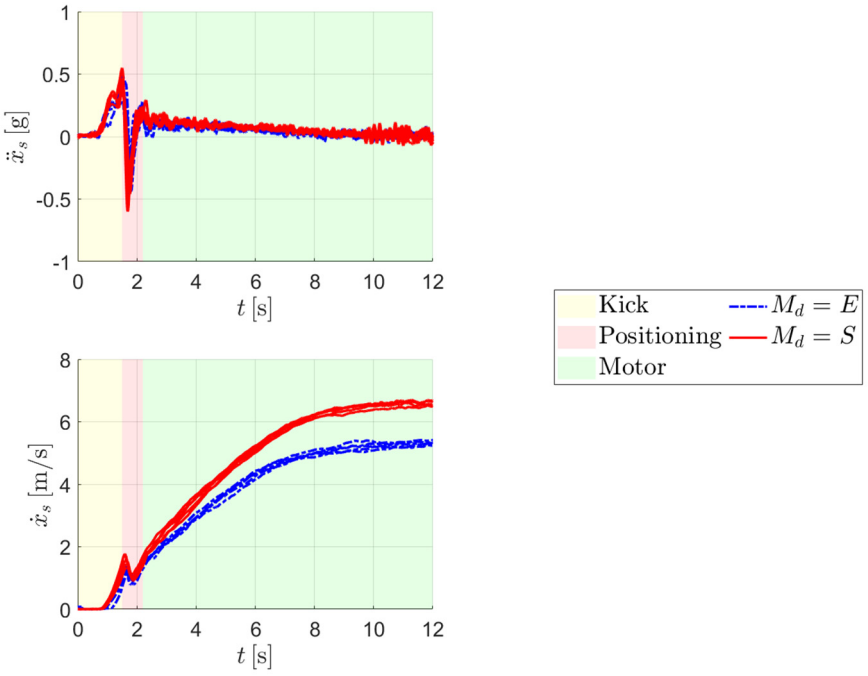

Figure 32 - Acceleration and velocity varying the driving motor mode

As highlighted by Figure 32, the experimental results are repeatable. As initially supposed, the electric motor modality M_d impacts on the e-scooter performance both in terms of maximum velocity, which is almost in line with the technical specification, and acceleration. The maximum velocity is equal to 19.3 km/h and 23.7 km/h respectively in E and S mode, slightly lower than the expected value. Analysing Figure 32, three main phases can be highlighted in the standing start manoeuvre:

- rider kicking (in yellow);
- rider body adjustment (in pink);
- electric motor driving torque (in green).

The kicking phase is characterized by an increasing longitudinal acceleration which is the result of the contact tangential force applied by rider on the ground. At the end of the kicking phase, the maximum value of longitudinal acceleration in the whole manoeuvre is calculated. The average maximum value is equal to 0.42 g. The second phase is characterized by the rider's body settling and the small delay between the end of the kick and the pushing of the accelerator. In this phase the acceleration is negative and reaches the lowest value. The average minimum is equal to -0.34 g. Experimental acceleration and velocity are quite similar in the two motor modalities since they depend only on the rider gestures and not on the e-scooter settings. The trends of the two signals are also experienced performing standing start tests without acting on the throttle. The motor torque action is visible by the change of the velocity slope, at the beginning of the green area in the velocity plot. In order to compare the acceleration of the motor adopting the two different modalities, the average time necessary to increase the velocity from 7 km/h to 17 km/h is assessed. The velocity bounds are chosen in order to consider only the effect of the motor.

Table 24 - Elapsed time to increase e-scooter velocity adopting the two motor modes

	M_d	
t_{7-17} [s]	4.2	2.9

Standing start tests aiming at evaluating the effect of rider position evidence sufficient repeatability but negligible differences.

3.2.2 Coasting

Coasting tests consist of achieving the maximum velocity then letting the vehicle free to move forward, progressively decelerating due to the resistance forces. Road slope and bank angle of the testing area are measured by an inclinometer (accuracy of $\pm$ 1°), and result to be negligible. The stretch of road is characterized by homogeneous asphalt, free of macroscopic unevennesses (potholes and bumps). The abovementioned points ensure that the vehicle deceleration is due to just vehicle motion resistances. Two operative parameters are varied during the tests:

- the electric motor regenerative modalities M_e;
- the tyre inflation pressure P_t.

In the following, M_e equal to 0 corresponds to the case in which the vehicle is switched off: no regenerative braking torque is applied to the wheel. Light, medium and strong regenerative mode corresponds to M_e equal to 1, 2 and 3. Each configuration is tested ten times and results are averaged. The dynamic equilibrium along the longitudinal direction during this kind of manoeuvre can be written according to Eq.(11),

$$\bar{R} = -(m_r + m_s)\ddot{x}_s \tag{10}$$

where:

- $\bar{R}$ represents the overall resistance force;
- m_r represents the mass of the rider;
- m_s represents the mass of the e-scooter;
- $\ddot{x}_s$ is the vehicle longitudinal acceleration.

The overall resistance force $\bar{R}$ can be written as sum of four terms (Eq.(11)),

$$\bar{R} = R_f + R_r + D + \frac{T_r}{r_t} \tag{11}$$

where:

- $R_{f/r}$ is the resistance force due to front and rear tyre rolling;
- D is the aerodynamics drag;
- T_r is the regenerative braking torque applied by the electric motor;
- r_t is the tyre radius (Table 5).

The following assumptions are preliminarily made with respect to the vehicle velocity $\dot{x}_s$ in order to identify the motion resistances ($R_{f/r}$ and D) and the motor torque (T_r):

- R_f and R_r are constituted by the sum of two contributions, i.e., a constant and a term dependent on the square of $\dot{x}_s$ (it is afterwards verified that the linear term is negligible);
- R_f and R_r can be affected by the tyre inflation pressure P_t;
- D depends only on the square of $\dot{x}_s$;
- T_r is independent on $\dot{x}_s$ and can be affected by M_e.

According to these hypotheses, Eq. (11) can be rewritten as Eq. (12),

$$\bar{R} = \bar{A} + \bar{B}\dot{x}_s^2 \tag{12}$$

Setting Eq. (12) equal to Eq. (10), coefficients $\bar{A}$ and $\bar{B}$ are identified in the velocity interval from 5 m/s to 2 m/s: in this way the initial and the final parts of the manoeuvre are excluded from the assessment. Figure 33 reports the average $\bar{A}$ (left panel) and $\bar{B}$ (right panel) coefficients for the different motor regenerative modalities M_e.

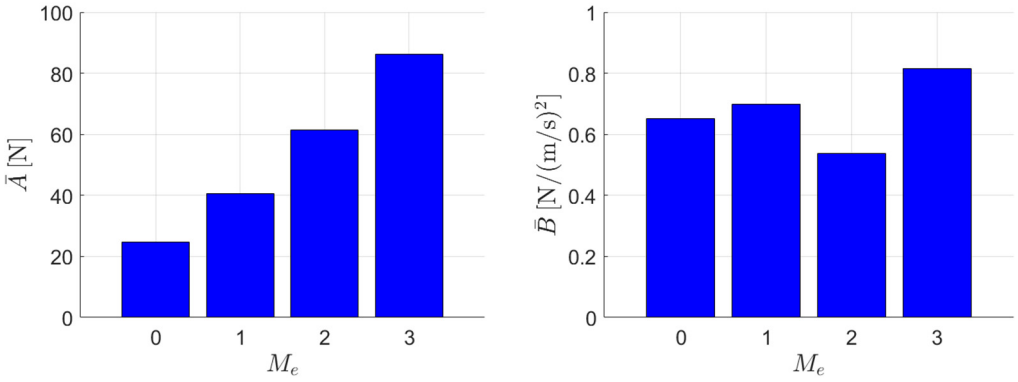

Figure 33 - Averaged resistance coefficients varying the regenerative mode

The following consideration can be underlined:

- $\bar{A}$ depends on M_e;
- $\bar{B}$ seems to be not affected by M_e.

Consistent with the abovementioned hypotheses, it follows that the regenerative torque T_r is not dependent on the vehicle velocity since the only parameter which is varying is M_e. It is also noticed that $\bar{B}$ contribution is significantly lower than $\bar{A}$, highlighting a small dependency of the resistance force on the vehicle velocity. This evidence is reasonable considering that the velocity range of the e-scooter is limited. Starting from the fitted $\bar{A}$ and $\bar{B}$ for different M_e, (Figure 33), the overall resistance force $\bar{R}$ is recomputed varying $\dot{x}_s$ from 0 m/s to 6 m/s using Eq. (12). Figure 34 represents the recomputed resistance forces versus the vehicle velocity.

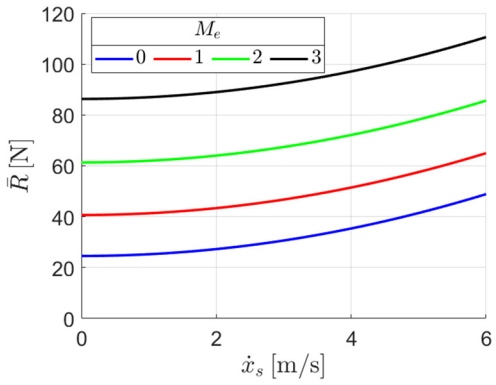

Figure 34 - Recomputed resistance force versus velocity varying the motor regenerative mode

As visible from Figure 34, the starting point of $\bar{R}$ ($\dot{x}_s = 0$ m/s) grows switching M_e from 0 to 3 due to the increasing T_r. The way in which $\bar{R}$ increases by effect of $\dot{x}_s$ is the same in the different configurations of M_e underlining that T_r remain constant once M_e is defined. Based on these considerations and the obviousness that the motor contribution occurs only in case of switched-on vehicle, the regenerative motor torque T_r is computed for the different M_e according to Eq. (13).

$$T_{r,i} = \left(\bar{A}_{M_e = i} - \bar{A}_{M_e=0}\right) r_t \qquad i = 1,2,3 \tag{13}$$

Results are reported in the coasting panel of Figure 43 dealing with the motor modelling. The second purpose of the coasting manoeuvre is assessing the effect of the tyre inflation pressure P_t. It is preliminary supposed that the vehicle resistance force decreases increasing the tyre inflation pressure due to a sensible reduction of the front and rear wheel rolling resistance. Four pressures are tested, from 2.5 to 4 bar with a step of 0.5 bar. The same pressure is simultaneously adopted for the front and rear tyre. The accuracy of the compressor used to inflate the tyres is 0.1 bar. The tests are conducted adopting M_e equal to 1. The motor contribution is subtracted from the results to evaluate the net resistance force R. Eq. (11) is rewritten to obtain R.

$$R = R_f + R_r + D = \bar{R} - \frac{T_r}{r_t} \tag{14}$$

Eq. (15) follows rearranging Eq. (12).

$$R = A + B\dot{x}_s^2 \tag{15}$$

As previously demonstrated, the regenerative torque is independent of the vehicle velocity (Figure 33); A and B coefficients can be obtained by the relations reported in Sys. (16).

$$\begin{cases} A = \bar{A}_{M_e = 1} - \dfrac{T_{r,\,M_e = 1}}{r_t} \\ B = \bar{B}_{M_e = 1} \end{cases} \tag{16}$$

The dependency of the net average coefficients A and B with respect to the tyre inflation pressure is reported in Figure 35. Magenta squares are the experimental data in correspondence of the tested tyre pressures. The experimental points are fitted with a 1^{st} degree polynomial in P_t (solid blue line). $P_{t,0}$ represents the nominal tyre pressure, equal to 3.5 bar (dot-dot black line).

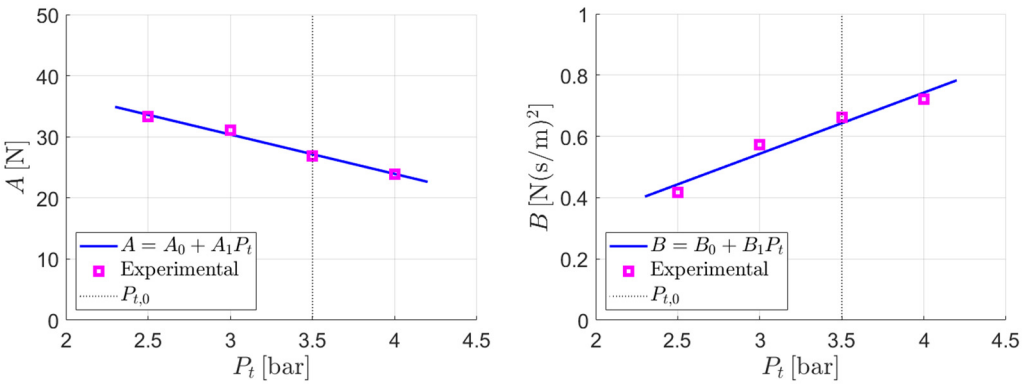

Figure 35 - Net resistance coefficients varying the tyre pressure

As visible from Figure 35, A and B coefficients seem to decrease and increase with P_t, respectively. These experimental results can be considered valid in the tested tyre pressure range. As previously done for M_e, the net resistance force R is recomputed in function of the velocity $\dot{x}_s$ varying the tyre pressures P_t using the identified A and B coefficients (Figure 36).

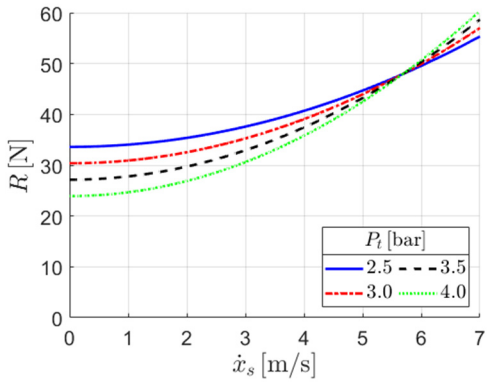

Figure 36 - Recomputed net resistance against velocity varying the tyre pressure

The highest gap in terms of resistance is detected for low velocities; the resistance force increases decreasing the tyre pressure. Increasing the vehicle velocity, the difference gradually reduces.

3.2.3 Braking

The braking manoeuvre analysis aims at evaluating the following aspects of the electric scooter:

- the influence of rider position (P_{x1} and P_{x2}), road condition (dry or wet) and tyre inflation pressure P_t;
- the braking performance varying the braking level S_b;
- the regenerative braking torque T_r applied by the electric motor to the front wheel varying the regenerative modalities M_e.

All the braking tests are carried on the same asphalted stretch of road characterized by negligible slope and bank angle. Apart from the tests in which tyre inflation pressure is investigated, the nominal value $P_{t,0}$ is adopted. In the same way, rider position P_{x2} is used if not differently specified. The braking manoeuvre is performed always driving in longitudinal up to the vehicle maximum velocity and then pulling the braking lever according to the braking level of the test. Heavy braking manoeuvre corresponds of the case in which the braking lever is completely pulled; the time of actuation is the shortest possible. In order to perform a homogeneous comparison between the several conditions, the average deceleration $|\bar{\ddot{x}}_s|$ is assessed neglecting the initial and the final parts of the manoeuvre. The phase in which $|\bar{\ddot{x}}_s|$ is evaluated is highlighted in red in the following diagrams.

Figure 37 refers to the heavy braking manoeuvre adopting P_{x1} and P_{x2} rider position (left panel) and on dry and wet asphalted road (right panel).

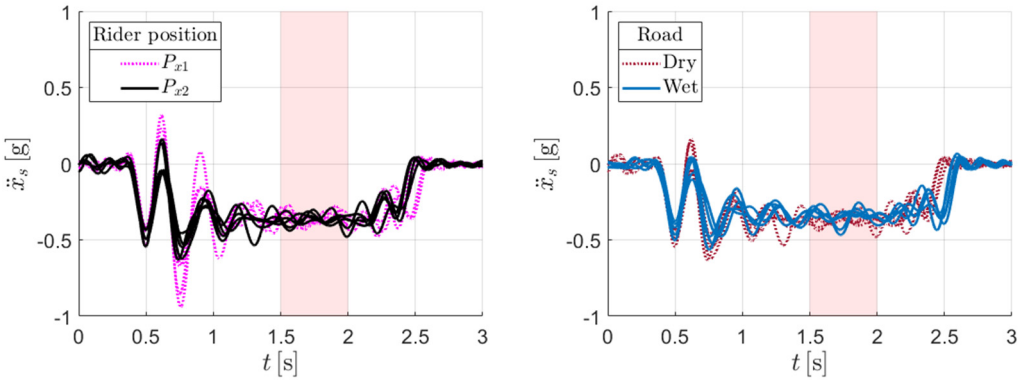

Figure 37 - Longitudinal acceleration in the heavy braking tests varying the rider position (left) and road wet condition (right)

A common feature of all the heavy braking tests is the locking of the rear wheel. At the beginning of the braking manoeuvre, relevant oscillations in terms of longitudinal acceleration always occur. As it will be demonstrated by the support of the simulation, the acceleration oscillations are due to the inertia of the

rider and his relative motion with respect to the vehicle. The oscillation amplitude is on average higher for P_{x1} probably because of rider's posture and the distance between the chest and the handlebar, which implies a different human body response. The average modulus of the acceleration is respectively 0.35 g for P_{x1} and 0.37 g for P_{x2}. The difference can be reconducted to the different vertical load distribution between the front and the rear wheel. The average modulus of the acceleration is respectively 0.37 g on dry asphalt and 0.34 g on wet asphalt. Oscillation amplitudes are comparable in the two cases. A common characteristic of the heavy braking tests stands in the locking of the rear wheel. In Figure 38, the longitudinal acceleration $\ddot{x}_s$ versus time adopting different braking level S_b is reported.

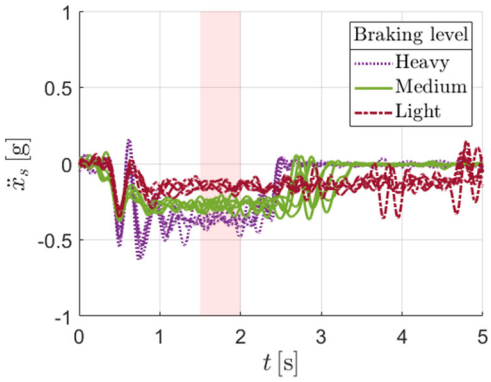

Figure 38 - Longitudinal acceleration in the heavy, medium and light braking tests

In this analysis, the braking level S_b is not directly measured but evaluated by the rider during the tests from his experience. S_b is intended as the normalised braking command, from 0 to 1, where 0 corresponds to no braking condition and 1 corresponds to the complete braking. Three different situations are compared, i.e., heavy, medium and light braking. As expected, different decelerations are achieved with different braking command (Table 25). Longitudinal acceleration oscillations in the initial part of the braking vary with the braking severity. Higher oscillations correspond to heavier braking level. The locking of the rear wheel does not occur in the case of light and medium braking.

Table 25 - Braking manoeuvre summary varying the braking command

Braking level	S_b [-]	$\lvert\bar{\ddot{x}}_s\rvert$ [g]
Light	< 0.05	0.15
Medium	~ 0.5	0.27
Heavy	1	0.37

The longitudinal acceleration $\ddot{x}_s$ versus time adopting different regenerative electric motor modalities M_e is also assessed in the heavy braking manoeuvre (left panel in Figure 39). For the sake of clarity, a single acceleration signal for each regenerative modalities is reported on the understanding that the tests are repeatable. No difference is detected when the vehicle is switched-on, concluding that the torque applied by the electric motor during the braking manoeuvre is independent of M_e. The manoeuvre is also performed switching off the vehicle ($M_e = 0$): it is detected an average longitudinal acceleration of 0.26 g. The gap of almost 0.11 g in terms of $\lvert\bar{\ddot{x}}_s\rvert$ with respect to the switched-on vehicle must be attributed to the electric motor. It is also noticed that rear wheel never locks during heavy braking with the vehicle turned off, due to the lower load transfer produced by the lower deceleration. Heavy braking tests are finally performed varying the tyre inflation pressures (right panel in Figure 39): results do not highlight relevant differences.

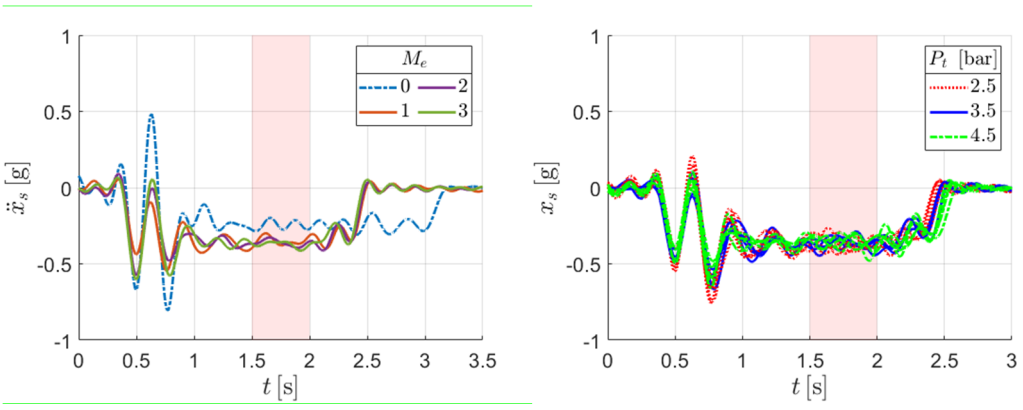

Figure 39 - Longitudinal acceleration in the heavy braking tests varying the regenerative electric motor modalities (left) and tyre pressure (right)

3.3 Lumped parameter modelling and simulation

In this paragraph, a simplified lumped parameter model able to describe the longitudinal dynamics of the electric scooter is discussed. The first target of this phase is characterising the unknown parameters of the vehicle. The second aspect to be investigated is the interaction between the rider and the vehicle during the braking manoeuvre. In the first subparagraph the development of a 3-DOF model is discussed. In the second subparagraph, the simulation of the standing start manoeuvre is presented. In the third subparagraph the braking manoeuvre is analysed switching the model to 4-DOF.

3.3.1 3-DOF model

Matlab/Simulink R2022a and Simscape toolbox are used to develop the models. The first model, whose free body diagram is reported in Figure 40, is constituted by three degrees of freedom (3-DOFs), respectively:

- the translational motion of the vehicle-rider system x_s;
- the angular motion of the front wheel θ_f;
- the angular motion of the rear wheel θ_r.

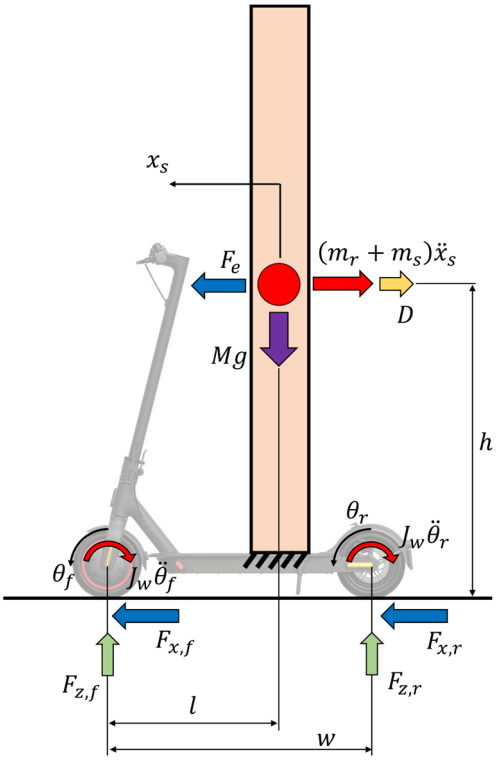

Figure 40 - 3-DOF longitudinal model

The total mass is lumped in correspondence of the centre of mass of the whole system. Mass distribution and center of mass locations have been already discussed within subparagraph 2.2.2. The longitudinal motion of the system, x_s, is computed from the translational dynamic equilibrium. Vertical load on the tyres is computed considering the static load distribution and the load transfer due to the aerodynamic drag D and the inertial force $(m_s + m_r)\ddot{x}_s$. In the absence of detailed analyses, the aerodynamic drag D is supposed to be applied in correspondence of the center of mass of the whole system; in terms of height, this point almost coincides with the middle of the frontal area. Pitch motion is not included in the model. The angular motions, θ_f and θ_r, are computed solving the rotational dynamic equilibrium of the wheels: the wheel-tyre system moment of inertia, equal to 0.008 kgm^2, is taken from the CAD model. $F_{x,f}$ and $F_{x,r}$ are the longitudinal forces developed by the tyre at the front and at the rear. They are modelled, according to a simplified release of the Pacejka longitudinal formulation [59]: they are dependent on the vertical load acting on the tyre, $F_{z,f}$ and $F_{z,r}$, and the longitudinal slip, σ_f and σ_r.

$$\sigma_{f/r} = 1 - \frac{\dot{\theta}_{f/r} r_t}{\dot{x}_s}$$

(17)

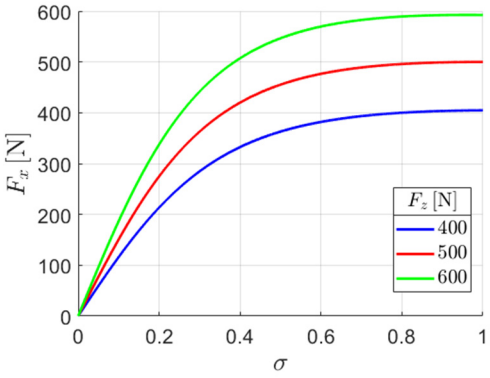

Figure 41 - Tyre longitudinal force in function of the longitudinal slip and the vertical force

The external longitudinal force F_e in Figure 40 is used to simulate the rider kick in the standing start.

Resistance forces

The front and the rear rolling resistances are computed according to Eq. (18),

$$R_{f/r} = F_{z,f/r}(a + b\dot{x}_s^2)$$

(18)

where a and b are coefficients depending on the tyre air pressure, computed according to Sys. (19).

$$\begin{cases} a = a_0 + a_1 P_t \\ b = b_0 + b_1 P_t \end{cases}$$

(19)

The coefficients in Sys. (19) and reported in Table 26 are computed from the experimental results (Figure 35).

Table 26 - Rolling resistance coefficients depending on tyre air pressure and normalised by the vertical load

a_0 [-]	$7.08 \cdot 10^{-2}$
a_1 [1/bar]	$-1.11 \cdot 10^{-2}$
b_0 [s^2/m^2]	$-3.82 \cdot 10^{-4}$
b_1 [s^2/(m^{2}bar)]	$2.14 \cdot 10^{-4}$

The aerodynamic drag D is computed according to Eq. (20).

$$D = \frac{1}{2}\rho c_D A_D \dot{x}_s^2 \tag{20}$$

Parameters in Eq. (20) are computed from the experimental results and Acarer's work [60].

Table 27 - Aerodynamics parameters

Parameter	**Description**	**Value**
ρ [kg/m^3]	Air density	1.21
c_D [-]	Drag coefficient	0.76
A_D [m^2]	Frontal area	0.68

Mechanical braking

The mechanical braking system, which is a braking disc at the rear wheel in Xiaomi Pro II, is modelled as the torque T_b, (Eq. (21)):

$$T_b = 2\mu_b N_b r_b \tag{21}$$

The multiplier equal to 2 is used since the mechanical braking system consists of 2 pads. Parameters included in Eq. (21) are reported in Table 28.

Table 28 - Mechanical braking parameters

Parameter	Description	Value
μ_b [-]	Pad friction coefficient	0.3
N_b [N]	Normal force to disc	From 0 to 800
r_b [m]	Disc effective radius	0.06

μ_b is assumed considering that low-cost materials used to manufacture pads are characterised by friction coefficient between 0.25 and 0.35 [61]. N_b is proportional to the force exerted by the rider to the braking lever, hence to the braking signal S_b. It is assumed a maximum normal force equal to 800 N since it corresponds to the minimum value able to reproduce the experimentally evidenced locking of the rear wheel in heavy braking manoeuvre. r_b is available from the e-scooter technical datasheet.

Electric motor and control unit

The electric motor model and the relative control is developed and tuned in order to match experimental evidence. Figure 42 represents the electric motor controller.

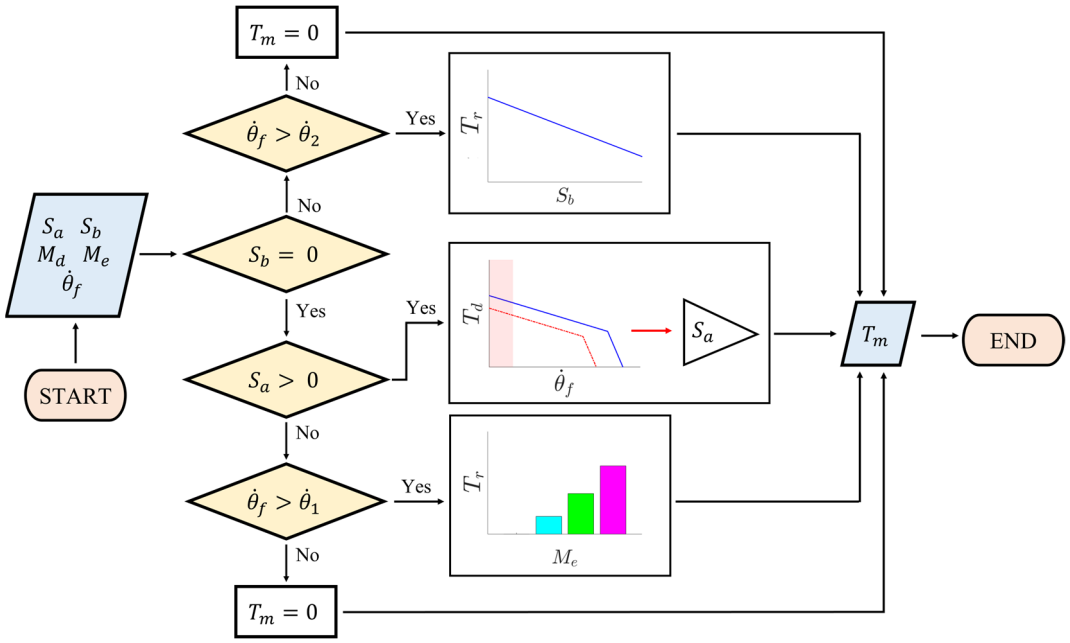

Figure 42 - Electric motor controller

The input of the controller are the accelerator and braking signals, S_a and S_b, the motor modes in driving and regeneration, M_d and M_e, the angular velocity of the front wheel, $\dot{\theta}_f$. S_b constitutes the first check to detect the braking. During braking ($S_b > 0$), the motor applies a negative braking torque T_r proportional to S_b up to the angular velocity lower bound of 80 rpm. On the contrary ($S_b = 0$), if S_a is positive and $\dot{\theta}_f$ is higher than 110 rpm, the motor applies a positive driving torque T_d dependent on S_a, M_d and $\dot{\theta}_f$. If the accelerator signal is null ($S_a = 0$), a constant negative braking torque T_r is applied depending on M_e up to the angular velocity lower bound of 130 rpm. Figure 43 represents the motor torque in driving, braking and coasting.

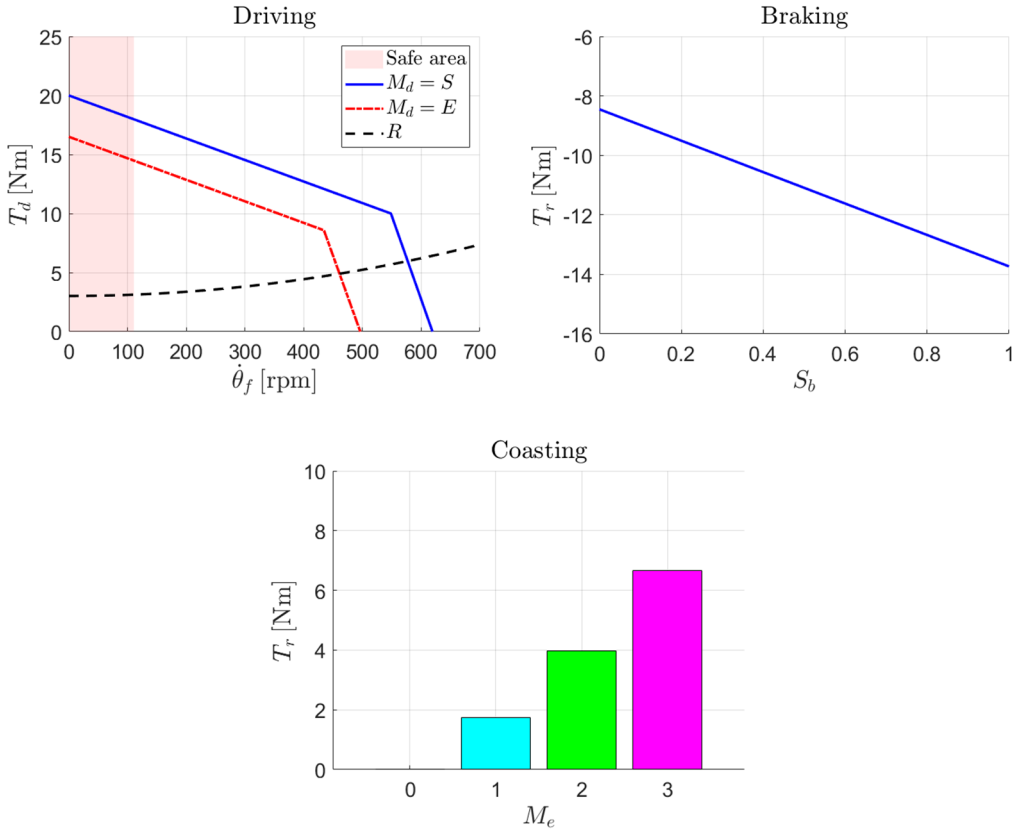

Figure 43 - Driving (T_d) and regenerative (T_r) torque of the electric motor in driving, braking and coasting

The driving torque characteristic T_d (Driving panel in Figure 43) depends on the angular velocity of the front wheel $\dot{\theta}_f$ and the motor mode in driving M_d. The blue solid line corresponds to the Sport mode (S) while the red dash-dot line to the Eco mode (E). The black dashed line represents the resistance force versus the front wheel angular velocity, in the reference load and tyre conditions. The safe area, evidenced in shaded red, is the angular velocity range in which the rider kick is required to start up the e-scooter. In other words, if the accelerator signal is not null ($S_a > 0$) but the $\dot{\theta}_f$ is within this angular velocity range (from 0 up to 110 rpm), no driving torque is applied by the electric motor. This control strategy implemented in the model represents what really happens in the standing start manoeuvre. The regenerative torque T_r in the braking manoeuvre (Braking panel in Figure 43) is proportional to the braking signal S_b and does not depend on the motor mode in regeneration M_e. The regenerative torque T_r in the coasting manoeuvre (Coasting panel in Figure 43) just depends on the motor mode in regeneration M_e.

Battery

Since no additional data are available for both motor and its drive, unitary efficiencies are assumed. The instantaneous power P_m, consumed or recovered by the motor, is computed according to Eq. (22).

$$P_m = T_m \dot{\theta}_f \tag{22}$$

The actual state of charge SOC is computed according to Eq. (23)(22).

$$SOC = SOC_0 - \frac{\int_{t_1}^{t_2} P_m dt}{E_b} \tag{23}$$

SOC_0 and E_b represent the initial state of charge and the total capacity of the battery respectively.

3.3.2 Standing start simulation

The 3-DOF model described in subparagraph 3.2.1 is firstly used to simulate the standing start manoeuvre. Figure 44 and Figure 45 represent the experimental-numerical comparison in terms of longitudinal acceleration $\ddot{x}_s$ (left panel) and velocity $\dot{x}_s$ (right panel). Figure 44 refers to the sport driving mode while Figure 45 refers to the eco driving mode of the electric motor.

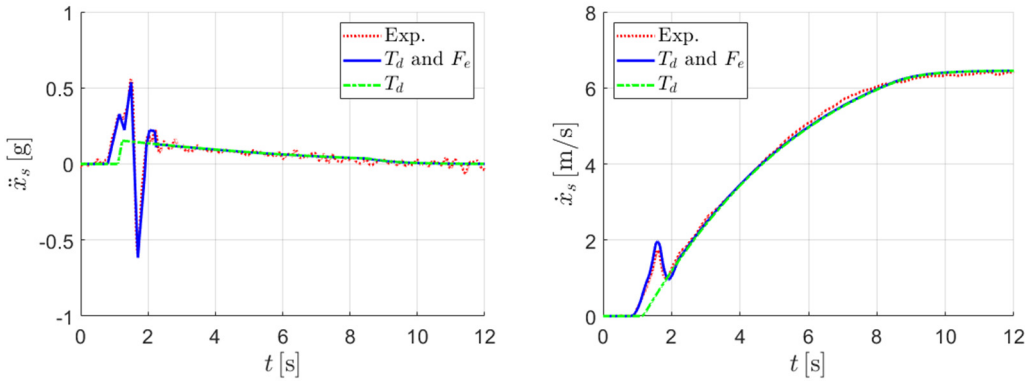

Figure 44 - Standing start simulation: experimental-numerical comparison in terms of longitudinal acceleration (left) and velocity (right) in Sport mode

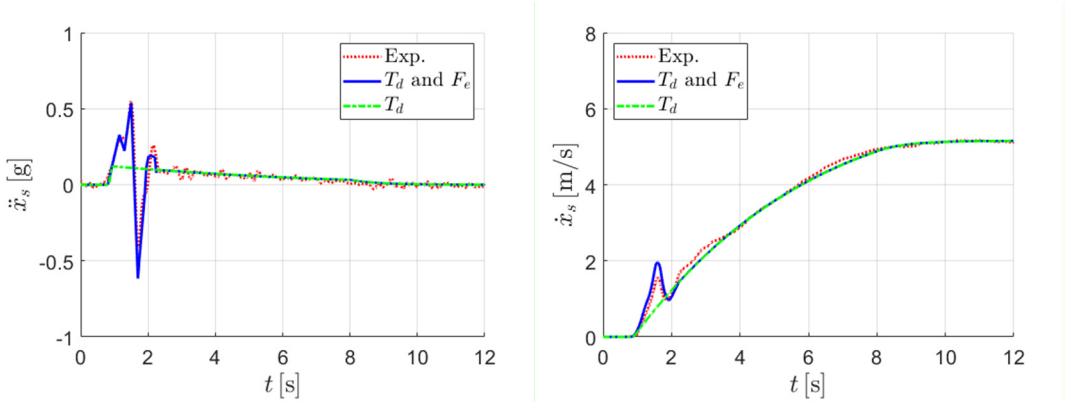

Figure 45 - Standing start simulation: experimental-numerical comparison in terms of longitudinal acceleration (left) and velocity (right) in Eco mode

Red dotted lines are used for the experimental accelerations and velocities; blue solid lines are used for the numerical results using as inputs the motor driving torque T_d and the external force corresponding to the rider kick and positioning F_e; dash-dot green lines are used for numerical results obtained only by the driving torque. The signal synchronisation is based on the vehicle velocity. A good correlation is achieved adopting both driving modes of the electric motor. It can be concluded that:

- the identified motor characteristics are able to represent the vehicle velocity profile in the acceleration manoeuvre;
- the beginning of the standing start manoeuvre is strongly influenced by the rider gestures.

3.3.3 4-DOFs model and braking simulation

An additional translational DOF is included in the model in the attempt of reproducing the experimental signals acquired in the braking manoeuvre tests. The mass of the rider (m_r) is separated by the mass of the vehicle (m_s). The locations of the centres of mass corresponding to the rider and the e-scooter have been already presented in subparagraph 2.2.2. Figure 46 represents the free body diagram of the 4-DOF version of the model.

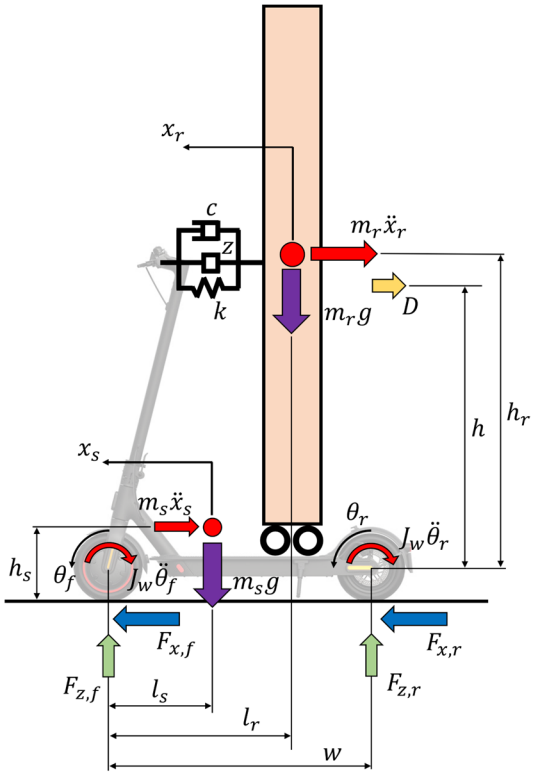

Figure 46 - 4-DOF longitudinal model

The translational degrees of freedom corresponding to the e-scooter (x_s) and the rider (x_r) are linked by means of lumped translational elements, i.e., stiffness k, damping coefficient c and inerter coefficient z. The assumption at the basis of the 4-DOF model is that the mass of the rider can have a relative longitudinal translation with respect to the mass of the vehicle. The lumped linking parameters aims at simulating the human body rigidity with respect to the vehicle. The real rider motion is more complex and kinematically depends on the human body joints as well the muscular response. The function of the inerter is to limit the relative acceleration between the two degrees of freedom associated to m_r and m_s. It is supposed at first that the inerter is replacing a sort of rider's active control on his muscular system with the purpose of reducing the relative motion with respect to the vehicle. As evidenced in paragraph 6.2 dealing with the same kind of manoeuvre simulated by the full multibody model, a passive anatomical rider (with stiffness and damping included in the joints) is able to reproduce the human body dynamics response. It follows that the inerter element constitutes an additional parameter of the lumped parameter model which covers the shortcomings due to the simplifying hypotheses. Coefficients k, c and z are kept constant during each simulation and tuned to match the experimental results.

Figure 47 reports the experimental-numerical comparison in terms of vehicle longitudinal acceleration in light (left panel) and heavy (right panel) braking manoeuvres.

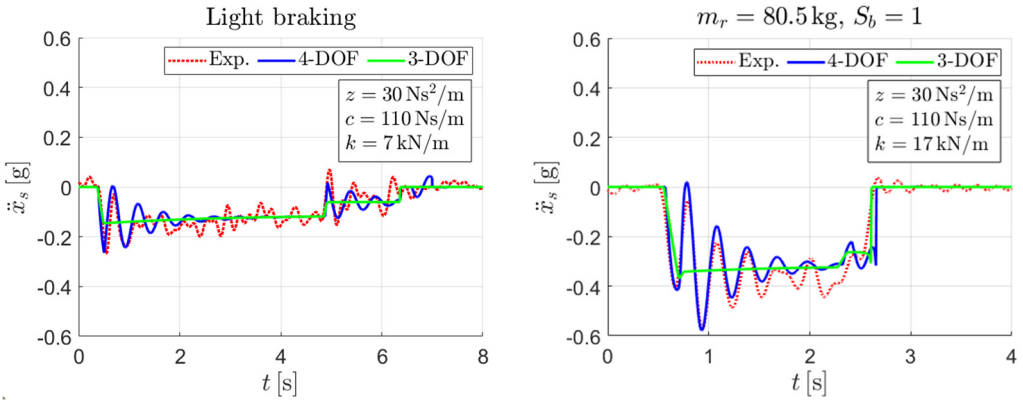

Figure 47 - Experimental-numerical comparison of the e-scooter acceleration in light (left) and heavy (right) braking

Keeping constant the masses of the vehicle (14.4 kg) and the rider (80 kg), k and z are tuned to fit the frequency of the system oscillations and the initial amplitude, while c is tuned to fit the amplitude decrease. As visible in Figure 47, different parameters are used in the two different manoeuvres, since the rider response varies. The rider seems to be stiffer and more damped during heavy braking.

A sensitivity analysis is then conducted on the 4-DOF model to evaluate the system response, varying k, c and z. Considering the system constituted by the two translational masses, m_r and m_s, and solving the real eigenvalue problem, the non-null natural frequency f_n is computed according to Eq. (24). The damping ratio ζ is computed according to Eq. (25).

$$f_n = \frac{1}{2\pi}\sqrt{\frac{k(m_r + m_s)}{(m_s + z)(m_r + z) - z^2}} \tag{24}$$

$$\zeta = \frac{c}{2\sqrt{k\left(\frac{m_s m_r}{m_s + m_r} + z\right)}} \tag{25}$$

In the first sensitivity analysis (Figure 48), k and z are varied. f_n and ζ are maintained constant and equal respectively to 3.2 Hz and 0.1 which are the experimental fitted values.

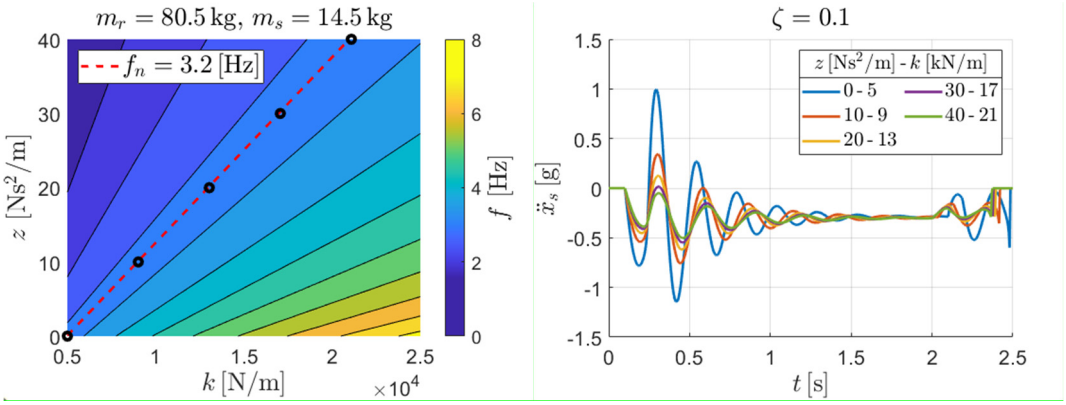

Figure 48 - Iso-frequency contour and numerical acceleration in the heavy braking varying the inerter coefficient and the stiffness

Red dashed line in the contour graph represents the iso-frequency line (3.2 Hz) varying k and z. The black circles represent the pairs of values used in the simulation. The main effect is the reduction of the initial oscillation amplitude in the longitudinal acceleration. Figure 49 represents the sensitivity analysis on ζ.

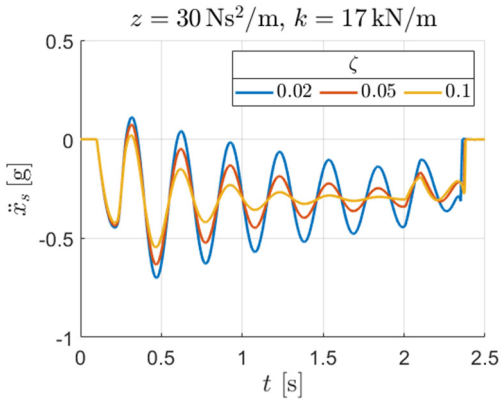

Figure 49 - Numerical acceleration in the heavy braking varying the damping ratio

Damping ratio ζ affects the oscillation decay but has no impact on the initial amplitude.

Chapter 4

Vertical dynamics

In everyday life, vehicles and working machineries are the main responsible of human body exposure to mechanical vibrations. Vibrations can be primarily classified according to their repeatability characteristic: they can be random, periodic or transient. The effects are manifold, such as feelings of discomfort and annoyance, affecting human capability, constituting a real risk for the human health. This chapter is focused on the assessment of vibrations perceived by a rider driving an electric kick scooter. Both the e-scooters available at DIMEAS are tested. The main source of vibrations is the road surface, which can be simply rough or have macro unevennesses such as bumps and potholes. The vehicle represents the means by which vibrations are transmitted to the rider's body. Vibrations are usually filtered by some vehicle components like tyres and suspension systems, according to their elasto-viscous properties. As regards the electric kick scooter, only some advanced models are equipped with basic suspensions, which can affect the comfort quality. Another important aspect to be remarked is that both perception and biological effects can vary from subject to subject. Thus, a quantitative and objective assessment of the human response to vibrations represents a very challenging task. ISO 2631-1 [62] and ISO 5349-1 [63] constitute the reference concerning the methodologies to quantify respectively whole-body and hand-transmitted vibrations. Even though the approach is similar, the vibration analysis follows different steps according to the purpose:

- health;

- comfort;
- perception;
- motion sickness.

In this research work, the attention is just focused on comfort aspects. ISO 2631-5 [64] is dedicated to whole-body vibrations containing shocks and their effects on human health. In biodynamics field, shock is intended as a short-time and high-magnitude vibration. Since this Standard is referred exclusively to the seated human posture, the proposed methodology is not used in this work.

This chapter presents the experimental analyses aiming at characterising and comparing the vertical dynamics of the two electric kick scooters. Paragraph 3.1 is dedicated to the sensor setup for the whole experimental campaign. Paragraph 3.2 deals with the tests carried out driving on a bike path characterised by seven speed bumps. Paragraph 3.3 deals with the e-scooter comfort comparison driving on homogeneous road surfaces such as asphalt and pavé.

4.1 Sensor setup

The sensor setup exploited in the experimental campaign is reported in Figure 50. The same instruments are used on both the e-scooters.

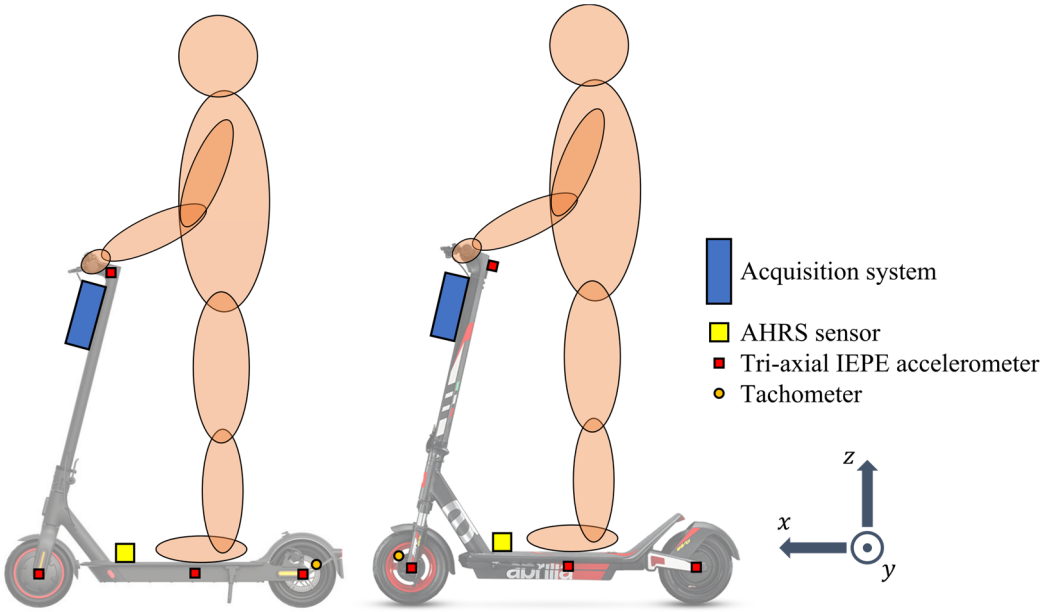

Figure 50 - Experimental setup for the vertical dynamics studies

The experimental setup consists of:

- Siemens SCADAS XS acquisition system;
- SBG Ellipse A AHRS inertial unit;
- four Kistler IEPE tri-axial accelerometers;
- Gebildet LJ12A3-4-Z proximity sensor.

The acquisition system together with the sensor cables and the battery which powers SBG Ellipse A and Gebildet LJ12A3-4-Z is placed inside a plastic case, fixed on the steering column and the handlebar by velcro strips. The signal acquisitions are manually started and stopped (Free-run mode) adopting the SCADAS standalone mode. SBG Ellipse A AHRS inertial unit is fixed on the deck floor. It is used to evaluate the vertical acceleration and the angular velocity around the vehicle y axis (pitch rate) with a sampling frequency of 200 Hz. The tri-axial accelerometers are used to detect the acceleration components in several points of the e-scooters. Two accelerometers are mounted in correspondence of the front and rear wheel centres. The target is to evaluate the vibration inputs from the ground and filtered by the tyres. As prescribed by ISO 2631-1 [62] and ISO 5349-1 [63], a good comfort assessment requires to evaluate vibrations as close as possible to the interface between the human body and the vibration source, which in this case is the vehicle. Since the interface surfaces are represented by the deck floor and the hands grip, a reasonable compromise between good sensor positioning and driving safety leads to place one accelerometer on the lateral side of the deck just under the feet and another one at the middle of the handlebar. Gebildet LJ12A3-4-Z proximity sensor is used as tachometer for measuring the wheel angular velocity. It is placed at the rear in Xiaomi Pro II setup and at the front in Aprilia ESR2 setup. Both accelerations and angular velocity are acquired with a sampling frequency of 3200 Hz. For more details on the acquisition system and the sensors used during the experimental campaign, refer to Appendix A.

4.2 Bump road tests

In this subparagraph the experimental tests conducted on the bike path with the seven speed bumps is discussed. Subparagraph 3.2.1 deals with the test procedure and the data processing. The main results are shown in subparagraph 3.2.1. All the tests here described have been carried out by the reference rider. For more details see paragraph 2.4.

4.2.1 Test procedure and data processing

The test consists of driving at constant velocity the e-scooter on a bike path characterised by the presence of seven bumps, equal and evenly spaced.

Figure 51 - Bike path with the seven bumps

Cruise control is exploited to keep constant the velocity. Five different target velocities $\bar{v}$ are tested, from 5 km/h to 25 km/h, with a step of 5 km/h. Each velocity is tested five time at least in order to verify repeatability.

Data processing is carried out in Matlab R2022a. Signals from SBG Ellipse A and Kistler accelerometers are rotated in order to get the alignment with the vehicle reference frame. All the signals are resampled with a sampling frequency of 3200 Hz in order to work with a common time base. The angular velocity of the wheel, ω_r, is filtered with a low-pass band filter (cut-off frequency equal to 4 Hz) and used to estimate the vehicle velocity $\dot{x}_s$ by Eq. (26)

$$\dot{x}_s = \omega_r r_t \tag{26}$$

where r_t is the tyre radius (Table 5). The vehicle velocity $\dot{x}_s$ is numerically integrated exploiting the trapezoidal method in order to compute the distance x_s travelled by the vehicle, using Eq. (27):

$$x_s = \int \dot{x}_s dt$$

(27)

SBG Ellipse A and Kistler accelerometer signals are filtered with a with a low-pass band filter (cut-off frequency equal to 100 Hz) to remove the signal noise. The time histories are first manually and roughly isolated. A refined synchronisation is carried out based on the second positive peak in the vertical acceleration of the front wheel. This peak corresponds to the end of the descendent phase of the front tyre with respect to the first bump.

4.2.2 Results

Figure 52 and Figure 53 present the z acceleration acquired by the four accelerometers and the angular velocity around the vehicle lateral axis during the tests driving Xiaomi Pro II and Aprilia ESR2 e-scooters at different velocities. Results reached at 5 km/h are not reported for sake of clarity in the plots. The signals are reported in function of the spatial coordinate x_s.

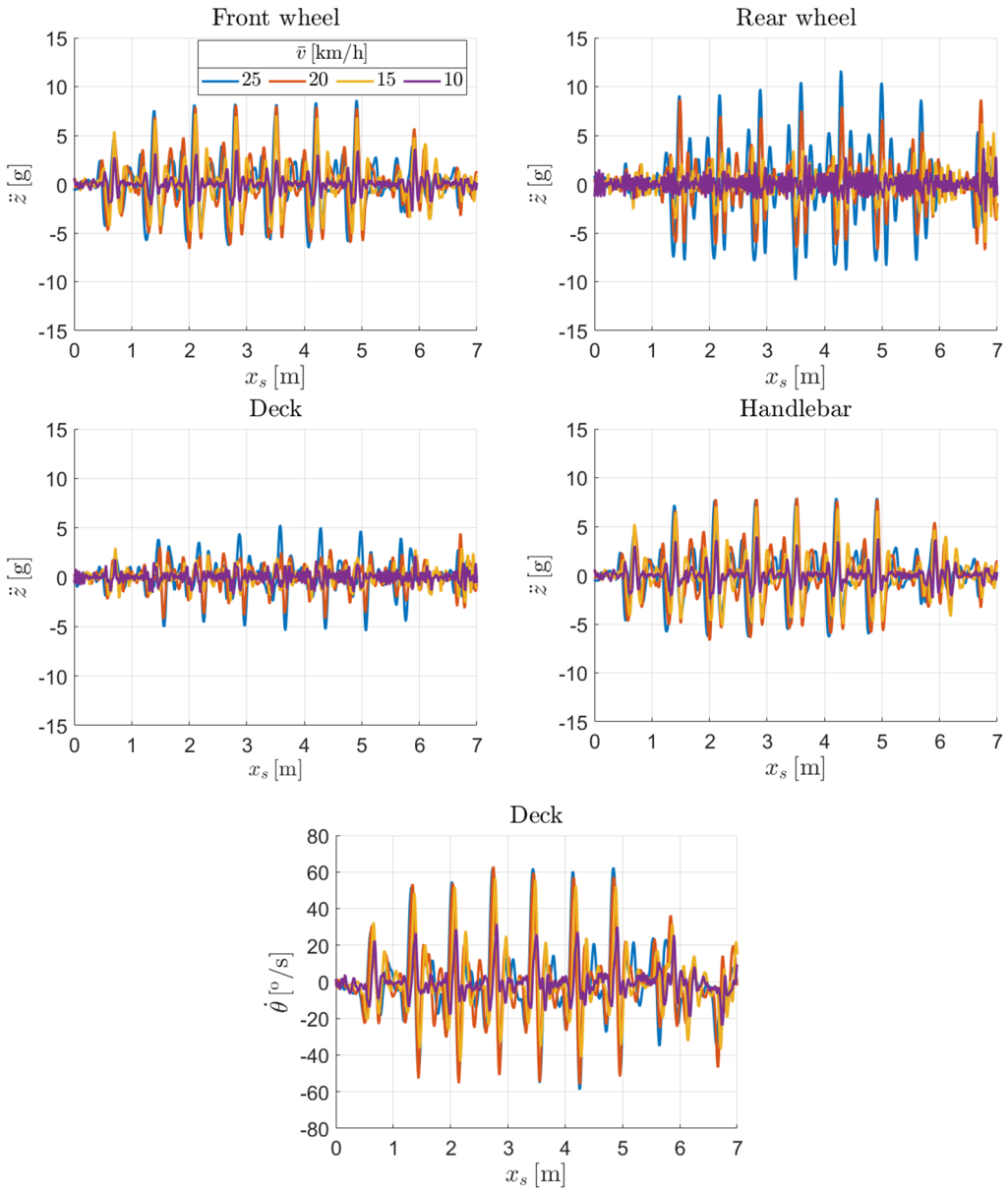

Figure 52 - Vertical accelerations and pitch rate of Xiaomi Pro II varying the velocity in the road with the bump series

Taking as reference the front wheel z acceleration, the signals at 15 km/h, 20 km/h and 25 km/h are very similar each other. The same speech can be extended also to the handlebar z acceleration. The largest difference both in terms of trend, minima and maxima are evident in correspondence of the rear wheel and the deck. Moreover, rear wheel and deck signals at 10 km/h seem to be noisy.

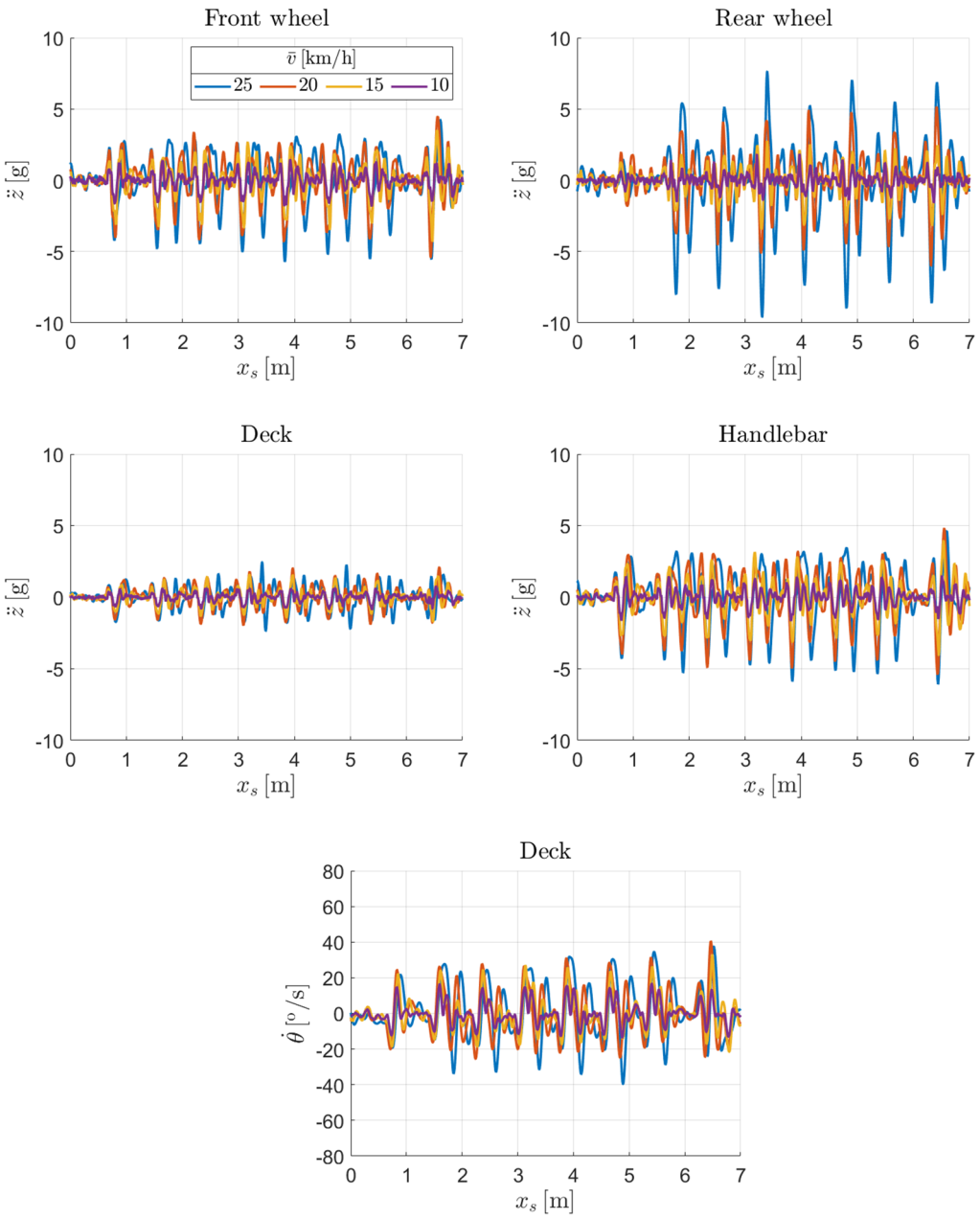

Figure 53 - Vertical accelerations and pitch rate of Aprilia ESR2 varying the velocity in the road with the bump series

Tests on Aprilia ESR2 show that the z acceleration in all the measuring area is influenced a lot by the vehicle velocity. Since the rider is always the same and even the inertial properties of the two e-scooters are very similar, the different behaviour can be reconducted to the differences between the vehicles, i.e., the wheelbase, the tyres (size and stiffness), the presence of the suspension systems.

Figure 54 and Figure 55 report the absolute maxima and minima of the z acceleration of each test detected by the four accelerometers. The results are reported in function of the average velocity of the test. All the tests carried out on the road with the bump series are considered in the following analysis. Figure 54 represents the comparison of the four measuring points within the same vehicle.

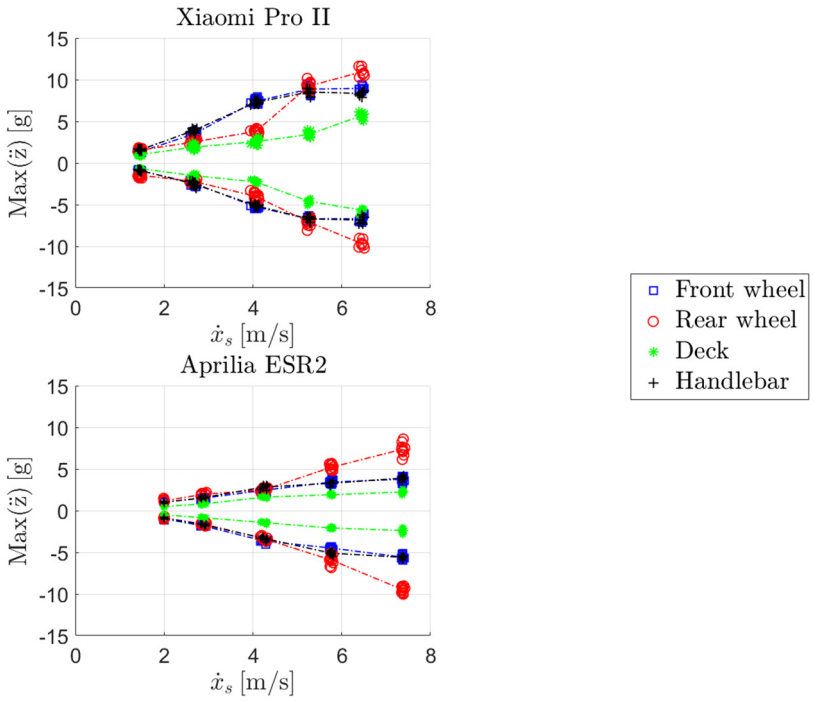

Figure 54 - Maxima and minima of the vertical accelerations of Xiaomi Pro II and Aprilia ESR2 in the road with the bump series

The considerations common to both e-scooters are reported below.

- Relevant level of repeatability in terms of maxima and minima is evident given the velocity.
- Maxima and minima are quite symmetric.
- Handlebar and front wheel maxima and minima are almost coincident.
- Deck is always the measuring area characterised by the smallest maxima and minima.

The third point is also studied exploiting the multibody model and presented in subparagraph 6.1.1. The difference between the two e-scooters occurs at the rear wheel trend of maxima and minima against the velocity. In Xiaomi Pro II, the rear wheel absolute values are lower than the front wheel absolute values at low

velocity and overcome them at about 18 km/h. In Aprilia ESR2, the rear wheel absolute values are comparable to the front wheel absolute values and start diverging over 15 km/h. This difference can be reconducted to the presence of the suspension system at the rear in the Aprilia ESR2 e-scooter. Figure 55 represents an inter-vehicle comparison considering each measuring area.

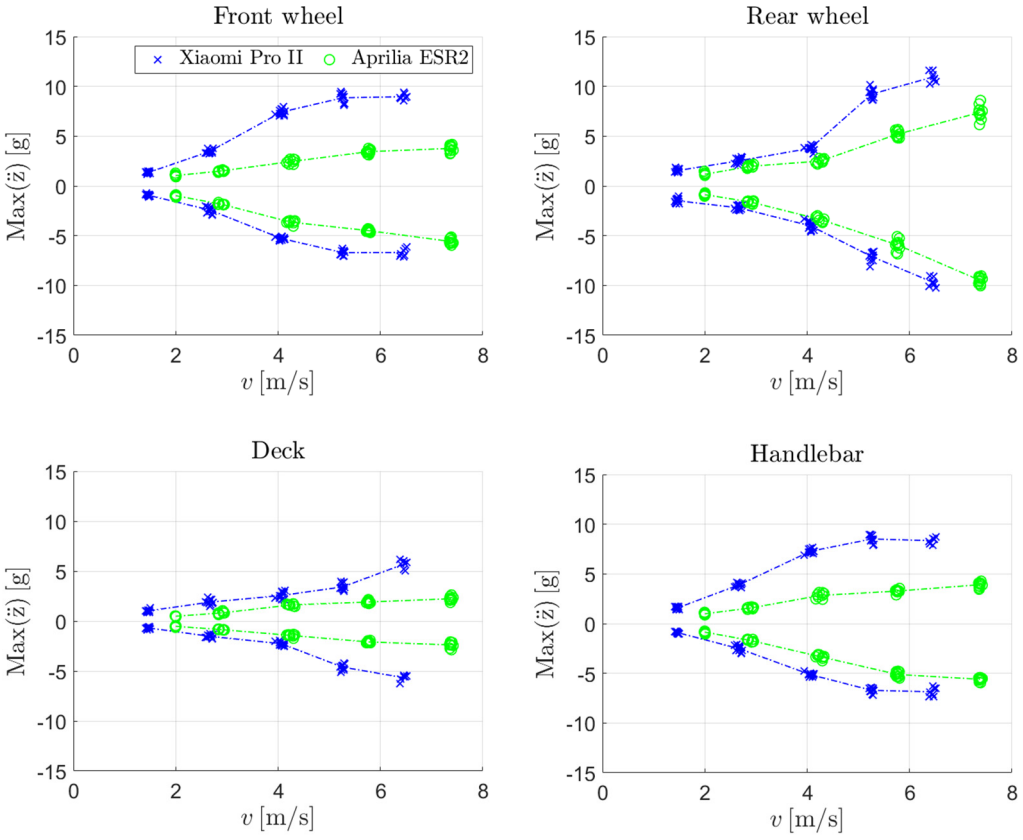

Figure 55 - Comparison between the e-scooters in terms of maxima and minima of the vertical accelerations in the road with the bump series

The effective velocity is different between the two e-scooter for the same target velocity. Since the author is confident in the measurements and in the data processing, the gap is attributed to an overestimation of the Xiaomi Pro II velocity displayed by the control unit onto the display and used by the rider as reference during the test. Apart from this negligible issue, it is evident that maxima and minima detected on-board of Xiaomi Pro II are always higher than the values detected on Aprilia ESR2. Two factors which determine the different dynamic behaviour are the tyre characteristics (see paragraph 2.3) and the presence of the suspension systems. The presented results do not involve acceleration components

along x and y axes since they are less significant than the z component for the four measuring areas.

4.3 Asphalted and pavé road tests

In this paragraph, the attention is shifted from lumped road irregularities to homogeneous surfaces: an experimental comfort comparison is described. The experimental comparison between the two e-scooters is conducted on two different road surfaces, asphalt and pavé, at different constant velocity.

Figure 56 - Asphalt and pavé road

ISO 2631-1 [62] and ISO 5349-1 [63] are used to assess vibrations transmitted by the vehicle respectively to rider's feet and hands. In sub-paragraph 3.3.1 the test procedure is described. In sub-paragraph 3.3.2 the data processing is explained. In sub-paragraph 3.3.3 the most interesting results are shown.

4.3.1 Test procedure

All the tests here described have been carried out by the reference rider. For more details see paragraph 2.4. The acquisitions are performed at constant velocity, from 5 to 25 km/h. Redundant tests are conducted in order to find statistically reasonable results. It is decided to perform the assessment on the same stretch of road in order to acquire homogeneous data. The duration of each acquisition varies according to the test velocity. It is considered statistically sufficient even for the shortest tests, corresponding to the highest velocity. The pavé road is almost 100 m long while the asphalted road is 330 m long. Figure 57

and Figure 58 represents the velocity during the tests achieved respectively on Xiaomi Pro II and Aprilia ESR2.

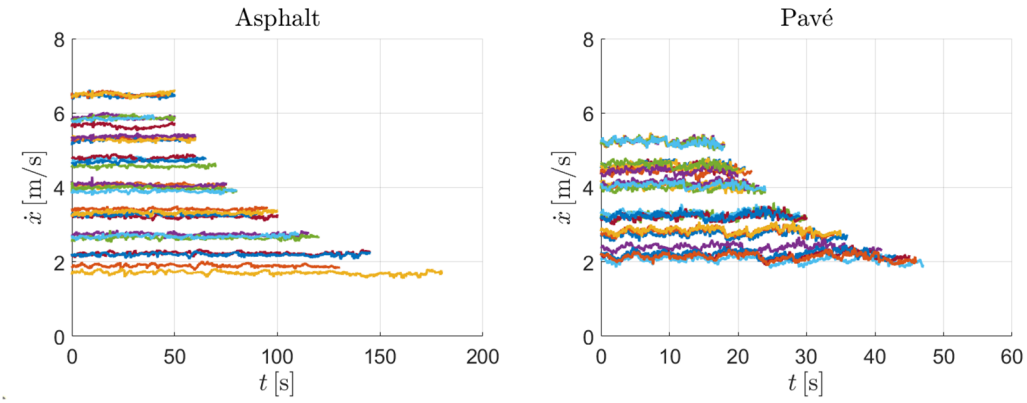

Figure 57 - Xiaomi Pro II velocity during asphalt and pavé road tests

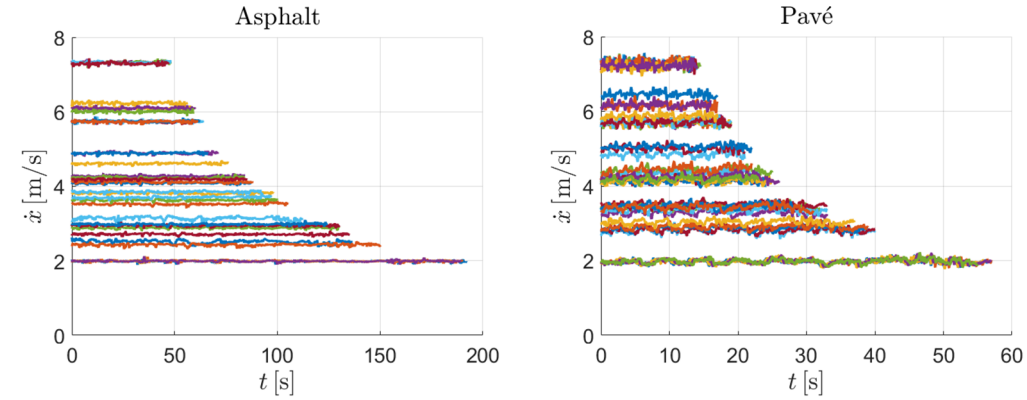

Figure 58 - Aprilia ESR2 velocity during asphalt and pavé road tests

On the asphalted road it is evident that the maximum velocity of Xiaomi Pro II is lower than the maximum velocity of Aprilia ESR2. With the Xiaomi Pro II e-scooter on the pavé surface, it is not possible to reach the maximum velocity due to the high vibration level, which compromises safety.

4.3.2 Data processing

ISO 2631-1 (whole-body vibrations) [62] and ISO 5349-1 (hand-transmitted vibrations) [63] constitute the reference standard for the comfort assessment as regards respectively whole body and hand-transmitted vibrations. The procedure defined by ISO 2631-1 and ISO 5349-1 is based on the frequency weightings of the experimental vibrations and the computation of the Root Mean Square (RMS). The final target of the analysis is computing for each experimental acquisition a

synthetic parameter a_v to be used as objectified benchmark between different testing conditions. In this study, the comfort index is used to highlight the different ride comfort perception on electric kick scooter by varying the velocity, the road surface and the vehicle. This methodology is commonly considered valid for crest factors (CREST) less than 9. The comfort frequency range is between $0.5 - 80$ Hz for the whole-body vibrations and $8 - 1000$ Hz for the hand-transmitted vibrations. As concern Standard dedicated to whole-body vibrations, the frequency weightings, which are nothing but acceleration gains function of the frequency, depend on several aspects:

- the purpose of the study (health, comfort, perception, motion sickness);
- the human body posture (standing, recumbent, seated);
- the human body segment (feet, pelvis, back);
- the direction of the vibration.

In this study the weightings for comfort assessment are used, the human body position is standing and the whole-body vibration is transmitted by the deck floor to the feet. On the other hand, the Standard dedicated to hand-transmitted vibrations prescribed a single set of weighting independently of the purpose of the study and the direction of the vibration. Table 29 reports the weightings to be used according to the vibration location and the vibration direction.

Table 29 - Frequency weightings in function of the vibration location and axis [62,63]

Location	**Axis**	**Weighting**
Deck	x, y	W_d
	z	W_k
Handlebar	x, y, z	W_h

Figure 59 shows the graphical representation of the frequency weightings reported in Table 29.

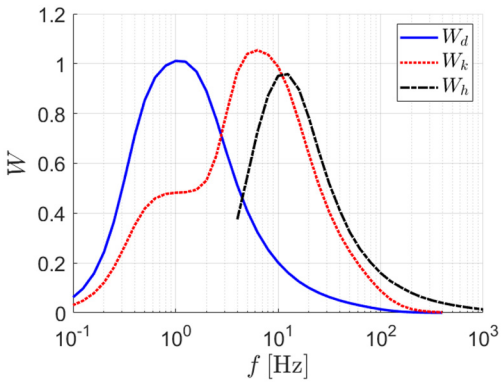

Figure 59 - Weightings in function of the frequency [62,63]

Frequency response of the accelerometers and the signal conditioning of the acquisition system are in agreement with the requirements of the Standards. The first step in the data processing is applying the abovementioned filters (W_k, W_d, W_h) to the components of acceleration ($\ddot{x}, \ddot{y}$, $\ddot{z}$) to obtain the filtered equivalent components ($a_{W,x}$, $a_{W,y}$, $a_{W,z}$) and the relative root mean squares ($\mathrm{RMS}(a_{W,x})$, $\mathrm{RMS}(a_{W,y})$, $\mathrm{RMS}(a_{W,z})$). To do so, three different methods are proposed in the following: they are explained with reference to the generic acceleration component a. The three methods show differences lower than 0.5%. The comfort index referring to a single vehicle-rider interface is computed combining $\mathrm{RMS}(a_{W,i})$ according to Eq. (28).

$$a_v = \sqrt{k_x^2 \left(\mathrm{RMS}(a_{W,x})\right)^2 + k_y^2 \left(\mathrm{RMS}(a_{W,y})\right)^2 + k_z^2 \left(\mathrm{RMS}(a_{W,z})\right)^2} \tag{28}$$

k_x, k_y and k_z are multiplying factors depending on the same parameters which impact on the choice of the frequency weightings. In agreement with the Standards, they are equal to 1 within this study. The abovementioned CREST factor, which represents a sort of relative maximum of the signal, is computed component by component.

$$\mathrm{CREST}(a_{W,i}) = \frac{\mathrm{Max}(|a_{W,i}(t)|)}{\mathrm{RMS}(a_{W,i})} \qquad i = x, y, z \tag{29}$$

It is important to underline that $\mathrm{CREST}(a_{W,i})$ must be identified in the same time interval T used for the computation of $\mathrm{RMS}(a_{W,i})$. If the crest factor is equal or lower than 9, the proposed assessment is appropriate.

Method 1 - Filtering in time domain by a digital filter

Before applying the weightings, the whole-body vibrations must be filtered with a high-pass band filter with cut-off frequency of 0.4 Hz and with a low-pass band filter with cut-off frequency of 100 Hz. The cut-off frequencies of the same filters for the hand-transmitted vibration are 6.3 Hz and 1258.9 Hz respectively. The frequency weightings shown in Figure 59 are used to develop the corresponding finite impulse response (FIR) digital filters (arbitrary magnitude response). The square roots of the weightings $W(f)$ are used as frequency amplitudes. The parameters in Table 30 are also required in the design of the filter.

Table 30 - Digital filter parameters

Filter order	3000
Sampling rate f_s [Hz]	3200

The sampling rate is referred to the signal to be processed. The input signal a is processed in forward and in backward direction. Consequently, the filter amplitudes are the squares of the original filter amplitudes, the filter order is twice the original filter order, and zero phase distortion is ensured in the filtered signal a_W. Root mean square is computed in time domain according to Eq. (30),

$$\mathrm{RMS}(a_W) = \sqrt{\frac{1}{T}\int_0^T a_W^2(t)dt} \tag{30}$$

where T is the time interval in which the RMS is computed. Since the signals are discrete, Eq. (30) turns into Eq. (31),

$$\mathrm{RMS}(a_W) = \sqrt{\frac{1}{N}\sum_{\kappa=1}^{N} a_{W,\kappa}^2(t)}$$

(31)

where N represents the number of samples. The proposed method is useful since it also allows the computation of CREST, according to Eq. (29).

Method 2 - Filtering in time domain by transfer function

The second method to filter signal a is also carried out in time domain. It is based on the creation of transfer functions TF equivalent to the digital filters. Signal a is used as input for TF while the filtered signal a_W is the output. The parameters of the transfer functions and their formulations are reported in ISO 2631-1 [62] and ISO 5349-1 [63]. Table 31 reports the parameters for the computation of the transfer function related to W_k and W_d.

Table 31 - Parameters of the transfer functions related to the frequency weightings of ISO 2631-1

	Band-limiting		**Acceleration-velocity transition**			**Upward step**			
	f_1	f_2	f_3	f_4	Q_4	f_5	Q_5	f_6	Q_6
W_k	0.4	100	12.5	12.5	0.63	2.37	0.91	3.35	0.91
W_d	0.4	100	2.0	2.0	0.63	∞	0	∞	0

The frequencies must be preliminarily turned into angular frequencies.

$$\omega = 2\pi f$$

(32)

The transfer function $H_{2631}(p)$ prescribed by ISO 2631-1 is reported in Sys. (33),

$$\begin{cases} H_{2631}(p) = H_h(p)H_l(p)H_t(p)H_s(p) \\ H_h(p) = \dfrac{1}{1 + \dfrac{\sqrt{2}\omega_1}{p} + \left(\dfrac{\omega_1}{p}\right)^2} \\ H_l(p) = \dfrac{1}{1 + \dfrac{\sqrt{2}p}{\omega_2} + \left(\dfrac{p}{\omega_2}\right)^2} \\ H_t(p) = \dfrac{1 + \dfrac{p}{\omega_3}}{1 + \dfrac{p}{\omega_4 Q_4} + \left(\dfrac{p}{\omega_4}\right)^2} \\ H_s(p) = \dfrac{1 + \dfrac{p}{Q_5\omega_5} + \left(\dfrac{p}{\omega_5}\right)^2}{1 + \dfrac{p}{Q_6\omega_6} + \left(\dfrac{p}{\omega_6}\right)^2}\left(\dfrac{\omega_5}{\omega_6}\right)^2 \end{cases} \tag{33}$$

where p represents the variable of the Laplace transform. H_h and H_l are related to the high and low pass-band filter. The product of the transfer function H_t and H_s is the real frequency-weighting filter. Table 32 reports the parameters for the computation of the transfer function related to W_h.

Table 32 - Parameters of the transfer functions related to the frequency weighting of ISO 5349-1

	Band-limiting			**Frequency weightings**			
	f_1	f_2	Q_1	f_3	f_4	Q_2	K
W_h	6.31	1258.9	0.71	15.915	15.915	0.64	1

The transfer function $H_{5349}(p)$ prescribed by ISO 5349-1 is reported in Sys. (34),

$$\begin{cases} H_{5349}(p) = H_b(p)H_w(p) \\ H_b(p) = \dfrac{p^2\omega_2^2}{(p^2 + \frac{\omega_1 p}{Q_1} + w_1^2)(p^2 + \frac{\omega_2 p}{Q_1} + \omega_2^2)} \\ H_w(p) = \dfrac{(p + \omega_4)Kf_4}{\left(p^2 + \frac{\omega_4 p}{Q_2} + \omega_4^2\right)f_3} \end{cases} \tag{34}$$

where H_b refers to the pass-band filter while H_w to the frequency-weighting filter. After computing a_W, Eqs (31) and (29) are applied. Even this method is useful since it allows the computation of CREST, according to Eq. (29).

Method 3 - Filtering in frequency domain

The third method is the only one applied in frequency domain. The first step is the transformation from time domain to frequency domain applying the Fast Fourier Transform (FFT) to the original signal.

$$a(f) = \text{FFT}(a(t)) \tag{35}$$

The following parameters are adopted in the FFT:

- the frequency resolution Δf is the highest possible (equal to $1/T$);
- the overlap is set equal to 0%;
- no windowing is set.

High-pass band and low-pass band filters are just applied bringing to zero the corresponding amplitude of $a(f)$ out of the frequency band of interest. The frequency weighting is obtained multiplying band by band the amplitude of $a(f)$ by $W(f)$. The root mean square in frequency domain is computed according to Eq. (36),

$$\mathrm{RMS}(a_W) = \sqrt{\frac{1}{M}\sum_{\chi=1}^{N}\left(\frac{a_{W,\chi}(f)}{2}\right)^2}\sqrt{\frac{f_s}{\Delta f}} \tag{36}$$

where:

- M is the length of the signal in frequency domain;
- f_s [Hz] is the sampling frequency of the signal;
- Δf [Hz] is the frequency resolution of the signal after FFT.

4.3.3 Results

Acceptable level of vibrations in the comfort assessment are not univocally defined: they strictly depend on the applications. Table 33 indicates the reference values in public transport as for the whole-body vibrations.

Table 33 - Reference on comfort reaction in public transport (ISO 2631-1)

Band $[\mathbf{m/s^2}]$	**Reaction**
< 0.315	Not uncomfortable
$0.315 - 0.63$	A little uncomfortable
$0.5 - 1$	Fairly uncomfortable
$0.8 - 1.6$	Uncomfortable
$1.25 - 2.5$	Very uncomfortable
> 2	Extremely uncomfortable

Figure 60 represents the comfort index evaluated on the deck versus the velocity, for both electric scooters on the two surfaces. The bands in Table 33 are also reported in the graph.

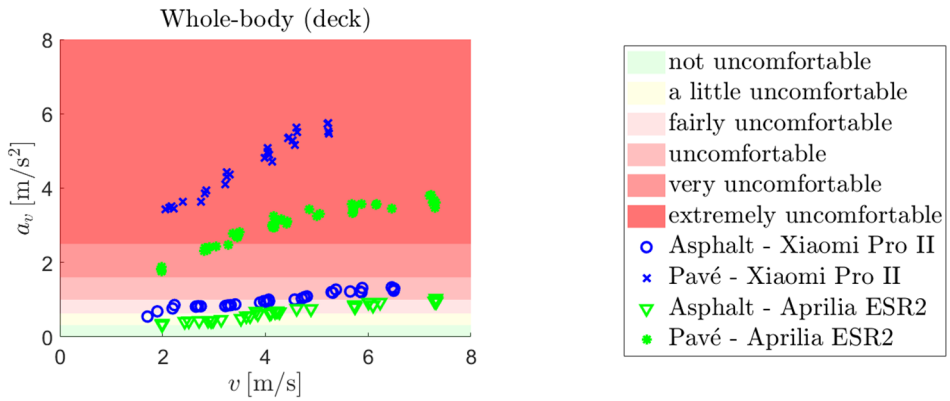

Figure 60 - Comfort index evaluated on the deck

The following considerations can be drawn.

- a_v always increases with the vehicle speed.
- Pavé road emphasizes the difference between the vehicles.
- The increasing slope of a_v with respect to the vehicle velocity is higher on pavé than asphalt.
- a_v related to Aprilia ESR2 seems to reach an asymptotic value for high velocity, while a_v related to Xiaomi Pro II seems to continue increasing.

Figure 61 represents the comfort index evaluated on the handlebar versus the velocity, for both electric scooters on the two surfaces.

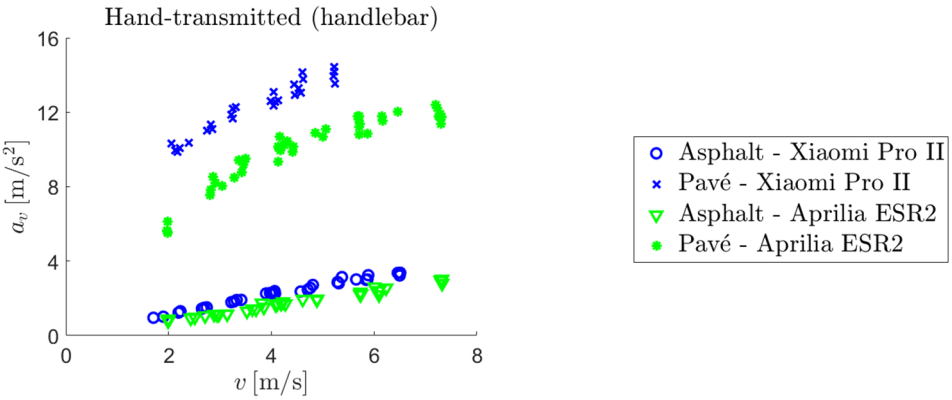

Figure 61 - Comfort index evaluated on the handlebar

The same considerations discussed for the whole-body vibrations can be extended to the hand-transmitted ones. The magnitudes are generally higher compared to the whole-body ones.

No dependency of CRESTs on velocity is detected for both vehicles and on both surfaces. For this reason, CRESTs are averaged components by components. Figure 62 and Figure 63 respectively represent the CRESTs evaluated on the deck and on the handlebar along the three axes.

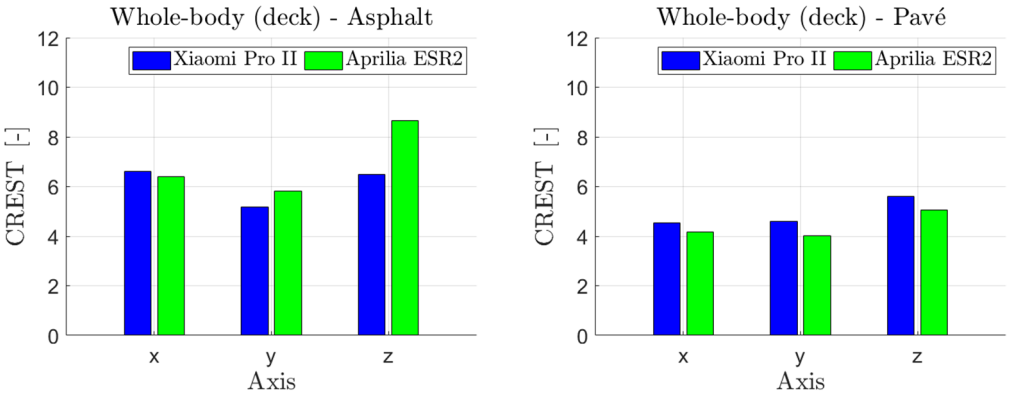

Figure 62 - Crest factors evaluated on the deck

Regarding Figure 62, the following aspects can be highlighted:

- CREST is always much smaller than the critical threshold of 9, except for the z value of Aprilia ESR2 on asphalt;
- CRESTs along the three directions are comparable for both vehicles on both surfaces;
- CRESTs related to Xiaomi Pro II on pavé are always higher than CRESTs related to Aprilia ESR2.

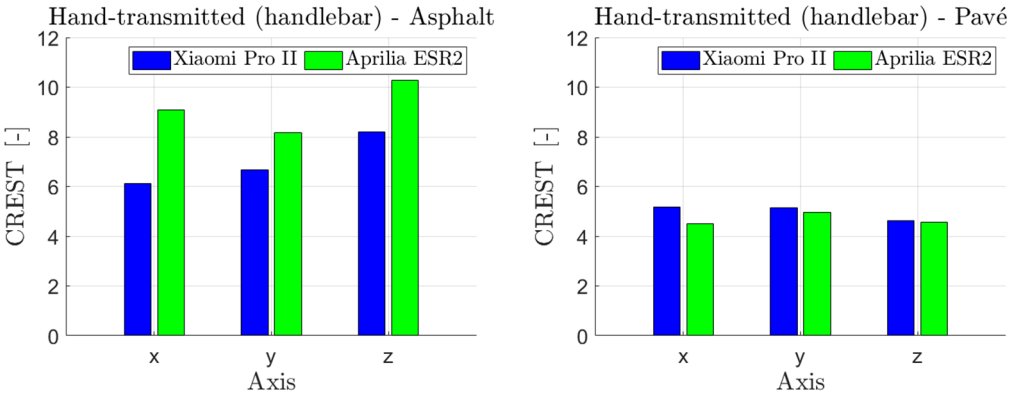

Figure 63 - Crest factor evaluated on the handlebar

Regarding Figure 63, the following aspects can be highlighted;

- CREST is slightly higher than the critical value along x and z axes in Aprilia ESR2 on asphalt;
- CRESTs of Aprilia ESR2 are higher on asphalt and lower on pavé with respect to the CRESTs of Xiaomi Pro II.

Generally speaking, whole-body CRESTs are lower than hand-transmitted CRESTs. In conclusion, CREST is strongly influenced by the denominator in Eq. (29). Thus, it is strictly connected to the measuring area, the road surface and the capacity of the vehicle to filter vibrations.

Chapter 5

Human body motion

This chapter presents the experimental analyses aiming at evaluating the rider kinematics in longitudinal manoeuvres and driving on the bump series already discussed in paragraph 4.2.

Sensor setup and data processing are discussed in paragraph 5.1. The main results related to the standing start on Xiaomi Pro II e-scooter, are reported in paragraph 5.2. For the sake of brevity, the results related to the braking manoeuvre on Xiaomi Pro II will be shown in the experimental-numerical comparison discussed in paragraph 6.2. Paragraph 5.3 deals with the tests conducted on the road with bumps at constant velocity, driving Xiaomi Pro II. Finally, a statistical assessment carried out on a sample of fourteen people to characterise the vibration transmissibility from vehicle to driver is presented in paragraph 5.4. This final work is carried out using Aprilia ESR2 e-scooter.

5.1 Sensor setup and data processing

The sensor setup used for the experimental study of human body motion driving Xiaomi Pro II and Aprilia ESR2 electric kick scooter is reported in Figure 64.

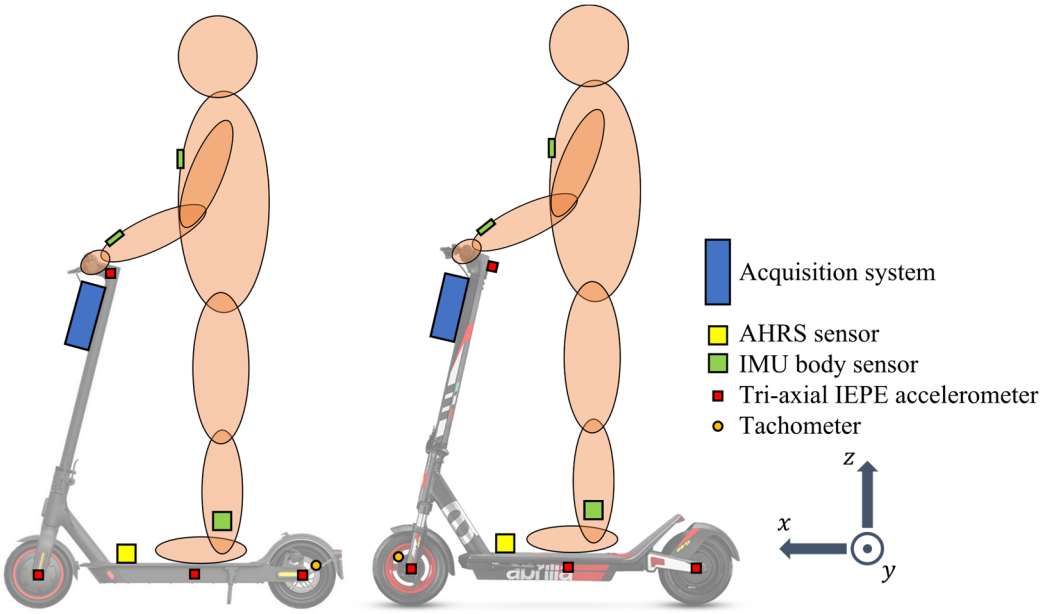

Figure 64 - Experimental setup for human body motion analyses

The experimental setup is constituted by:

- Siemens SCADAS XS acquisition system;
- SBG Ellipse A AHRS inertial unit;
- four Kistler IEPE tri-axial accelerometers;
- Gebildet LJ12A3-4-Z proximity sensor;
- five wearable Opal APDM inertial units.

The acquisition system, the AHRS sensor, the tri-axial accelerometers and the tachometer have been already discussed in paragraph 4.1. Even in this case the acquisitions are manually started and stopped (Free-run mode) adopting the SCADAS standalone mode. The inertial system Opal APDM consists of five wireless magneto-inertial measurement units (MIMUs) containing a tri-axial accelerometer, a tri-axial gyroscope and a tri-axial magnetometer. Inertial sensors are fixed on rider's chest, left and right forearms, left and right shanks through bands supplied in APDM kit. Each unit is positioned paying attention to the alignment of its x axis with the longitudinal axis of the corresponding human body segment. The communication between the inertial units and the PC is guaranteed via Bluetooth. Data are acquired through the proprietary software Motion Studio with a sampling frequency of 200 Hz. The synchronization between Siemens SCADAS XS and the Opal APDM system is ensured following the procedure here reported. Each test begins with the vehicle completely stopped and an analogue port of the Siemens SCADAS XS connected to the Opal docking

station (Figure 112). The acquisition is launched on Siemens SCADAS XS; then, Opal system is launched: Opal units starts measuring and the docking station parallelly sends an analogue trigger to Siemens SCADAS XS. At this point, the two systems are physically disconnected, and the rider begins the test. Figure 65 represents the synchronisation of Siemens SCADAS XS and Opal APDM system. A conventional voltage equal to 0.5 V is used for zeroing the Siemens SCADAS XS signals.

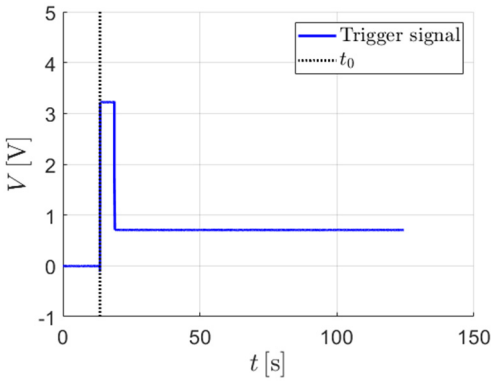

Figure 65 - Synchronization of the two acquisition systems

As concern the common data processing, the angular velocity of the rear wheel, ω_r, is filtered with a low-pass band filter (cut-off frequency equal to 4 Hz) and used to estimate the vehicle velocity $\dot{x}_s$ by Eq. (26). Gravitational field is removed from the accelerations acquired by Opal units following the procedure here presented. Vector $\boldsymbol{g}_G$ represents the magnetic field vector in the global reference system:

$$\boldsymbol{g}_G = [0 \quad 0 \quad 9.81]^T \tag{37}$$

while $\ddot{\boldsymbol{p}}_i$ represents the vector containing the three components of acceleration of the $_i$ Opal unit:

$$\ddot{\boldsymbol{p}}_i = [\ddot{x}_i \quad \ddot{y}_i \quad \ddot{z}_i]^T \tag{38}$$

Rotation matrix $\boldsymbol{A}_i$, corresponding to the $_i$ sensor, represents the orientation of the sensor in the global reference system. It is computed at each time step starting from Opal unit quaternions, provided by the sensor as a measurement.

Gravitational field $\boldsymbol{g}_G$ is reported in the reference frame of the Opal unit, $\boldsymbol{g}_i$, according to Eq. (39):

$$\boldsymbol{g}_i = \boldsymbol{A}_i \boldsymbol{g}_G \tag{39}$$

The gravitational field in the sensor reference frame $\boldsymbol{g}_i$ is subtracted from the acquired acceleration $\ddot{\boldsymbol{p}}_i$ according to Eq. (40):

$$\ddot{\boldsymbol{p}}_{i,0} = \ddot{\boldsymbol{p}}_i - \boldsymbol{g}_i \tag{40}$$

Finally, accelerations and angular velocities signals coming from the AHRS inertial unit, the four tri-axial accelerometers and the five Opal units are aligned to the vehicle reference axes. For more details on the acquisition system and the sensors used during the experimental campaign, refer to Appendix A.

5.2 Standing start and heavy braking manoeuvre

In this paragraph the standing start manoeuvre performed by the reference rider (see paragraph 2.4) monitoring the kinematics of the main body segments of the rider is discussed. Xiaomi Pro II e-scooter is used during this experimental campaign.

5.2.1 Test procedure

The test starts with the rider at the left of the e-scooter. The right foot is placed on the e-scooter deck while the left foot is on the ground. The left foot is used to kick the ground in order to accelerate the vehicle and overcome the motor velocity threshold. Finally, the left foot is brought onto the deck and the accelerator is simultaneously pushed. After reaching the maximum velocity for several seconds, the braking lever is completely pushed till the vehicle is completely stopped. Thus, a standing start manoeuvre and a heavy braking manoeuvre are recorded in a single acquisition. The test is repeated three times to verify repeatability.

5.2.2 Data processing

Data processing is carried out in Matlab R2022a. Since the several signals are synchronously acquired but characterised by different sampling frequencies, the first step of the post-processing consists of resampling the signals (frequency equal to 2000 Hz) in order to work on a common time base. A low-pass band filter (cut-off frequency equal to 8 Hz) is applied to remove the noise from the e-scooter longitudinal acceleration $\ddot{x}_s$. Acceleration and angular velocity components of the Opal units are filtered using a low-pass band filter with a cut-off frequency equal to 6 Hz to remove the noise without altering the original signal. The time interval corresponding to the manoeuvre of interest is isolated and presented in sub-paragraph 4.2.3.

5.2.3 Results

Figure 66 represents the longitudinal acceleration (left panel) and the velocity (right panel) during the manoeuvre.

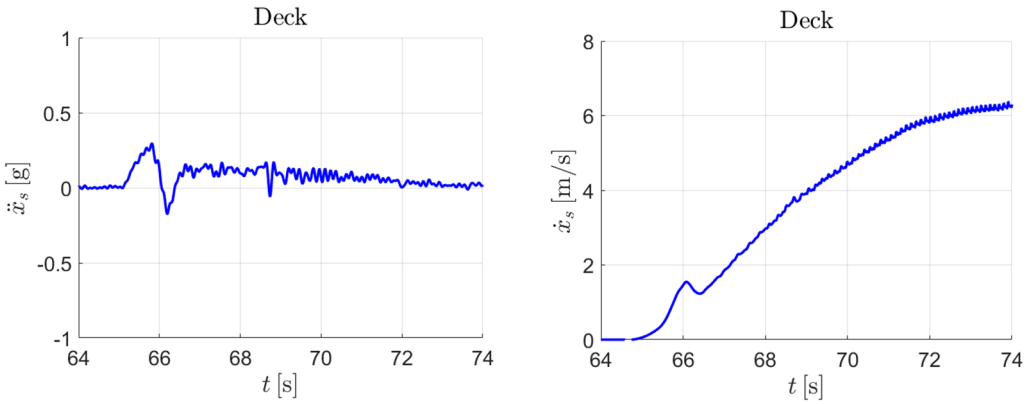

Figure 66 - E-scooter acceleration (left) and velocity (right) in the standing start manoeuvre

Experimental results are similar and coherent with the data presented in sub-paragraph 2.2.1. A comparison between the vehicle velocity estimated from the GNSS signal (paragraph 2.2) and the estimation here proposed from the angular velocity of the rear wheel is presented in Appendix B. Figure 67 represents the angular velocities, $\dot{\theta}$, around the y axis of the rider's chest, left and right forearms, left and right shanks.

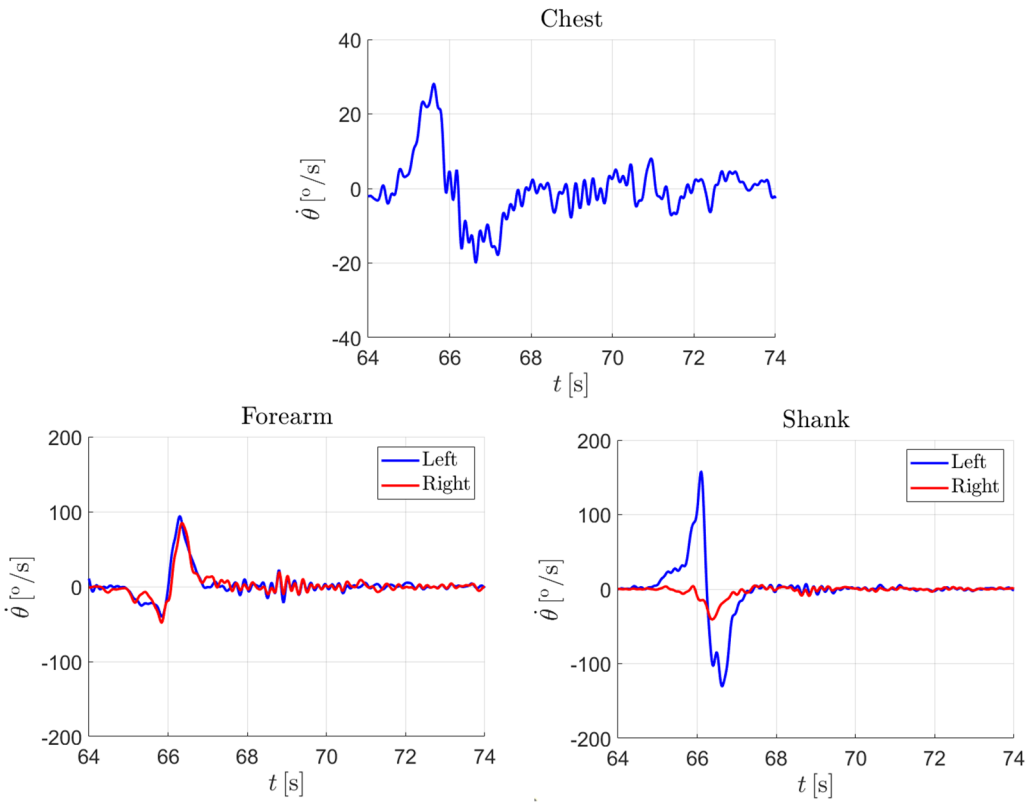

Figure 67 - Angular velocity around lateral axis of different body segments (chest, forearms, shanks) during the acceleration manoeuvre

As evidenced by Figure 67, the time interval in which the rider plays an active role in the manoeuvre (refer to Figure 32), is mainly characterised by two phases. The upper body is first bent forward ($\dot{\theta} > 0$). In the first phase the forearms are rotated due to the elbow flexion ($\dot{\theta} < 0$). In the second phase, the upper body is brought again in the normal upright position ($\dot{\theta} < 0$). Left and right forearms are characterised by a similar trend despite the vehicle standing start manoeuvre is asymmetric. The two different phases are also visible on the shank plot. The right shank which corresponds to leg used as a stand on the e-scooter deck is affected only by the rider positioning. On the contrary, the leg used to kick on the ground emphasises both the gestures. The other components of acceleration and angular velocity belonging to the five human body segments are not here reported since their trend is not significant during the manoeuvre. The results related to the heavy braking manoeuvre are reported in paragraph 6.2 together with the experimental-numerical comparison.

5.3 Bump road tests

In this paragraph the tests performed by the reference rider (see paragraph 2.4) aiming at studying the human body response driving on bumps are reported. Xiaomi Pro II e-scooter is used during this experimental campaign.

5.3.1 Test procedure

The test consists of driving at constant velocity the e-scooter on a bike path characterised by the presence of seven bumps. For more details on the bump-road, refer to paragraph 3.2. The velocity is kept constant thanks to the assistance of the cruise control. Three different velocities are tested, i.e., 15 km/h, 20 km/h and 25 km/h. The test is repeated three times for each velocity to verify the repeatability.

5.3.2 Data processing

Data processing is carried out in Matlab R2022a. Even in the post-processing of this experimental data, the first step of the consists of resampling the signals and adopting a common time base (frequency equal to 2000 Hz). The vehicle travel x_s is computed by the cumulative trapezoidal integration of $\dot{x}_s$ by Eq. (27). Acceleration and angular velocity components of the Opal units are filtered using a low-pass band filter with a cut-off frequency equal to 100 Hz to remove the noise without altering the original signal.

5.3.3 Results

In the following, the focus is on the vertical component of the acceleration (left panels) and the angular velocity around vehicle y axis (right panels) of the body segments. The magnitudes are plotted versus the spatial coordinate x_s. Since no remarkable differences can be qualitatively appreciated between the signals acquired on left and right limbs, only the signals of the left side of the rider are reported. Figure 68 refers to the left forearm, Figure 69 refers to the left shank and Figure 70 refers to the chest. The vertical dotted black line is drawn at the first positive peak of the vertical acceleration of the front wheel, corresponding to the climbing of the first bump. It is used as trigger for the synchronisation of the presented results.

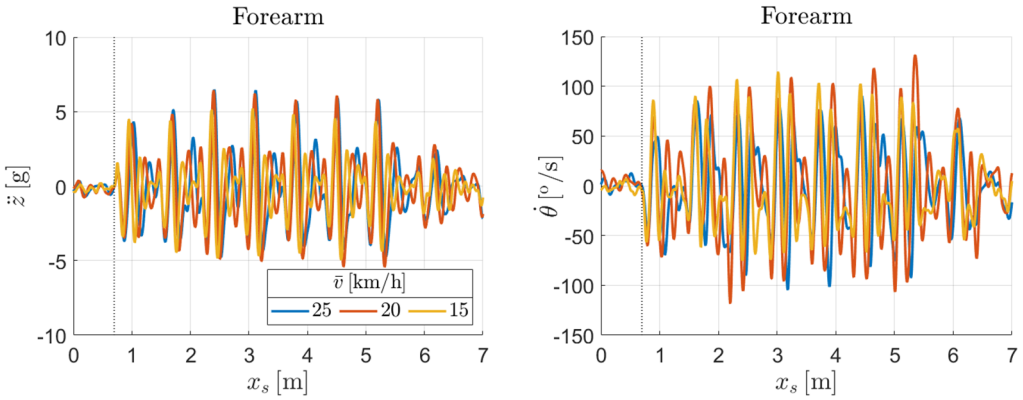

Figure 68 - Vertical acceleration (left) and angular velocity around lateral axis (right) of the left forearm varying the velocity

As evidenced by Figure 68, the forearm motion seems to be not influenced by vehicle velocity. Both maxima and minima as well the overall trends are fairly similar driving at the three velocities. The forearm response results to be periodic as the road input.

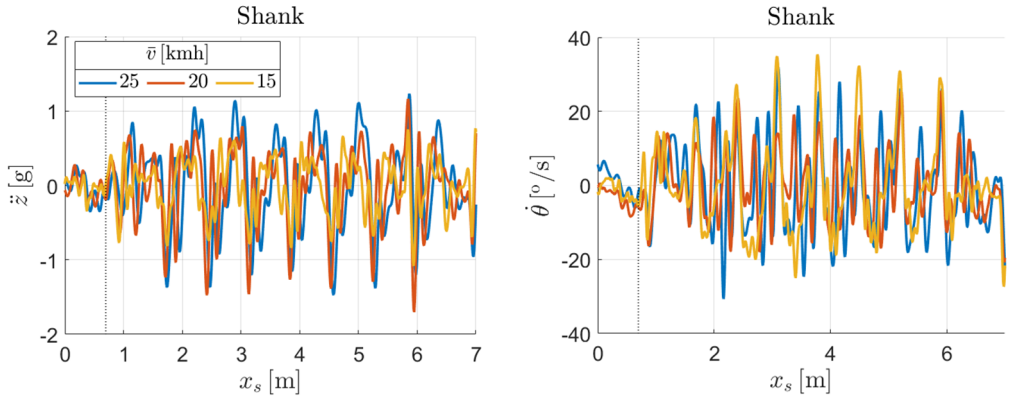

Figure 69 - Vertical acceleration (left) and angular velocity around lateral axis (right) of the left shank varying the velocity

Vertical acceleration detected at the shank, reported in Figure 69, is similar in the tests at 20 and 25 km/h, while maxima and minima are reduced at 15 km/h. Similarities can be highlighted even for the angular velocity at 20 and 25 km/h. In relation to 15 km/h, some maxima are higher than the corresponding one at 20 and 25 km/h. As a general consideration, the absolute maxima of the vertical accelerations detected at the forearm are almost three times the absolute maxima of the vertical accelerations detected at the shank. The forearm is indeed closer to the handlebar where vibrations are experimentally higher than the deck. On the contrary, the deck vibrations influence more the shank measurements.

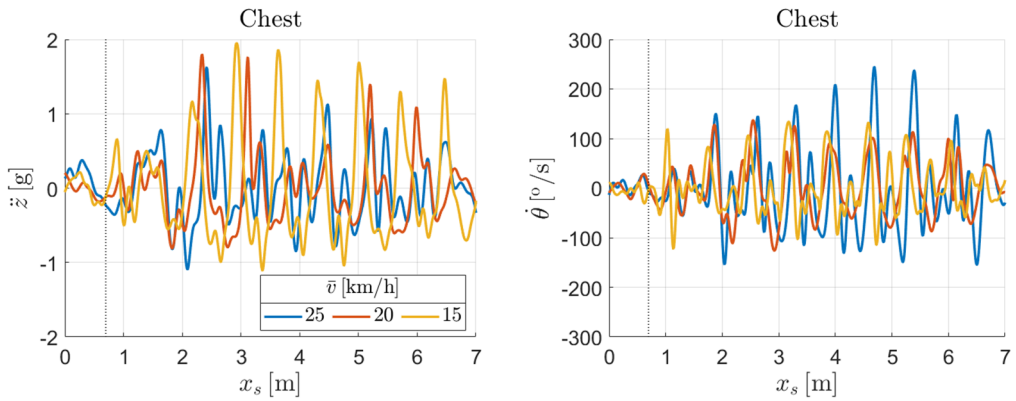

Figure 70 - Vertical acceleration (left) and angular velocity around lateral axis (right) of the chest varying the velocity

The largest differences can be detected on the chest varying the velocity, both in terms of vertical acceleration and angular velocity. The chest motion is indeed influenced by the vibrations coming from the handlebar through the upper limbs and the vibrations coming from the deck through the lower limbs. Both vertical acceleration and angular velocity trends are not periodic and vary during the test, highlighting a possible effort of the rider to adapt to the input and being less affected by vibrations due to the road profile. In contrast to forearm and shank magnitudes, chest measurements are less repeatable comparing results at the same velocity. This effect does not degrade the repeatability of the vibration measurements carried out on the e-scooter, suggesting a sort of uncoupling phenomenon between the vehicle and the rider systems. As it will be remarked in subparagraph 6.3.2 which is dedicated to the comparison between the experimental signals and the numerical results of the multibody simulation, the abovementioned uncoupling effect occurs at the high velocities. At low velocities, the rider tends to be more rigid and at the same time rigidly connected to the vehicle. On the contrary, the dynamic influence of the human body inertia tends to decrease at higher velocities. This aspect justifies the fact that at 15 km/h the chest vertical acceleration seems to be characterised by higher amplitudes and higher regularity.

5.4 Statistical analysis on the bump road

In this paragraph a statistical assessment with the goal of evaluating the vibration transmissibility from vehicle to driver is presented. Aprilia ESR2 e-scooter is used during this experimental campaign.

5.4.1 Participants

Fourteen healthy young subjects (seven males and seven females) represent the statistical population in the experiment. Four inclusion criteria are considered in order to analyse a homogeneous group of people:

- age between 20 and 35 years;
- no neurological disorders and musculoskeletal diseases;
- equal level of expertise driving e-scooters.

The choice of investigating a population characterised by a low level of expertise is driven by the easiness of recruiting participants and the possibility to analyse the behaviour of first-time riders. Data related to age, gender, mass, height and BMI are reported for each participant in Table 34.

Table 34 - Participants data

Subject	Age [y]	Gender	Mass [kg]	Height [m]	BMI [kg/m^2]
1	26	M	96	1.80	29.6
2	25	F	61	1.73	20.4
3	26	F	58	1.64	21.6
4	24	F	50	1.63	18.8
5	28	M	80	1.70	27.7
6	31	F	60	1.67	21.5
7	28	F	54	1.58	21.6
8	28	F	60	1.77	19.2
9	32	M	83	1.80	25.5
10	27	M	63	1.73	21.0
11	31	M	95	1.85	27.6
12	29	M	57	1.73	19.0
13	25	M	65	1.78	20.5
14	29	F	55	1.65	20.2
Mean/Std	27.8/2.5		66.9/15.1	1.7/0.1	22.5/3.6

Table 35 reports the dominant hand, the dominant foot, the foot used for kicking in the standing start and the foot position on the deck for each participant.

Table 35 - Dominant arm and riding foot position of the participants

Subject	Dominant hand	Dominant foot	Kick foot	Foot position
1	R/L	R	R	Parallel
2	L	R	L	Tandem
3	R	R	R	Tandem
4	R	R	R	Tandem
5	R	R	L	Tandem
6	L	L	L	Tandem
7	R	R	R	Tandem
8	R	R	L	Tandem
9	R	R	L	Tandem
10	R	R	L	Tandem
11	L	L	L	Parallel
12	R	R	L	Parallel
13	R	R	R	Tandem
14	R	R	R	Parallel

R: Right, L: Left

Parallel foot position ensures a perfect symmetry of the rider with respect to the middle plane of the vehicle (xz). Tandem position consists of placing one foot forward the other one on the deck floor. The forward foot is generally aligned with the longitudinal axis of the vehicle (x) while the backward foot can be rotated of a certain angle with respect to the xz plane of the vehicle. The riders which prefer the foot tandem position use the backward foot for the initial kick. Among the participants, three subjects (21.5%) are left-handed while only one subject is ambidextrous. Apart from two subjects, the whole population has the dominant hand aligned with the dominant foot. Eight subjects (57%) prefer to use the dominant foot for the kick. Tandem foot position is preferred by ten subjects (71.5%) with respect to parallel foot position (28.5%). All the subjects who adopted the tandem foot position place the kick foot behind the other one.

5.4.2 Test procedure

Each participants conducts twelve tests driving at constant velocity the e-scooter on a bike path characterised by the presence of seven bumps.: six tests are carried out at 5 km/h and six tests at 25 km/h. These velocities respectively correspond to the maximum admitted velocity in pedestrian areas and the maximum admitted velocity on bike paths and urban roads. For more details on the bump road, refer to paragraph 3.2. Even if no participant has riding experience, the vehicle velocity has been kept constant thanks to the assistance of the cruise control and the motor modalities which limit the maximum vehicle velocity. The velocity in the bump stretch is verified after each test exploiting the tachometer measure.

5.4.2 Data processing

The procedure described in this sub-paragraph is applied to each acquisition. Data processing is carried out in Matlab R2022a. The vertical acceleration detected at the front wheel is used as trigger signal for the identification of the time intervals to be used in the assessment. Firstly, the bump series is roughly identified and isolated in the whole-time history. Then, the front wheel vertical acceleration is filtered with a low-pass band filter with a cut-off frequency depending on the vehicle velocity: this magnitude is used for the refined identification of the bump series. The first bump encountered is conventionally associated to the first relevant positive peak. The parameters used in the data processing are reported in Table 36.

Table 36 - Cut-off frequency and parameter for the peak identification

	v [km/h]	
Parameter	5	25
$f_{cut-off}$ [Hz]	40	120
Minimum peak height [g]	0.34	2.40

The raw and filtered vertical acceleration and peak identification referring to the first tests at 5 and 25 km/h of the first participant are reported in Figure 71 as examples.

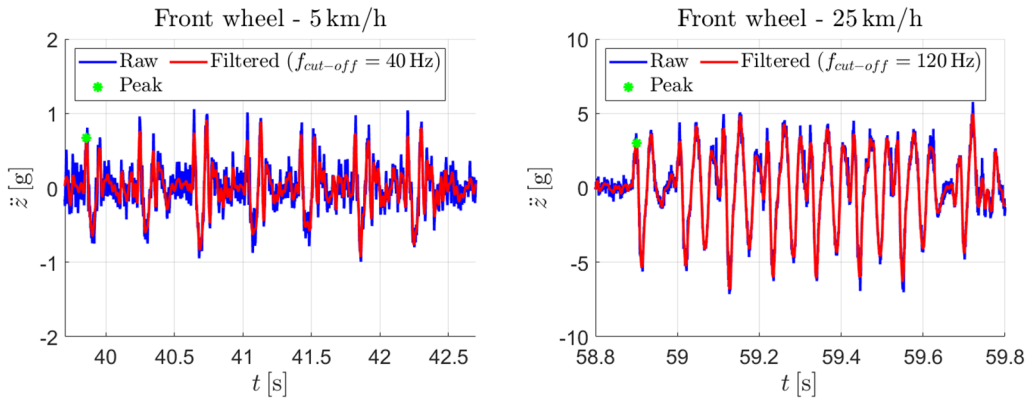

Figure 71 - Raw and filtered vertical acceleration and peak identification

The statistical analysis is carried out on the norm n of the acceleration acquired at the deck and the handlebar, which constitute the vehicle-human body interfaces, and at human body segments, i.e., the forearms, the shanks and the chest. The acceleration norm n_i corresponding to the i sensor is computed according to Eq. (41),

$$n_i = \sqrt{\ddot{x}_i^2 + \ddot{y}_i^2 + \ddot{z}_i^2} \tag{41}$$

where $\ddot{x}_i$, $\ddot{x}_i$ and $\ddot{x}_i$ are respectively the acceleration components along x, y and z axes acquired by the $_i$ sensor. Starting from the acceleration norms, two magnitudes are monitored, i.e., the maxima (Max) and the root mean squares (RMS). The assessment is carried out identifying the norm maxima in the same time interval in each acquisition: the time interval coincides with the e-scooter free response due to the second bump encountered by the front wheel. Figure 72 refers to the first tests conducted by the first participant at 5 and 25 km/h.

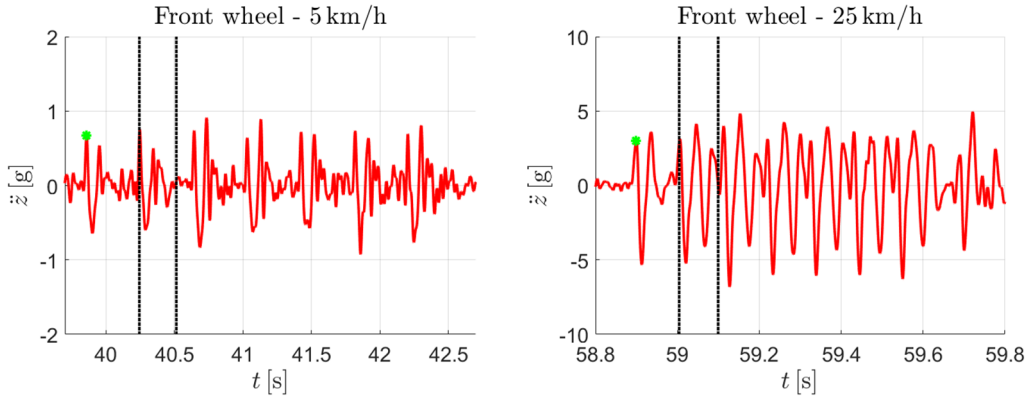

Figure 72 - Time interval used for the identification of norm maxima

The norm root mean squares are computed in the whole-time interval corresponding to the bump series. Even in this case, the identification of the time interval is carried out based on the front wheel vertical acceleration. Figure 73 refers to the first tests at 5 and 25 km/h performed by the first participant.

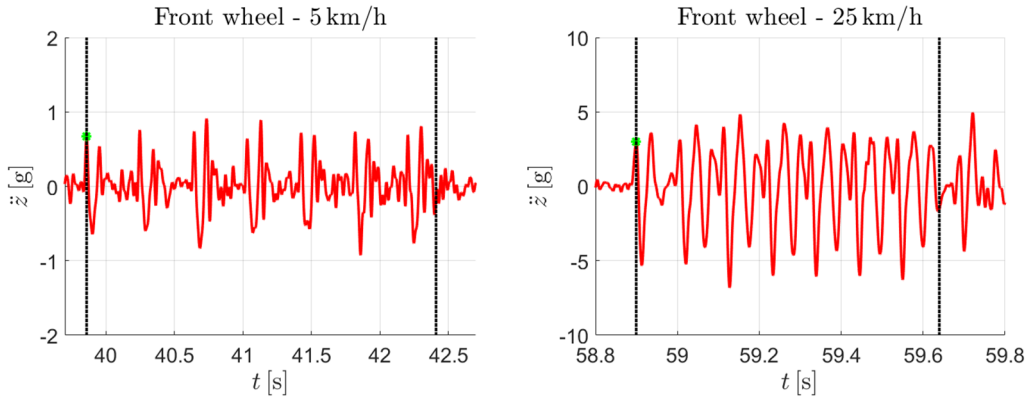

Figure 73 - Time interval used for the identification of norm RMS

5.4.3 Results

The following statistical tests are performed by IBM SPSS statistical software both on maxima and root mean squares, grouping the experimental tests and averaging the data according to several factors, highlighting relevant statistical differences. From Figure 74 to Figure 80, capital letters R and L refer to right and left limbs respectively. The application of the Shapiro-Wilk test (2-tails, significance level α equal to 0.05) preliminarily certifies the non-normal distribution of the data and imposes a non-parametric statistical analysis [65].

The first statistical investigation is focused on the comparison between the measuring areas which are relatively close but belong to the vehicle and the human body (handlebar and forearms, deck and shanks). Friedman test [66,67] is performed to verify if any statistical difference among triples of data exists. It is applied both on Max and the RMS averaging on the entire population. Since the Friedman test is positive, the post-hoc Wilcoxon signed-rank test [68] follows to find significant differences between couples of values (two-tailed, significance level α equal to 0.05). This kind of test is suitable to compare data referring to the same subjects but on different measuring areas. In the following, significant differences are highlighted using the statistical p-value (p). A single asterisk corresponds to p lower than 0.05 while two asterisks correspond to p lower than 0.01. Results in terms of maxima are reported in Figure 74 while results in terms of root mean squares are reported in Figure 75.

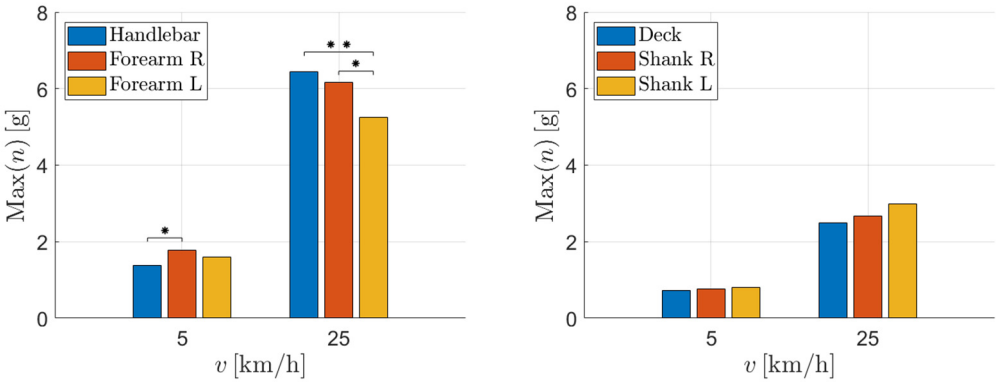

Figure 74 - Maxima belonging to handlebar/forearms (left) and to deck/shanks (right)

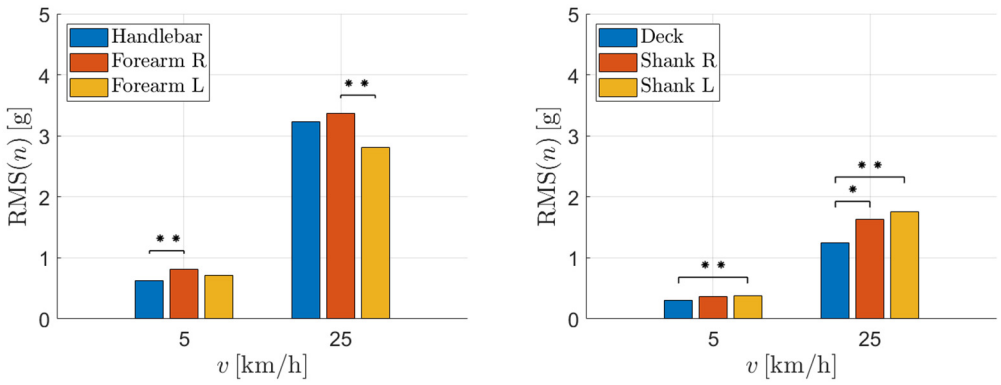

Figure 75 - Root mean squares belonging to handlebar/forearms (left) and to deck/shanks (right)

Considering the transmissibility of vibrations from the handlebar to the rider upper limb, significant differences are highlighted both in terms of maxima and root mean squares at 5 km/h and 25 km/h. Focusing on maxima, when the e-scooter velocity is high, the maxima of the forearms are significantly lower than the maximum of the handlebar. Right forearm maxima and root mean squares are generally higher than the left forearm ones: this evidence could be related to position of the accelerator (on the right part of the handlebar) and the braking lever (on the left part of the handlebar). Focusing on the comparison between the shanks and the deck, no significant differences is highlighted in terms of maxima. Shank root mean squares are higher than the deck one with some significance.

Mann-Whitney U test [69] is applied to evaluate the velocity effect on vibrations (2-tails, significance level α equal to 0.05). This kind of test is suitable to compare data referring to the same measuring area but in different operating conditions. Results are averaged on all the subjects and all the different segments are considered. Results in terms of maxima and root mean squares related to the different velocities are reported in Figure 76.

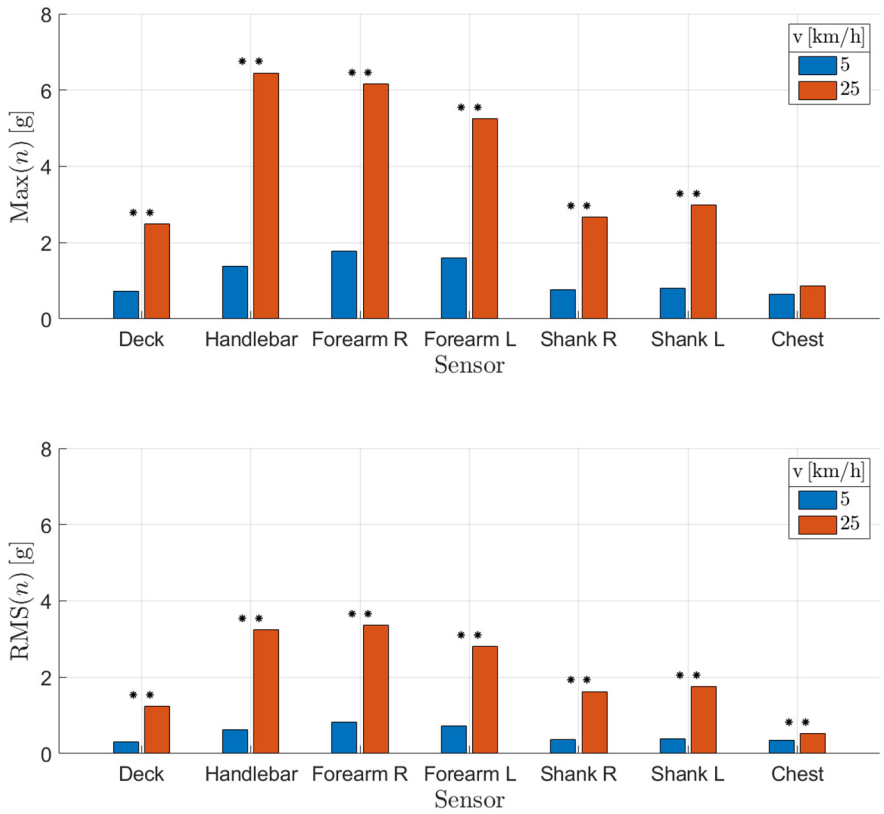

Figure 76 - Maxima and root mean squares clustering according to the velocity

Considering both maxima and root mean squares, the increase of e-scooter velocity produces a very significant increase in vibration in all the segments ($p << 0.01$). The unique different case is underlined in the maxima of the chest.

Mann-Whitney U test (2-tails, significance level: α equal to 0.05) is performed to compare males and females considering each segment and dividing the tests according to the velocity. Indeed, this statistical test is also used to analyse data belonging to the same measuring area but in different subjects. Differences between males and females at 5 km/h and 25 km/h are reported in Figure 77 (Max) and Figure 78 (RMS).

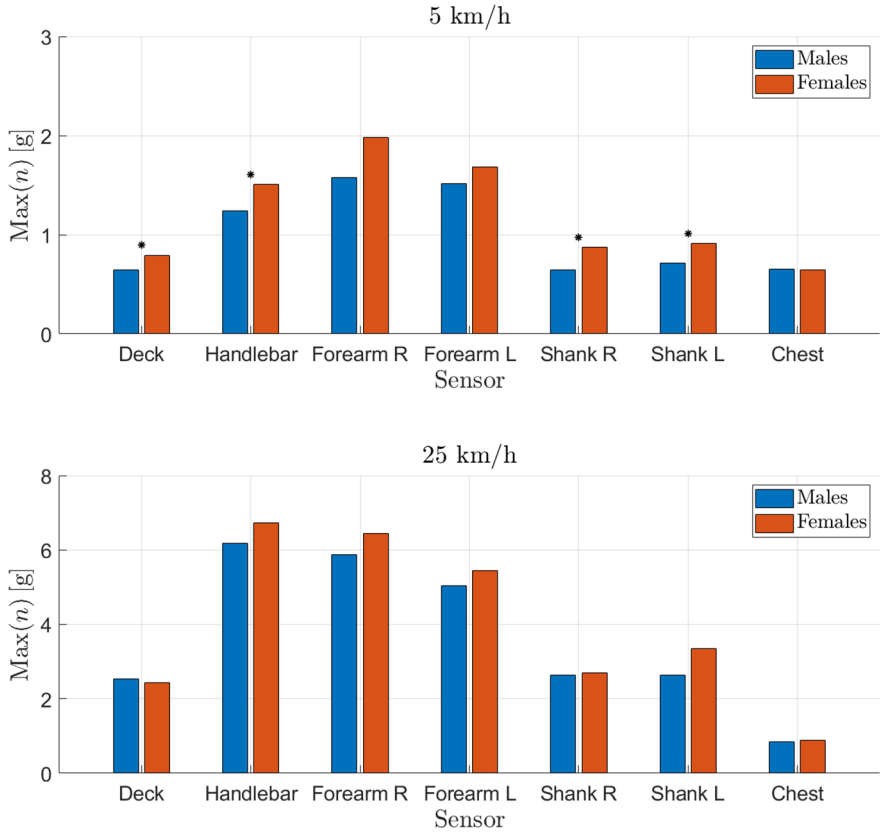

Figure 77 - Maxima clustering according to the rider gender

As general consideration, the maxima of the females are higher than the maxima of the males. Significant differences are only highlighted in terms of maxima in correspondence of the e-scooter sensors and the lower limbs at 5 km/h.

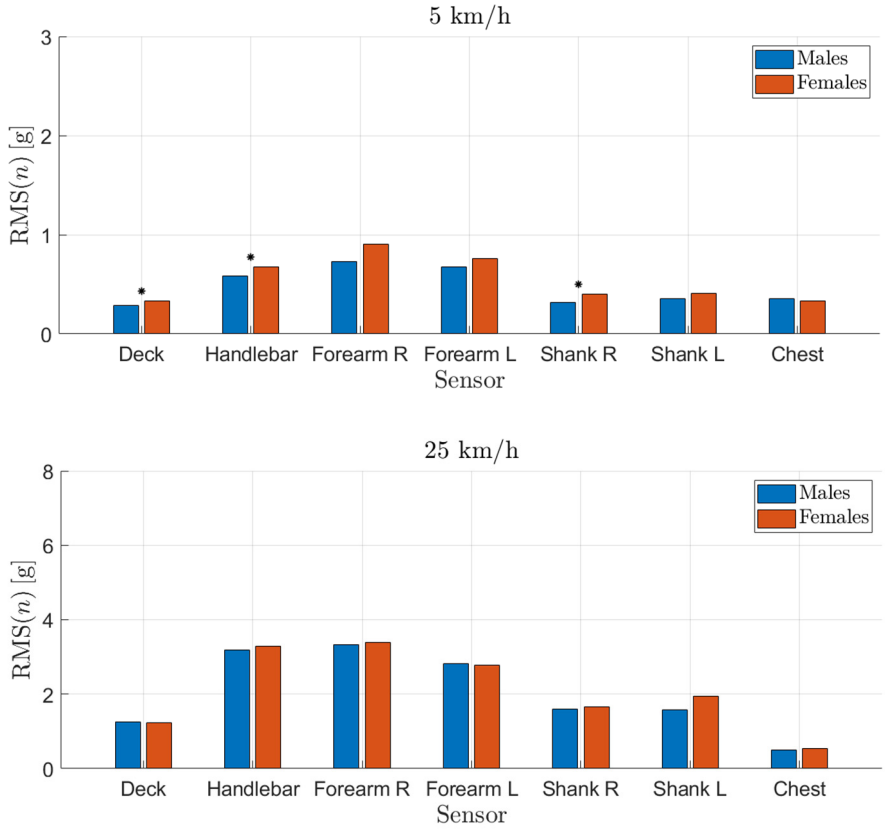

Figure 78 - Root mean squares clustering according to the rider gender

The difference between males and females is smoothened focusing on root mean squares. Significant differences occur also in correspondence of the deck, the handlebar and the right shank.

Subjects are finally divided into three groups based on their mass: less than 60 kg, in the range between 60 kg and 80 kg, more than 80 kg. A Friedman test followed by a post-hoc Mann-Whitney U test (two-tailed, significance level α equal to 0.05) is applied to compare the three groups. Differences in terms of maxima and root mean squares related to different riders' mass at 5 km/h and 25 km/h are reported in Figure 79 (Max) and Figure 80 (RMS).

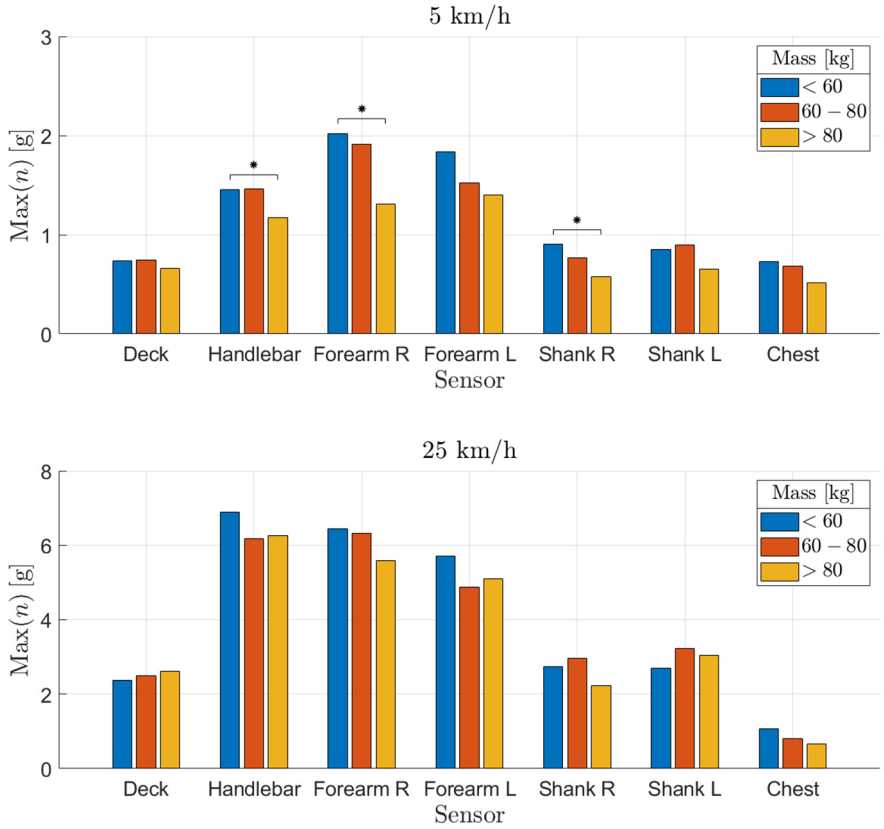

Figure 79 - Maximum of the norms, clustering according to the rider mass

As regards the handlebar, the right forearms, the left forearms and the chest, all maxima decrease with the rider's mass at both velocities. No statistical differences are highlighted in terms of maxima at 25 km/h.

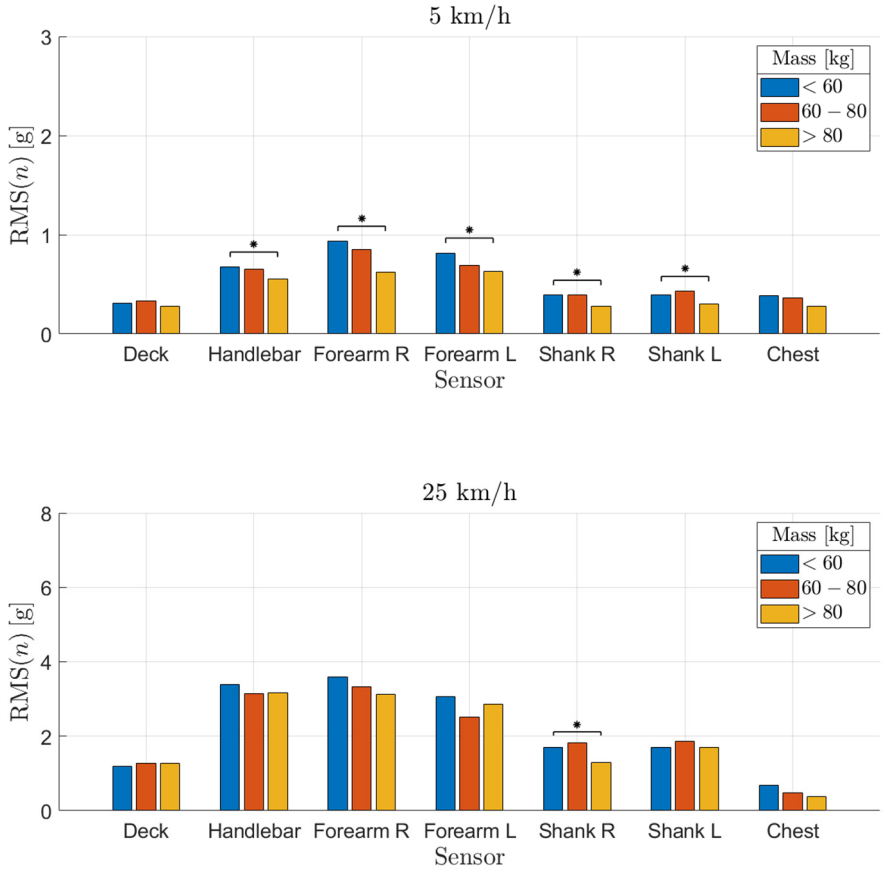

Figure 80 - Root mean square of the norms, clustering according to the rider mass

Focusing on the root mean squares at 5 km/h, there is always statistical difference between the lowest and highest mass groups, except for the deck and the chest. The consideration discussed for the maxima is also valid for the root mean squares. The results obtained comparing different mass classes are in line with the previous gender analysis. Indeed, the first group (< 60 kg) is tendentially composed of females, while the third one (> 80 kg) is composed of males. Accordingly, the mass of the rider influences the riding attitude, especially when the e-scooter velocity is low.

Subjects are also divided according to the dominant arm, the dominant foot, the foot position and the forward foot. Mann-Whitney U test (2-tails, significance level α equal to 0.05) does not highlight statistically significant differences for both maxima and root mean squares at both the velocities.

Chapter 6

Numerical simulation

As previously demonstrated by means of experimental tests and lumped parameter models, the rider motion relevantly affects the vehicle dynamics. The main reasons stand in the fact that the inertia of the human body is bigger than the inertia of the vehicle and that the rider/e-scooter system does not behave as a unique body. Moreover, the rider behaves differently, according to the manoeuvre and the road condition. The abovementioned reasons have led indeed the numerical research works on motorised two-wheeled vehicle to consider the rider as a system able to dynamically interact with the chassis and the handlebar. Thus, the strong hypothesis of rider as a single lumped inertia rigidly attached to the vehicle has been progressively removed. Cossalter et al. [70] considered a passive two-body rider in their mathematical model of motorbike. Zhu et al. [71] studied by an analytical model the effect of rider posture in a steady-state turning manoeuvre. Doria et al. [72] experimentally evaluated the frequency response functions of the rider and fitted a lumped parameter model to be integrated in a motorbike multibody model. Sequenzia et al. [73,74] included a fifteen-body rider in a multibody motorbike model developed in Adams/View. Rider's motion is reached applying torques in correspondence of the human joints and the effect on vehicle dynamics is shown in the simulation of a Monza lap. Bulsink et al. [75] investigated the lateral stability of bicycles through a multibody model developed in Adams considering a simplified four-body rider.

Another aspect common to the numerical modelling of two-wheeled vehicle stands in the fact that the vehicle is intrinsically unstable and requires a close loop

control. Besides the issues related to the modelling of the rider, even the tyre formulation deserves to be underlined. Traditional semi-empirical tyre models neglect the dynamics of the tyre structure and very short road irregularities. Although they provide accurate results for handling simulations, they are unsuitable for comfort analyses where the frequencies of interest are up to 100 Hz for whole-body vibrations and 1000 Hz for hand-transmitted vibrations. Following the research trends and driven by the abovementioned reasons, a detailed multibody model which includes the electric kick scooter, the rider and an advanced tyre model suitable for high frequency dynamics is developed and exploited to simulate some experimentally tested manoeuvres. The vehicle involved in the modelling is Xiaomi Pro II. The lateral equilibrium is achieved locking the roll and the lateral DOFs. Since the manoeuvre are in longitudinal direction, these model limitations do not impact on simulated results.

In this chapter the multibody model is presented in paragraph 6.1. In paragraph 6.2 the attention is focused on the braking manoeuvre. Paragraph 6.3 deals with the driving manoeuvre on the road with bumps.

6.1 Multibody model

It is preliminary decided to develop the multibody model in Matlab/Simscape Multibody. Previously known as SimMechanics, this multibody environment is designed for the simulation of all the typologies of mechanical 3D systems, such as robotics and land vehicles. The strength of Simscape Multibody stands in the fact that the model is developed in Matlab/Simulink, physically connecting equivalent blocks which represent bodies, joints, forces and other elements typically included in professional multibody environment. The advantages of using Simscape environment are several, among which the most relevant are:

- model parametrisation using Matlab variables;
- integration of control logics designed in Matlab/Simulink;
- integration of multi-physics plants using Simscape libraries.

Moreover, 3D geometries designed in CAD environment can be imported preserving inertia properties and boundaries. The model is developed in Matlab R2022b. The novelties of the presented multibody model are summarised in the following:

- the integration of a complete multibody mannequin characterised by dimensions and inertias in line with the real rider;
- the integration of an advanced tyre model, able to take into account short road irregularities and vibrations at high frequency.

Ride and handling behaviour of land wheeled vehicles is strictly dependent on tyre properties. High frequency vibrations are produced by road irregularities which are often shorter than the tyre contact patch. These are the reasons which led to use a tyre model able to cope with high frequency vibrations and to describe the tyre enveloping behaviour. The model has to be as accurate as possible, but simulation time must be consistent with the application.

The starting points of the modelling phase are reported in the following:

- the vehicle is built exploiting the inertias previously identified and shown in paragraph 2.2 and the CAD geometries as graphics;
- the human body is built by scratch including the main data of the rider who conducted the experimental tests;
- two roads are used in the simulation, the default flat one for the braking simulation and a specific road profile developed in Open CRG tool for simulating the uneven road.

A particular feature of the presented model is the usage of Simulink variant blocks. The advantage of using variants is the capability of developing and integrating different alternatives of a subsystem in the same model. In other words, variant blocks help representing multiple structural or algorithmic implementations of the same component in a single model and easily switching between them. The choice of the subsystem among the designed alternatives is carried out on the basis of a specific variable. The use of variants in the model design provides several advantages such as:

- use of the same model for many purposes;
- rapid prototyping without commenting out sections of the model;
- workflow speed by reducing model complexity;
- exploring different alternatives without altering the main model.

In the following some features common to all the simulations run within this research work are presented. In Table 37, the Matlab/Simscape joints used in the

presented model are reported, highlighting the degrees of freedom and the transformation sequence.

Table 37 - Matlab/Simscape joints

Type	Degrees of freedom	Transformation sequence
6-DOF	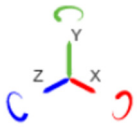	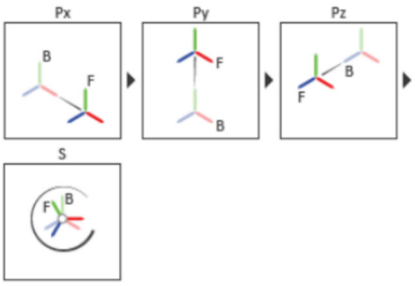
Bushing	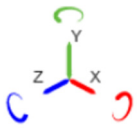	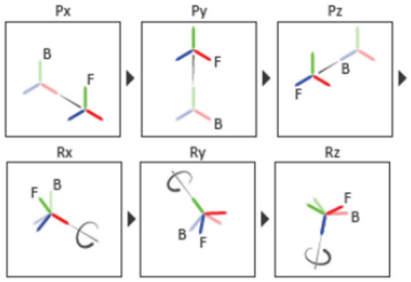
Gimbal	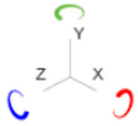	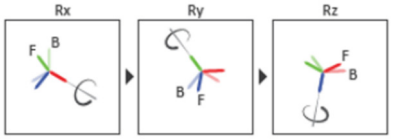
Planar	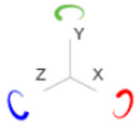	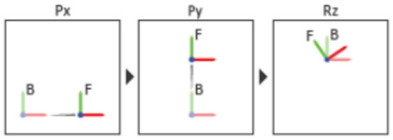
Revolute	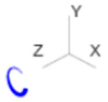	

Universal	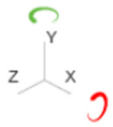	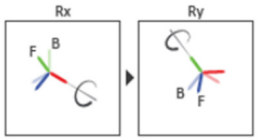

B: Base frame, F: Follower frame,
P: Prismatic primitive joint, R: Revolute prismatic joint

The variable-step ode23t solver is used. Table 38 reports the solver parameters.

Table 38 - Solver parameters

Base frame	**Follower frame**
Max step size	10^{-2}
Min step size	10^{-10}
Initial step size	10^{-6}
Absolute tolerance	10^{-3}
Relative tolerance	10^{-3}

The adopted solver settings are a good compromise between convergence and simulation time. The sampling frequency of the output signals is fixed at 1000 Hz. In subparagraph 6.1.1 the multibody model of the electric kick scooter is discussed. Then the advanced tyre model used for the simulation of road unevennesses is presented (subparagraph 6.1.2). In subparagraph 6.1.3, the multibody modelling of the rider is presented. The final multibody model in terms of Matlab/Simulink blocks and in the Matlab/Mechanics Explorer environment is reported in Figure 81 and Figure 82.

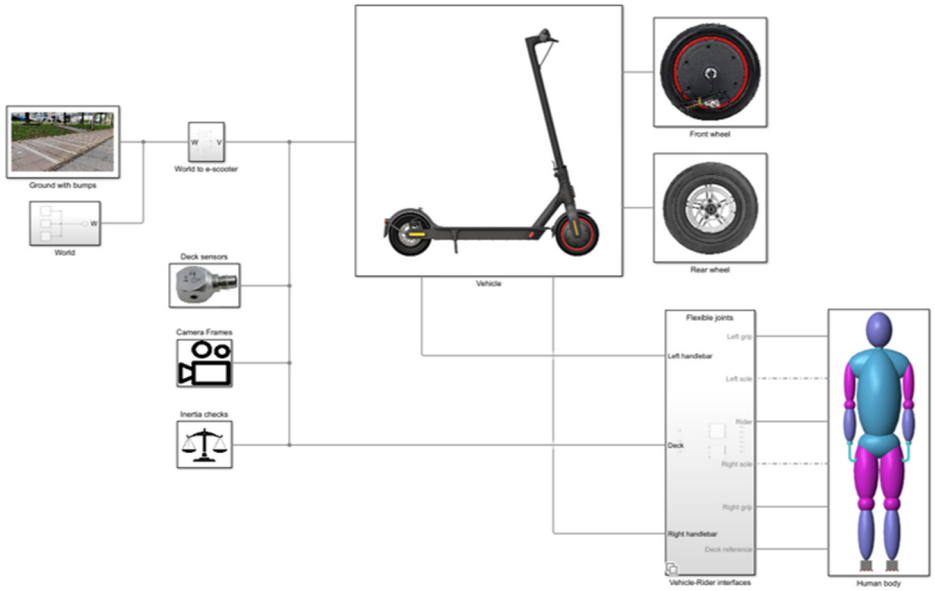

Figure 81 - Final multibody model (Matlab/Simulink)

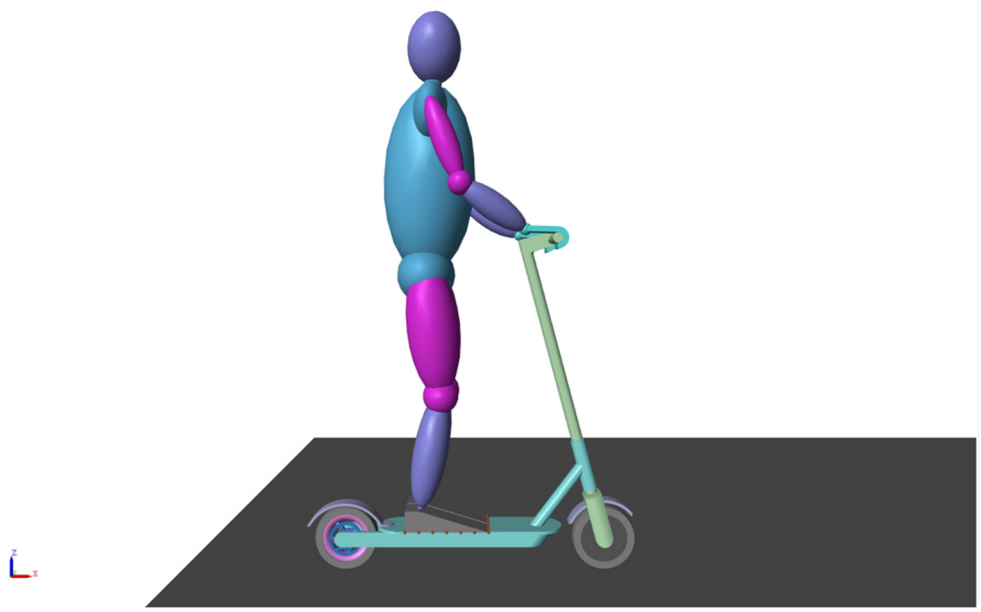

Figure 82 - Final multibody model (Matlab/Mechanics Explorer)

6.1.1 Electric kick scooter

Figure 83 represents the rigid bodies which constitute the vehicle multibody model. Parts and inertias are directly imported from the CAD model (Figure 13).

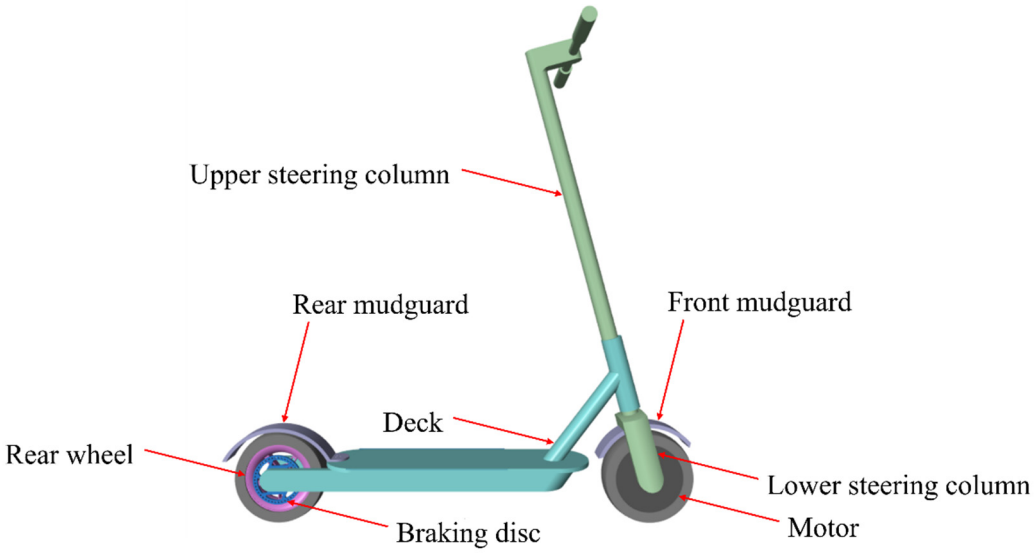

Figure 83 - E-scooter bodies

A 2D surface is set in correspondence of the deck floor in order to detect the contact with the foot soles, as described in subparagraph 6.1.2. Table 39 represents the joints between the bodies belonging to the vehicle multibody model. IMU sensor blocks are placed in correspondence of the sensors mounted during the experimental campaign (Figure 64).

Table 39 - E-scooter joints

Base frame	Follower frame	Type
Ground	Deck	6-DOF (1a) Planar (1b)
Deck	Rear mudguard	Locked
Deck	Rear wheel Braking disc	Revolute
Deck	Lower steering column	Locked (2a) Revolute (2b)
Lower steering column	Upper steering column	Locked (3a) Bushing (3b)
Lower steering column	Front mudguard	Locked

In the third column of Table 39, locked configuration refers to two bodies connected each other without the usage of a joint. In this way the two bodies are rigidly connected. The brackets underline the usage of variant blocks. The e-scooter deck can be connected to the ground letting free all the six degrees of freedom (1a) or locking the translation along y axis, the roll motion and the yaw motion (1b). The steering column is divided into two parts with respect to the CAD parts. This solution makes the multibody model closer to the real vehicle assembly and at the same time allows to better describe the steering column flexibility and the clearance of the steering joint. The lower steering column can be locked onto the deck (2a) or rotate around the steering axis (2b). The first alternative can be useful in the simulation of longitudinal manoeuvres. The upper steering column part can be rigidly connected to the lower steering column part, or a bushing joint can be introduced between the two bodies. In the real vehicle, the two parts which compose the steering column are not a unique component but are divided and joined by means of a hinge which allows the vehicle folding. The bushing joint is properly tuned to reproduce the vibrations detected on the handlebar as shown in the following. To do so, a test rig (Figure 84) is developed

to evaluate the system response, in terms of vertical accelerations, given a certain input of vertical displacement.

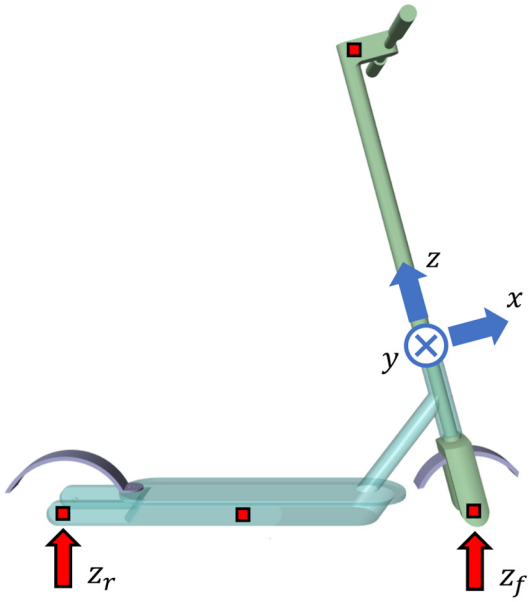

Figure 84 - Test rig for the multibody model of the e-scooter

The motion is provided in correspondence of the wheel centre. The experimental vertical accelerations detected driving at 25 km/h on the road with bumps at the front and rear wheels (Figure 52) are filtered with a high-pass band filter (cut-off frequency equal to 1 Hz) and integrated twice. They are used to assign the vertical motion inputs (Figure 85).

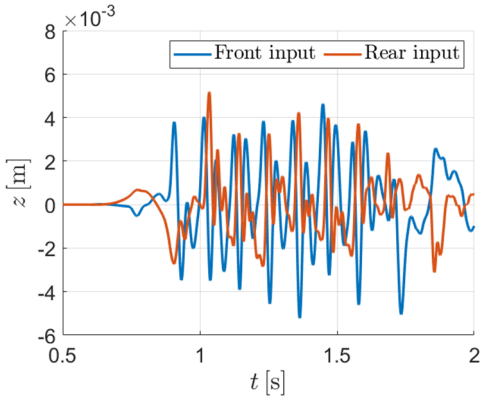

Figure 85 - Front and rear input at 25 km/h

Figure 86 represents the comparison between the experimental (blue lines) and the simulated (red lines) accelerations. Simulated results are achieved locking

the lower steering column part to the upper steering column part (3a configuration in Table 39). The signal synchronisation is obtained in correspondence of the first positive peak of the front wheel vertical acceleration.

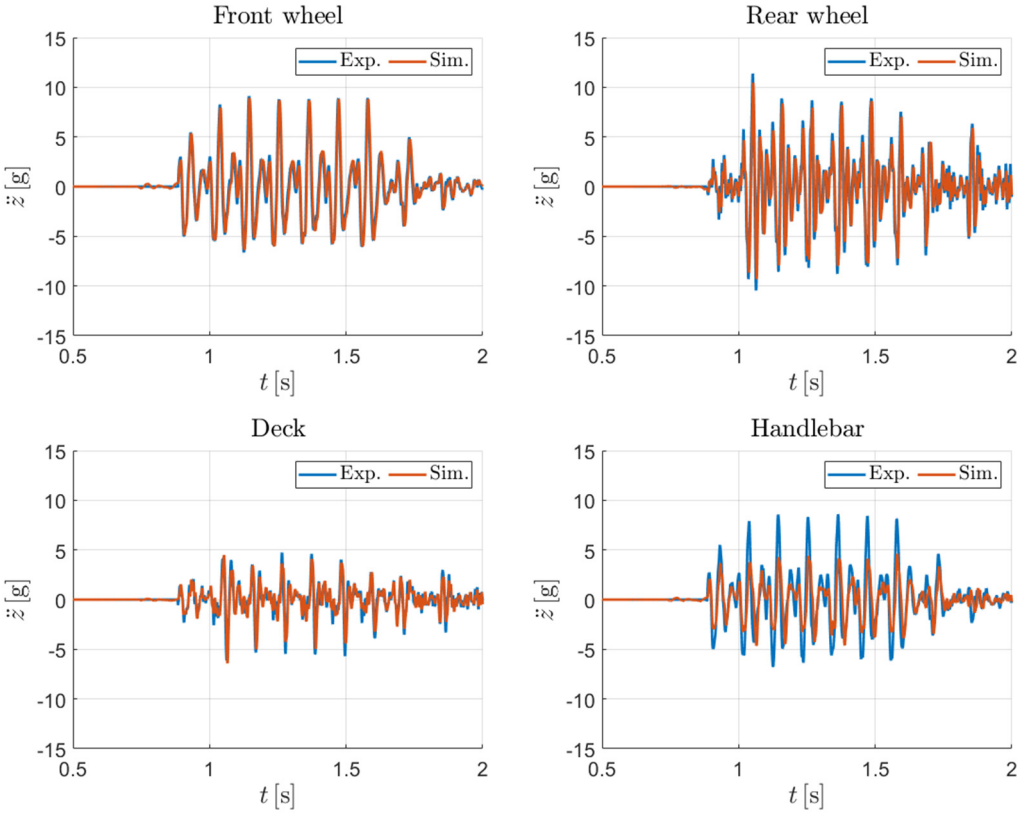

Figure 86 - Experimental-numerical comparison in terms of vertical accelerations simulating the road input at 25 km/h

A good matching is evidenced in all the measurement areas apart from the handlebar. The vertical acceleration experimentally detected on the handlebar is in phase but higher in amplitude than the numerical one underlining that the steering column and the deck do not behave as a unique rigid body. The difference can be due to the flexibility of the steering column and/or the clearance of the steering joint. Additional investigations are required to correctly identify the cause of this evidence. For the sake of simplicity of the model, the underlined compliance is lumped in the steering bushing whose stiffness characteristic is tuned with the purpose of minimising the difference between experimental and simulated signal on the handlebar. Table 40 represents the final values of stiffnesses and damping coefficients.

Table 40 - Stiffnesses and damping coefficients of the steering bushing

DOFs	Stiffness	Damping coefficient
x/y	10^6 N/m	$5 \cdot 10^4$ Ns/m
z	10^6 N/m	$5 \cdot 10^4$ Ns/m
rx/ry	5 Nm/°	0.25 Nms/°
rz	10^6 Nm/°	$5 \cdot 10^4$ Nms/°

Figure 87 represents the numerical-experimental comparison of the handlebar vertical acceleration after the introduction of the bushing (3b configuration in Table 39).

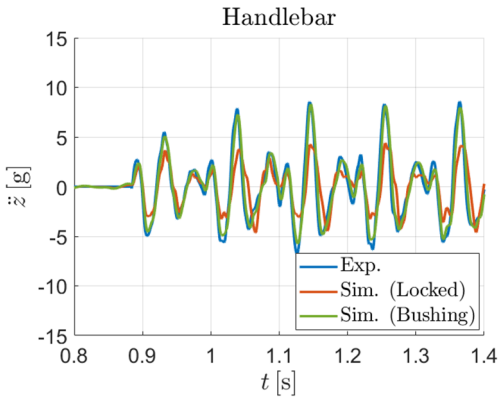

Figure 87 - Vertical acceleration of the handlebar after the steering bushing tuning at 25 km/h

The hypothesis at the basis of the presented tuning process is that the rider does not influence the motion of the handlebar during the manoeuvre by means of his inertia. As it will be shown in the next paragraphs, this assumption is reasonable since the supporting force exerted by the handlebar on the rider upper limb is only relevant during pure longitudinal manoeuvre as the braking. The rider does not use the handlebar to maintain the longitudinal balance in the normal driving, even during the crossing of small road unevennesses.

Finally, the electric motor can be controlled by the accelerator exploiting the motor characteristics shown in Figure 43 or directly in terms of velocity, exploiting the revolute joint between the deck and the motor.

6.1.2 Tyre

Several tyre models, characterised by different levels of details, are nowadays available in professional multibody codes for vehicle simulations [76,77]. In the last years, the interest on tyres has shifted from handling (low frequency dynamics) to control systems and NVH analyses (high frequency dynamics). Among the advanced tyre models, able to take into account frequencies higher than 60 Hz, FTire, RMOD-K and SWIFT are the most widespread [78–80]. The tyre formulation used in this multibody modelling is the most recent and advanced version of the world-renowned Pacejka Magic Formula (MF) tyre model [59], i.e., MF-Tyre/MF-Swift 6.2. A brief overview on Pacejka tyre model evolution and more details on MF-Tyre/MF-Swift are provided in Appendix C.

The necessity of integrating in the e-scooter multibody model an advance tyre formulation derives from the fact that road irregularities (bumps, potholes, etc.) generate high frequency vibrations which affect driver's comfort and health. The main effects of short wavelengths obstacles stand in non-linear horizontal and vertical tyre forces and the change of the effective rolling radius [80].

Since its first versions, MF-Tyre/MF-Swift tyre model is composed by four main subsystems [80]:

- the Magic Formula (MF-Tyre);
- the contact patch slip model (MF-Tyre);
- the rigid ring model (MF-Tyre/MF-Swift);
- the road enveloping model (MF-Tyre/MF-Swift).

Magic Formula and contact patch slip model refer respectively to the capability of the model to describe forces and moments in steady-state conditions and the spatial delay to achieve the tyre response given a certain input. Rigid ring model is the optional plug-in package which allows to consider the dynamics of the tyre. The strength of this extension is considering the tyre-wheel assembly as composed by two rigid bodies, i.e., the rim and the belt. The tyre belt, whose flexibility is neglected, is elastically suspended to the wheel rim. Coherence in terms of tyre stiffnesses between the Magic Formula model and the rigid ring

model is guaranteed adding residual stiffnesses. The common assumption of both simple and complex formulations is that the contact between the tyre and the road surface is constituted by a single point, where the slip is calculated, and forces and moments are applied. The fourth subsystem is also a plug-in package, needed for the computation of an equivalent road input starting from the real road elevation. The assumptions in the road profile computation are the following:

- the quasi-static response of the tyre with a single-point contact on the effective road is equal to the quasi-static response of the real tyre on the real road;
- local dynamics in the contact area can be neglected.

MF-Tyre/MF-Swift allows to turn on the several abovementioned features, shifting from the simplest models to the advanced one in all the main vehicle simulation packages, including Matlab/Simscape. The rigid ring model in combination with the envelope model has been experimentally validated on potholes, bumps and broad-band random signals [81]. Figure 88 represents the workflow of the integration of the rigid ring model with the road envelope model.

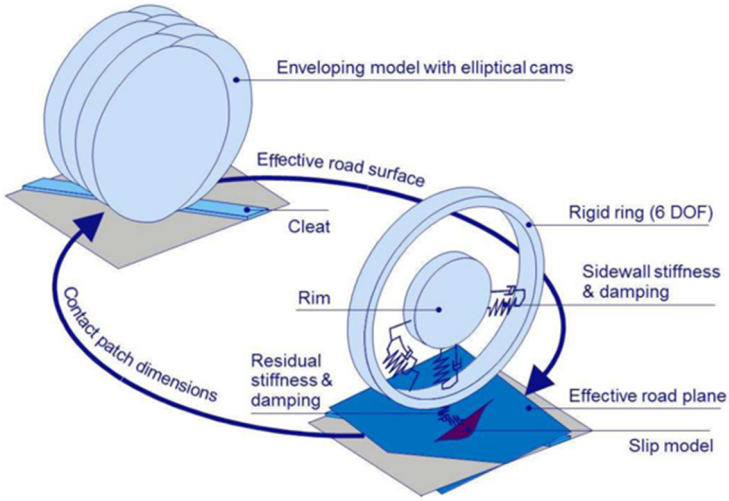

Figure 88 - Integration of the enveloping and rigid ring models [82]

The first parameters required by the model are the wheel inertial properties: mass and moments of inertia are read from the CAD model (Figure 13) paying attention to the difference between the front and the rear wheel. Since the tyre characterisation required by the model is time consuming and expensive, Siemens_car205_60R15.tir tyre property file is used as starting point. In the following, the modifications on the tyre parameters are explained. Tyre

asymmetry due to conicity and plies is removed due to the fact that the vehicle is two-wheeled. Even the lateral force and self-alignment moment computation is disabled since the simulated manoeuvres imply driving straight forwards. Table 41 reports the original and the modified parameters referring to the [DIMENSION] section of the tyre property file.

Table 41 - Geometrical parameters in the tyre property file

	Value	
Parameters	**205/60R15**	**Modified**
UNLOADED_RADIUS [m]	0.3135	0.108
WIDTH [m]	0.205	0.05
RIM_RADIUS [m]	0.1905	0.078
RIM_WIDTH [m]	0.152	0.035

Tyre (UNLOADED_RADIUS and WIDTH) and wheel rim (RIM_RADIUS and RIM_WIDTH) geometrical properties are taken from the CAD model of Xiaomi Pro II e-scooter (Figure 13). Table 42 reports the original and the modified parameters referring to the [INERTIA] section of the tyre property file.

Table 42 - Inertial parameters in the tyre property file

Parameters		Value	
		205/60R15	**Modified**
MASS [kg]	m_t	9.3	0.48
IXX [kgm^2]	$J_{x,t}$	0.391	0.0024
IYY [kgm^2]	$J_{y,t}$	0.736	0.0048
BELT_MASS [kg]	m_b	7.698	0.408
BELT_IXX [kgm^2]	$J_{x,b}$	0.352	0.0018
BELT_IYY [kgm^2]	$J_{y,b}$	0.489	0.0036

The inertial properties of the whole tyre (MASS, IXX and IYY) are evaluated from the CAD model (Figure 13) while the inertias of the belt (BELT_MASS, BELT_IXX and BELT_IYY) are computed scaling the tyre inertias and keeping constant the ratios of the original parameters. Table 43 reports the original and the modified parameters referring to the [VERTICAL] section of the tyre property file.

Table 43 - Vertical dynamics parameters in the tyre property file

Parameters	Symbol	Value	
		205/60R15	**Modified**
FNOMIN [N]	F_{z0}	4000	500
VERTICAL_STIFFNESS [N/m]	C_z	209652	100000

The vertical stiffness of the whole tyre (VERTICAL_STIFFNESS) in correspondence of the nominal vertical force (FNOMIN) is the value identified in the tyre characterisation (Figure 24). Table 44 reports the original and the modified parameters referring to the [STRUCTURAL] section of the tyre property file. The same parameters are reported in the rigid ring sketch in Figure 118.

Table 44 - Structural parameters in the tyre property file

		Value	
Parameters	**Symbol**	**205/60R15**	**Modified**
LONGITUDINAL_STIFFNESS [N/m]	C_x	381913	38191
FREQ_LONG [Hz]	f_x	76.6	100
FREQ_WINDUP [Hz]	f_θ	67.7	112
DAMP_LONG [-]	ζ_x	0.05	5
DAMP_ WINDUP [-]	ζ_θ	0.05	1.4

With regards to the dynamic behaviour of the tyre in the longitudinal direction, the longitudinal and wind-up frequencies of the belt, f_x and f_θ, are used to compute the belt stiffnesses in the radial ($C_{bx} = C_{bz}$) and in the tangential ($C_{b\theta}$) directions, according to Eqs (42) and (43).

$$C_{bx} = C_{bz} = m_b(2\pi f_\theta)^2 \tag{42}$$

$$C_{b\theta} = C_{bz} = I_{y,b}(2\pi f_\theta)^2 \tag{43}$$

The overall tyre longitudinal stiffness is the result of a series of lumped springs, according to Eq. (44).

$$\frac{1}{C_x} = \frac{1}{C_{bx}} + \frac{R_l^2}{C_{b\theta}} + \frac{1}{C_{rx}} + \frac{a}{C_{fk}}$$

(44)

R_l represents the loaded radius, a and C_{fk} are respectively the contact patch length and stiffness in the longitudinal direction. These parameters are computed on the basis of other empirical data in the tyre property file. C_{rx} is the residual stiffness in the longitudinal direction which allows the matching between the Magic Formula model and the rigid ring. Damping coefficients of the belt in the radial (k_{bx}) and in the circumferential ($k_{b\theta}$) directions are computed according to Eqs (45) and (46).

$$k_{bx} = k_{bz} = 4\pi\zeta_x f_x m_b$$

(45)

$$k_{b\theta} = k_{bz} = 4\pi\zeta_\theta f_\theta J_{y,b}$$

(46)

The vertical dynamic behaviour of the tyre according to the rigid ring formulation is modelled as two springs in series, as shown in Eq. (47).

$$\frac{1}{C_z} = \frac{1}{C_{bz}} + \frac{1}{C_{rz}}$$

(47)

C_{bz} is equal to C_{bx} since it represents the radial stiffness of the belt while C_{rz} is the residual vertical stiffness used to match the results of the simplest tyre model and the rigid ring.

6.1.3 Human body

Human body model is built by scratch in Matlab/Simscape. The model is constituted by fourteen rigid parts and thirteen joints. The main simplification as concerns rigid bodies is neglecting the flexibility of the spine column and the soft tissues (skin, muscles, inner organs, etc) [83–85]. The manoeuvres to be simulated always involve the rider in the standing position: the flexibility of the torso is expected to be negligible compared to the joint motion. The contribution of the soft tissues is important in vehicle simulation for analysing the restraint systems (belt and airbag) or crash events [86]: it is generally included by FE modelling. However, models of human body for vehicle dynamics simulation are generally constituted by rigid bodies only [72,73,87,88]. When it is possible, the joint kinematics standard proposed by the International Society of Biomechanics is followed [89,90]. Figure 89 represents the bodies and the joints included in the rider model.

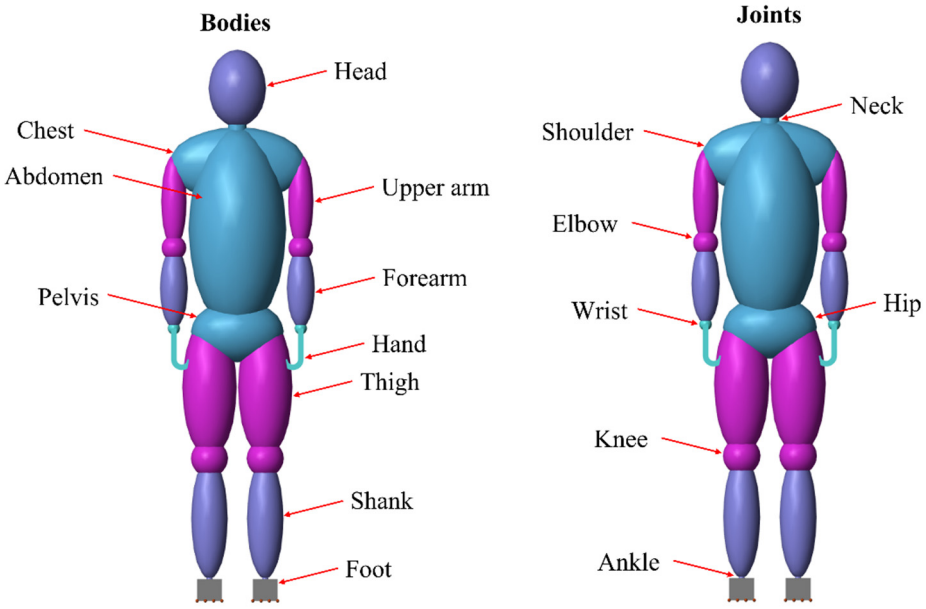

Figure 89 - Rider bodies (left) and joints (right)

Each rigid body is composed of one rigid segment at least. All the segments are modelled as simple geometries. Apart from the feet and the hands, which are modelled as extruded solids, and the neck, which is modelled as a cylinder, all the segments are characterised by an ellipsoidal shape. Equivalent dimensions of each segment are physically measured on the reference rider. Table 45 reports the human body segments, their geometries, the main sizes and the rigid body they belong to.

Table 45 - Rider segments and their dimensions of the multibody dummy model

Segment	Shape	Dimensions			Rigid body	Quantity
		r_1	r_2/h	r_3		
Head	Ellipsoid	0.093		0.125	(1)	1
Neck	Cylinder	0.030	0.050		(2)	1
Chest	Ellipsoid	0.065	0.170	0.360		
Abdomen	Ellipsoid	0.158		0.330		
Pelvis	Ellipsoid	0.100	0.150	0.360		
Thigh	Ellipsoid	0.088		0.230	(3)	2
Knee	Ellipsoid	0.060				
Shank	Ellipsoid	0.060		0.195	(4)	2
Ankle	Ellipsoid	0.01			(5)	2
Foot	Solid					
Upper arm	Ellipsoid	0.041		0.150	(6)	2
Elbow	Ellipsoid	0.040				
Forearm	Ellipsoid	0.045		0.130	(7)	2
Wrist	Ellipsoid	0.02			(8)	2
Hand	Solid					

The hand is modelled as the extrusion of a rectangle (which stands for the palm) and a hollow cylinder (which stands for fingers). The foot is modelled as the extrusion of a trapezoid. Figure 90 represents the models of the foot and the hand included in the multibody model.

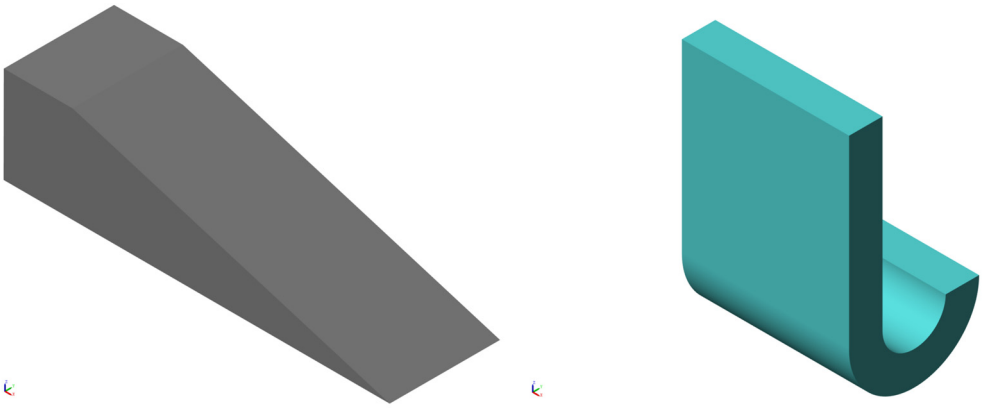

Figure 90 - Foot and hand model

Even though the addition of the joint segments implies some graphical interpenetration, they are used to add inertia in correspondence of the human body joints as in the real case. A unique value of material density (equal to 930 kg/m^3) is assigned to all the segments in order to get the mass of the reference rider. Table 46 represents the joints between the bodies.

Table 46 - Human body joints

Joint	Type	Base-Follower frame	Motion
Neck	Gimbal	Head-Chest	Flexion-Extension Lateral bending Rotation
Shoulder	Gimbal	Chest-Upper arm	Flexion-Extension Abduction-Adduction Internal-External rotation
Elbow	Universal	Upper arm-Forearm	Flexion-Extension Supination-Pronation
Wrist	Universal	Forearm-Hand	Flexion-Extension Ulnar-Radial
Hip	Gimbal	Chest-Thigh	Flexion-Extension Abduction-Adduction Internal-External rotation
Knee	Revolute	Thigh-Shank	Flexion-Extension
Ankle	Gimbal	Shank-Foot	Dorsiflexion-Plantarflexion Inversion-Eversion Abduction-Adduction

A variant block is used in correspondence of each human body joint in order to switch between locked/unlocked joint configuration. In addition to the intrinsic kinematics, each joint motion has been characterised by the features here reported:

- initial conditions [°];
- equilibrium position [°];
- stiffness [Nm/°] and damping coefficient [Nms/°];
- lower and upper motion end stop [°], end stop stiffness [Nm/°], end stop damping coefficient [Nms/°] and transition region [°];

- external torques.

The initial conditions are set equal to the equilibrium positions. Figure 89 refers to the human body in the standing configuration, which conventionally corresponds to the equilibrium joint positions equal to 0°. The stiffnesses and the damping coefficients are tuned according to the manoeuvres as it is shown in the following paragraph. The end stops are used to limit the angular motion while external torques can be assigned to actively control the model. Table 47 represents the equilibrium positions of the human body joints.

Table 47 - Equilibrium positions of the human body joints

Joint	Motion	Equilibrium [°]
Neck	Flexion-Extension	0
	Lateral bending	0
	Rotation	0
Shoulder	Flexion-Extension	22
	Abduction-Adduction	5.6
	Internal-External rotation	−28
Elbow	Flexion-Extension	40.4
	Supination-Pronation	64.5
Wrist	Flexion-Extension	−13.2
	Ulnar-Radial	32.3
Hip	Flexion-Extension	−8.4
	Abduction-Adduction	3.1
	Internal-External rotation	0.4
Knee	Flexion-Extension	16.6
Ankle	Dorsiflexion-Plantarflexion	−10.3
	Inversion-Eversion	−2.8
	Abduction-Adduction	−0.8

Table 48 represents the end stop bounds of the human body joints.

Table 48 - End stop bounds of the human body joints

Joint	Motion	End stop bound [°]
Neck	Flexion-Extension	$-50 : 50$
	Lateral bending	± 15
	Rotation	± 60
Shoulder	Flexion-Extension	$0 : 180$
	Abduction-Adduction	$0 : 180$
	Internal-External rotation	$-90 : 90$
Elbow	Flexion-Extension	$0 : 160$
	Supination-Pronation	$-90 : 90$
Wrist	Flexion-Extension	± 70
	Ulnar-Radial	± 30
Hip	Flexion-Extension	$-100 : -10$
	Abduction-Adduction	± 30
	Internal-External rotation	± 30
Knee	Flexion-Extension	$0 : 70$
Ankle	Dorsiflexion-Plantarflexion	± 30
	Inversion-Eversion	± 30
	Abduction-Adduction	± 30

The end stop stiffnesses and damping coefficients are respectively set equal to 10 Nm/° and 0.1 Nms/°.

The interface between the human body model and the external world are represented by a couple of revolute joints, in correspondence of the hands, and a couple of contact forces, in correspondence of the foot soles. A grid of massless points is created under the feet to detect the contact with other bodies. Figure 91 represents the mesh grid under a foot sole.

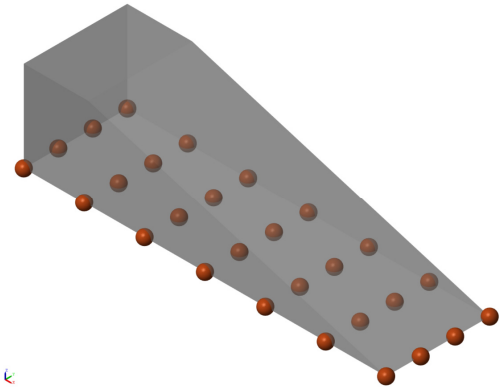

Figure 91 - Mesh grid under the foot sole

Each point is able to generate a normal force f_n (Eq. (48)) and a tangential force f_f (Eq. (49)) at the contact as shown in Figure 92.

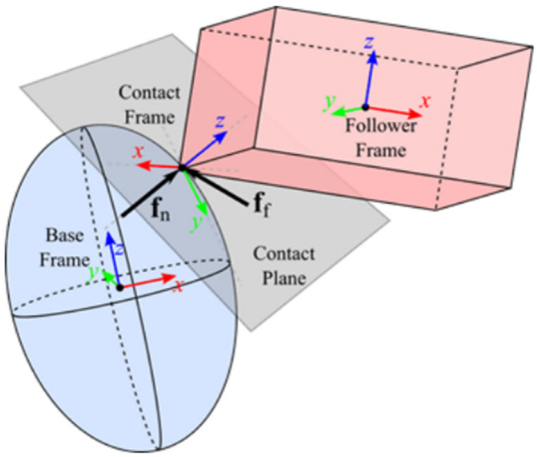

Figure 92 - Sketch of the spatial contact force

The normal force pushes against two surfaces in order to oppose the penetration while the tangential force opposes the relative tangential velocity,

$$f_n = s(d, w) \cdot (kd + cd') \tag{48}$$

where:

- d is the penetration depth between the two contacting surfaces;
- d' is the time derivative of d;
- k and c are respectively the normal force stiffness and damping coefficient;
- w represents the contact transition region;
- $s(d, w)$ is a smoothing function, it is 0 when d is equal to 0 while it is 1 when d is equal to w. The smoothing function has zero derivative at the origin.

Frictional force follows the stick-slip approach:

$$|f_t| = \mu |f_n| \tag{49}$$

where μ is the effective friction coefficient and it is function of the static (μ_{static}) and the dynamic ($\mu_{dynamic}$) friction coefficient, as shown in

Figure 93. At the critical tangential velocity, the effective friction coefficient reaches the maximum which is equal to the static value.

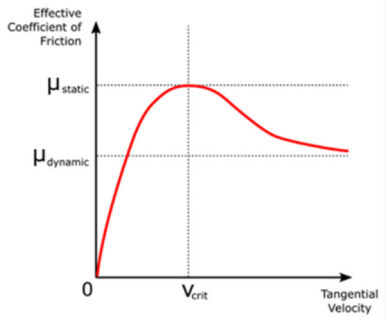

Figure 93 - Friction coefficient in function of the tangential velocity

Table 49 reports the contact force parameters between the foot sole and the deck.

Table 49 - Contact force parameters

k [N/m]	10^{-5}
c [Ns/m]	10^{-3}
w [m]	10^{-4}
μ_{static} [-]	1
$\mu_{dynamic}$ [-]	1
v_{cr} [m/s]	10^{-3}

For sake of completeness, Table 50 reports the mass and the principal moments of inertia of the final model.

Table 50 - Inertias of the human body model

m [kg]	76.6
J_X [kgm^2]	12.45
J_Y [kgm^2]	12.00
J_Z [kgm^2]	0.91

The center of mass is in the symmetry plane, almost in the middle of the footprint along x axis while it is located at the distance of 1.01 m from the ground along z axis (almost the 56% of the whole height). Figure 94 represents the centre of mass and the principal axes of inertia (X, Y, Z) of the final model. The resultant location centre of mass and moments of inertia are in line with [91,92].

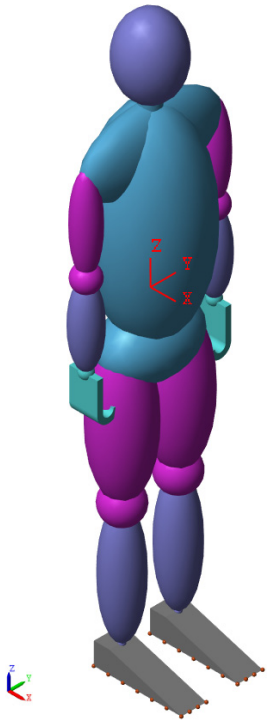

Figure 94 - Human body principal axes

In the locked joint configuration, the human body system is clamped on the deck and the rigid connections between the bodies are rotated in order to reproduce exactly the same posture of the unlocked case.

6.2 Heavy braking manoeuvre

This paragraph deals with the simulation of the heavy braking manoeuvre exploiting the passive version of the rider, i.e., without applying any torque in the anatomical joint. The following settings are adopted in the braking simulation:

- deck is connected to the ground by the planar joint (1a configuration in Table 39);
- the lower steering column part is rigidly connected to the deck (2a configuration in Table 39) and the bushing is turned on (3b configuration in Table 39);
- the electric motor is controlled in torque;
- the rider model is in the flexible mode and no torque is applied to the human body joints;

- default flat road, the smooth road contact method, and the relaxation behaviour (Table 64) are used.

The simulated manoeuvre consists of three phases:

- static settling of the multibody system;
- acceleration up to the maximum e-scooter velocity;
- full braking command in 0.1 s.

Experimental and numerical results are synchronised on the basis of the angular velocity of the rear wheel. The hypothesis on the basis of the method proposed to tune the model consists of considering the rider as a passive system during the braking manoeuvre. The objective is tuning the rotational stiffnesses and damping coefficients of the human body joints in order to reproduce both the vehicle performance and the rider kinematics in simulation. The human body model consists of 13 joints which involves 31 rotational stiffnesses and 31 damping coefficients for an initial number of unknowns equal to 62. High stiffnesses and damping coefficients are assigned to the neck joint thus considering the head as rigidly connected to the chest and assuming that the motion of the head does not relevantly affect the results. The same speech is extended to the rotational stiffnesses and damping coefficients at the interface between the hand and the handlebar. The number of unknowns is brought to 54. Two further assumptions are made to significantly reduce the number of unknowns:

- stiffnesses belonging to the same joint but referred to independent axes are considered equal;
- the ratio between the damping coefficient and the stiffness is the same for each joint and is kept constant.

The ratio between the damping coefficient and the stiffness is initially assumed equal to 1.5%: afterwards it is included as a parameter of the optimisation not remarking significant differences in the results. The number of parameters to be tuned is therefore reduced to 7.

6.2.1 Model tuning

The unknown parameters, i.e., the stiffnesses and the damping coefficients which characterise the human body joints, are identified through an optimisation process carried out in the Parameter Estimator tool of Matlab/Simulink. The

optimisation problem consists of minimising the difference between experimental and simulated signals. The cost function C is based on the sum squared error and is reported in Eq. (50),

$$C = \sum_{j=1}^{m} \left(\frac{\sum_{k=1}^{n} s_{j,k} - e_{j,k}}{\max|e_j|} \right)^2 \tag{50}$$

where:

- e_j is the j^{th} experimental signal;
- s_j is the corresponding simulated signal;
- n is the number of samples in the optimisation time interval T_{opt};
- m is the number of observed signals.

It is worth underlining that the experimental and the simulated output must be characterised by a coherent sampling frequency. T_{opt} is equal to 0.5 s, corresponding to the initial phase of the braking manoeuvre. The optimisation method and algorithm are respectively the nonlinear least squares and trust-region-reflective. Optimisation parameters are reported in Table 51.

Table 51 - Optimisation parameters

Parameter	**Value**
Parameter tolerance	10^{-3}
Function tolerance	10^{-3}
Maximum iteration	10^{2}

Other optimisation methods and algorithms are tested, not observing relevant improvements. The parameter variables, i.e., the rotational stiffnesses, are normalised by a reference value equal to 2.4 Nm/°. The initial condition of the optimisation is randomly chosen; the normalised upper and lower bound are respectively 0 and 30, corresponding to a completely free and extremely stiff joint

condition respectively. The optimisations are relaunched with different initial conditions, not observing significant differences.

6.2.2 Results

The robustness of the method is assessed providing to the optimisation tool more and more experimental signal to be fitted.

Table 52 - Experimental signals in the three optimisation runs

Optimisation run	Experimental signals
1	e-scooter longitudinal acceleration
2	e-scooter longitudinal acceleration left shank y axis angular velocity
3	e-scooter longitudinal acceleration left shank y axis angular velocity chest y axis angular velocity

In each optimisation run, the joints are progressively turning on or off in order to evaluate their effect on the rider response, reducing the number of variables and aiding the optimisation process. Table 53, Table 54 and Table 55 report the cost function evaluated at the end of each optimisation for several joint configurations. In reference to each optimisation, the following symbols are adopted:

- V stands for a joint in which the stiffness is varied (Variable);
- F stands for a joint in which the stiffness is equal to 0 (Free);
- L stands for a joint in which a very high stiffness is assigned (Locked).

Prior to the optimisations, it is observed on the upper limb that:

- one joint (shoulder, elbow, wrist, ankle) must be set variable at least to ensure the pitch equilibrium of the rider system;
- no joint (shoulder, elbow, wrist) must be locked since this condition implies the complete rigidity of the entire rider system.

The sub-runs corresponding to the minimum and maximum cost functions are highlighted respectively in green and red in Table 53, Table 54 and Table 55.

The first optimisation run is carried out considering only the experimental longitudinal acceleration of the e-scooter. Table 53 reports the cost function evaluated at the end of the first optimisations considering the contribution of the several human body joints.

Table 53 - Cost function evaluated in several joint configurations (1st run)

	Joint						
Opt.	**Ankle**	**Knee**	**Hip**	**Shoulder**	**Elbow**	**Wrist**	C
1a	F	L	L	F	V	F	1.64
1b	F	L	L	V	F	F	1.20
1c	F	L	L	V	V	F	1.20
1d	F	L	L	V	V	V	1.20
1e	F	L	V	V	F	F	0.53
1f	F	V	V	V	F	F	0.56
1g	V	V	V	V	F	F	0.53
1h	F	V	L	V	F	F	1.08

V: Variable, F: Free, L: Locked

In relation to optimisations (1a) and (1b) in Table 53, the e-scooter acceleration is closer to the experimental one acting on the shoulder and letting free the elbow rather than acting on the elbow and letting free the shoulder. This is a consequence of the type of joint (and the related degrees of freedom) which is different between the shoulder and the elbow (see Table 46). If the shoulder stiffness is variable, elbow and wrist stiffnesses seems to be irrelevant (optimisations (1c) and (1d)). From now on, the elbow and the wrist will be left

free while the shoulder stiffness always constitute an optimisation variable. Another joint which is strongly related to the rider response in the braking manoeuvre is the hip. In general, results are closer to the experimental one in the simulations which involve the hip stiffness. In the best configurations, all the lower limb joint and the shoulder stiffnesses are optimised, while the elbow and the wrist are left free. Experimental and numerical e-scooter longitudinal acceleration, chest and left shank angular velocities around y axis after optimisation (1g) are reported in Figure 95.

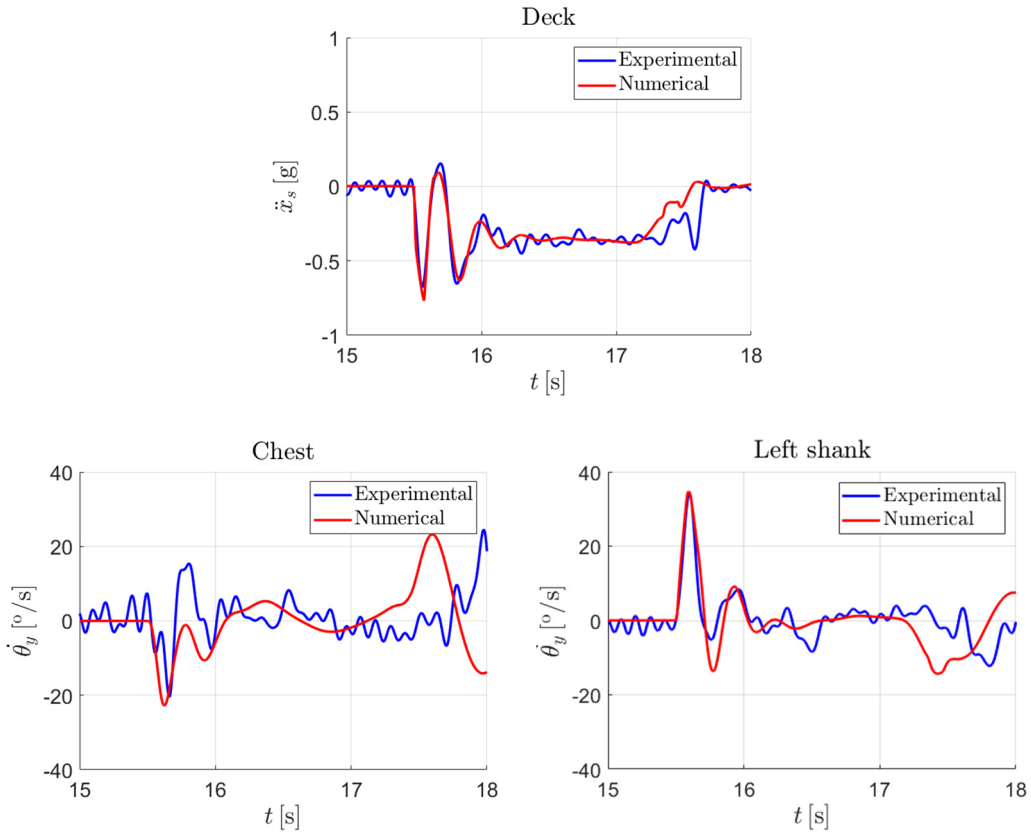

Figure 95 - Experimental-numerical comparison after the optimisation (1g)

As shown in Figure 95, a good agreement between experimental and numerical signals is reached just optimising the longitudinal acceleration of the e-scooter. The main difference can be remarked in the chest angular motion. Optimisation (1i) qualitatively produces comparable results to optimisation (1g).

The second optimization run is carried out considering the experimental longitudinal acceleration of the e-scooter and the angular velocity of the left shank around y axis. Table 54 reports the cost function evaluated at the end of the

second optimisations considering the contribution of the several human body joints.

Table 54 - Cost function evaluated in several joint configurations (2nd run)

	Joint						
Opt.	**Ankle**	**Knee**	**Hip**	**Shoulder**	**Elbow**	**Wrist**	C
2a	F	L	V	V	F	F	2.61
2b	F	V	V	V	F	F	2.67
2c	V	V	V	V	F	F	1.58

V: Variable, F: Free, L: Locked

In the best configuration, all the lower limb joint and the shoulder stiffnesses are optimised, while the elbow and the wrist are left free, as happened in the previous optimisation run (see Table 53). Experimental and numerical e-scooter longitudinal acceleration, chest and left shank angular velocities around y axis after the optimisation (2c) are reported in Figure 96.

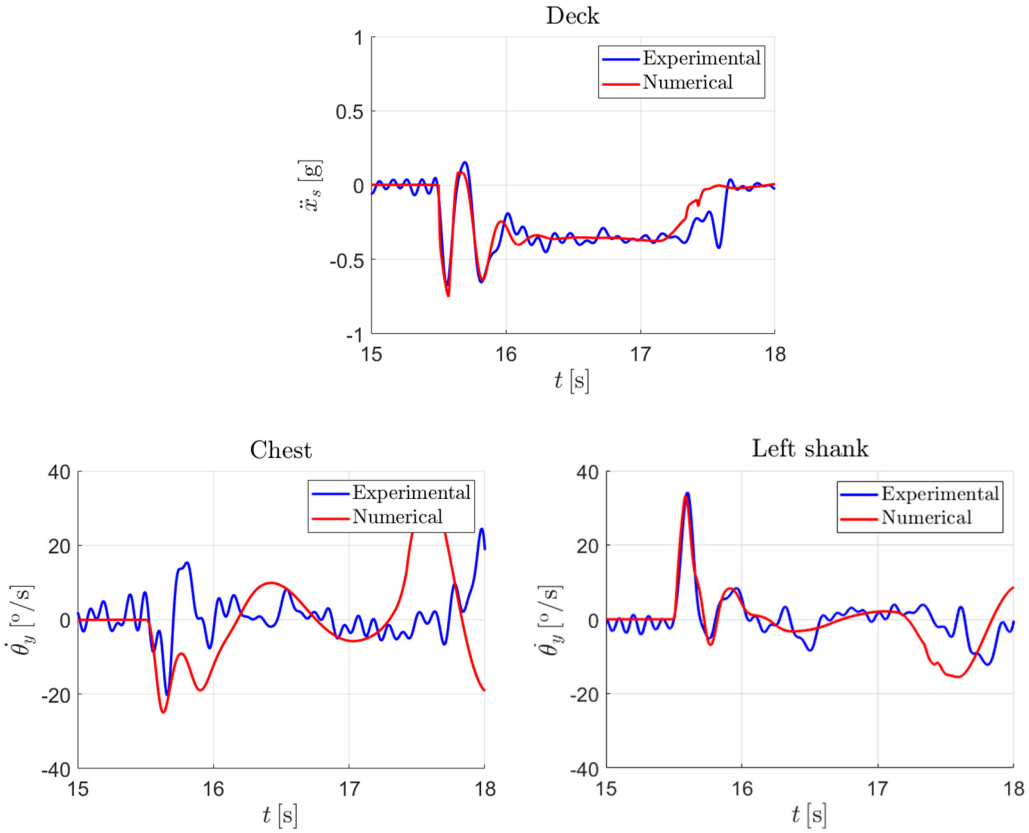

Figure 96 - Experimental-numerical comparison after the optimisation (2c)

No improvements in the longitudinal acceleration of the e-scooter can be detected while a very good matching in terms of left shank angular velocity is reached. The chest angular velocity continues to be different with respect to the experimental signal.

The third optimization run is carried out considering the experimental longitudinal acceleration of the e-scooter, the angular velocities of the left shank and the chest around y axis. Table 55 reports the cost function evaluated at the end of the third optimisations considering the contribution of the several human body joints.

Table 55 - Cost function evaluated in several joint configurations (3rd run)

	Joint						
Opt.	**Ankle**	**Knee**	**Hip**	**Shoulder**	**Elbow**	**Wrist**	C
3a	F	L	V	V	F	F	13.06
3b	F	V	V	V	F	F	13.38
3c	V	V	V	V	F	F	10.75

V: Variable, F: Free, L: Locked

As occurred in the previous optimisation runs (see Table 53 and Table 54), the best configuration involves the optimisation of all the lower limb joint and the shoulder stiffnesses, while the elbow and the wrist are left free. Experimental and numerical rear wheel angular velocity, e-scooter longitudinal acceleration, e-scooter pitch rate, chest and left shank angular velocities around y axis after the optimisation (3c) are reported in Figure 97.

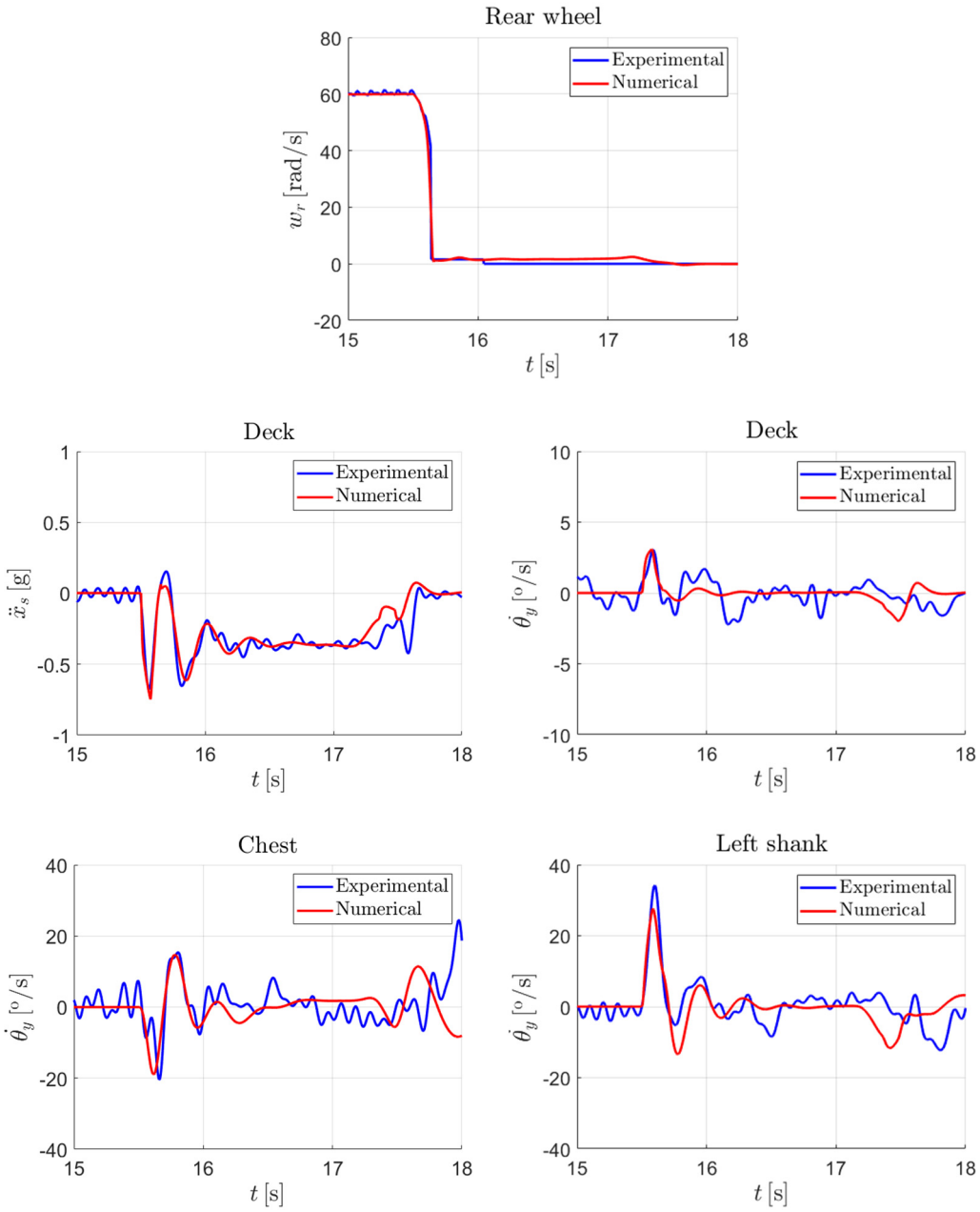

Figure 97 - Experimental-numerical comparison after the optimisation (3c)

As evidenced by Figure 97, all the simulated signals are in good agreement with the corresponding experimental ones. No differences can be appreciated in the e-scooter longitudinal acceleration while a little deterioration of the left shank angular velocity brings to a relevant improvement in the chest motion.

For the sake of completeness, the human body joint stiffnesses are reported in Table 56.

Table 56 - Joint stiffnesses after the final best run (3c)

	Joint					
	Ankle	**Knee**	**Hip**	**Shoulder**	**Elbow**	**Wrist**
k [Nm/°]	7.68	3.62	1.42	2.28	0	0

6.3 Bump-crossing

This paragraph deals with the simulation of the manoeuvre involving the vertical dynamics of the system and consisting of the crossing of the road bumps discussed in paragraph 4.2, 5.3 and 5.4. The following settings are adopted in the model in the driving on the bumps:

- deck body is connected to the ground by the planar joint (1a configuration in Table 39);
- the lower steering column part is rigidly connected to the deck (2a configuration Table 39) and the bushing is turned on (3b configuration Table 39);
- the electric motor is controlled in velocity;
- tyre is set in order to use the opencrg road, the envelope contact method and the rigid ring dynamics (Table 64).

The first subparagraph deals with the road generation while the second subparagraph on the relevant results.

6.3.1 Road model

Since envelope contact method and rigid ring dynamic model must be used for vibration analyses, the only possible way to define the road is the Curved Regular Grid (CRG) format. CRG is a file format able to store high-precision information from road surface scans [93,94]. The road format has been developed since 1995 by Daimler and made public since 2005 in an open-source code called

OpenCRG. This method is particularly useful as road input for different tyre models and simulation package in order to perform vehicle durability and comfort analyses. The main advantages of this file format are represented by high accuracy in terms of road data, memory efficiency, low computation effort for the generation of the road file and during the manoeuvre simulations. Among the storable data, the road elevation and the friction coefficient are the most important. The managing of the road surface is based on a mesh grid and a road reference line. The grid is constituted by columns and rows which respectively corresponds to longitudinal and lateral cuts of the road. Longitudinal and lateral cuts are always parallel and perpendicular with respect to the centre line. The minimum parameters to obtain a road reference line are the length and the width. The reference line can be characterised by a start coordinate and an end coordinate, the heading angle, the bank angle and the elevation. Road local height is defined on the basis of the mesh grid. OpenCRG library is also developed in Matlab in order to read, plot, modify and generate CRG files. It is used in the current research work for the creation of a new road profile based on the path experimentally tested (see subparagraph 3.2.1). The road includes seven bumps of rectangular cross-section, equally spaced. The main dimensions are reported in Table 57.

Table 57 - Bump geometry

Length [m]	0.08
Height [m]	0.004
Clearance [m]	0.65

The first step is constituted by the creation of a 2D road profile starting from the geometrical properties. The longitudinal spatial step is set equal to 1 mm in order to have high accuracy. The rectangular cross-section is approximated with a trapezoidal cross-section: the rising and the falling bump edges become ramp of length equal to 1 mm. This approximation is necessary to get a one-to-one correspondence between the x and the z road coordinates. A gap of 30 m is placed between the origin of the road and the first bump to allow the e-scooter to reach the target velocity of the simulation. Figure 98 refers to the 2D road profile.

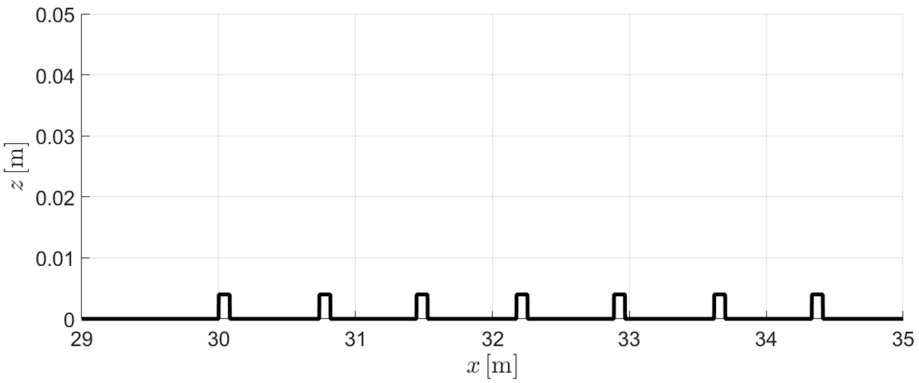

Figure 98 - 2D road profile

2D road profile in Figure 98 is used for the generation of the correspondence 3D road. The 3D road is characterised by a width of 4 m transversally cut in three sections. The final road is plotted in Figure 99 exploiting the OpenCRG library functions.

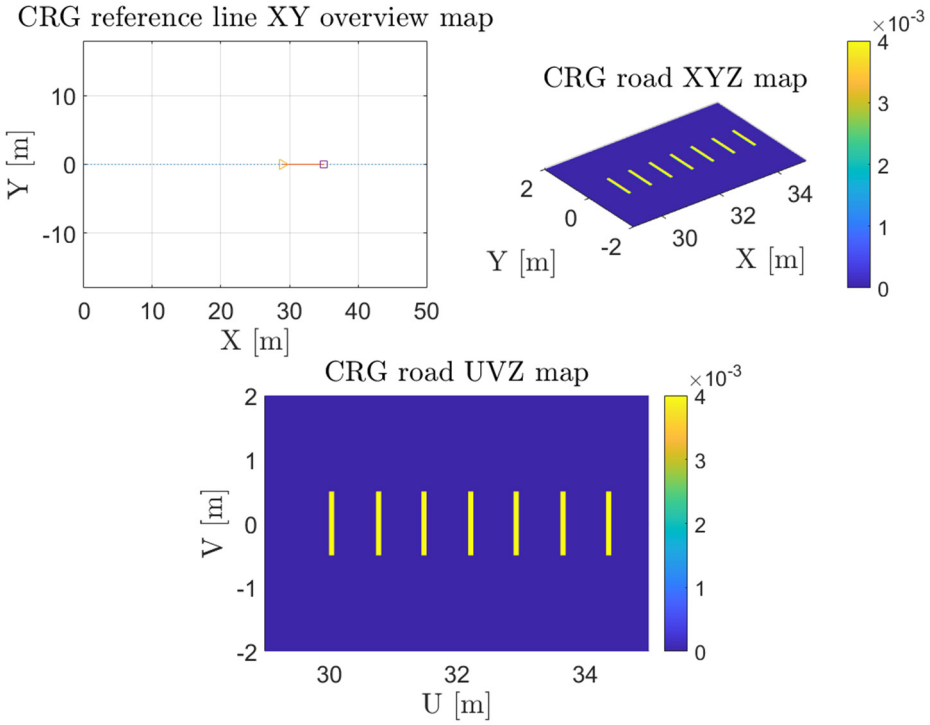

Figure 99 - Road in CRG format

6.3.2 Results

The following experimental-numerical comparison is reported in terms of vertical acceleration of the front wheel and angular velocity of the deck. As shown in subparagraph 6.1.1, apart from the steering column, all the e-scooter behaves like a unique rigid body. Thus, the vertical dynamics of the e-scooter deck can be defined knowing the vertical motion of a generic point (corresponding to the front wheel in this case) and its angular motion. The synchronisation between the experimental data and the simulated signals is based on the first peak of the vertical acceleration which corresponds to the climb of the first bump. A good agreement between the experimental and the simulated signals proves a challenging task due to the rider's response and his interaction with the vehicle. As previously underlined, the mass of the rider is predominant with respect to the mass of the e-scooter (the ratio is almost 5.5: 1). Moreover, it is noticed that a unique rider's setting in simulation cannot satisfied the correlation at different velocities, suggesting that the rider's behaviour involuntarily changes with speed. Several attempts to reproduce the human body and e-scooter dynamics are carried out. In the following, the best correlations obtained at 5, 15 and 15 km/h are proposed. Blue lines correspond to the experimental results already presented in paragraph 4.2; red lines correspond to the simulated data. Figure 100 refers to the comparison at 5 km/h.

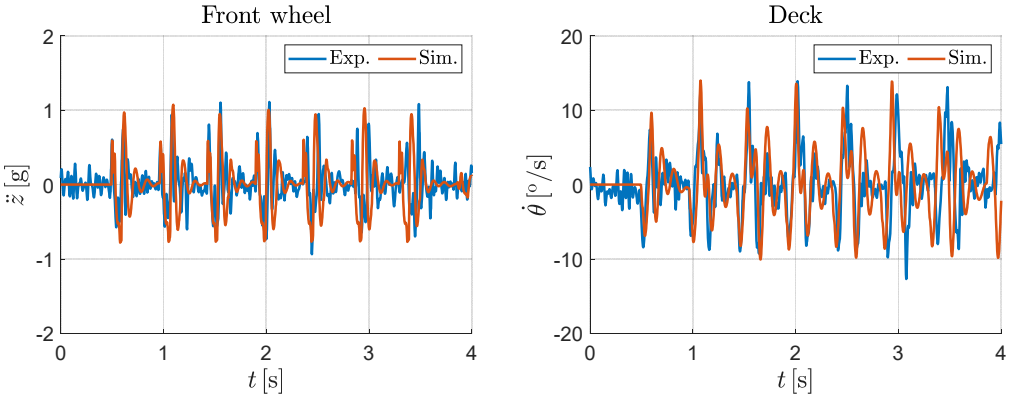

Figure 100 - Front wheel vertical acceleration (left) and deck pitch rate (right) at 5 km/h

A good matching with the experimental signals is achieved at 5 km/h locking all the human body joints and clamping the rider on the vehicle. This evidence suggests that the rider tends to be very rigid and tightly attached to the vehicle at low velocity. This rigidity can be related to the roll equilibrium of the system which is precarious driving at low velocity. Misalignment between the

experimental and the numerical signals, especially evident in correspondence of the last two bumps, are due to a reduction of the vehicle velocity in the experimental test. Figure 101 refers to the comparison at 15 km/h.

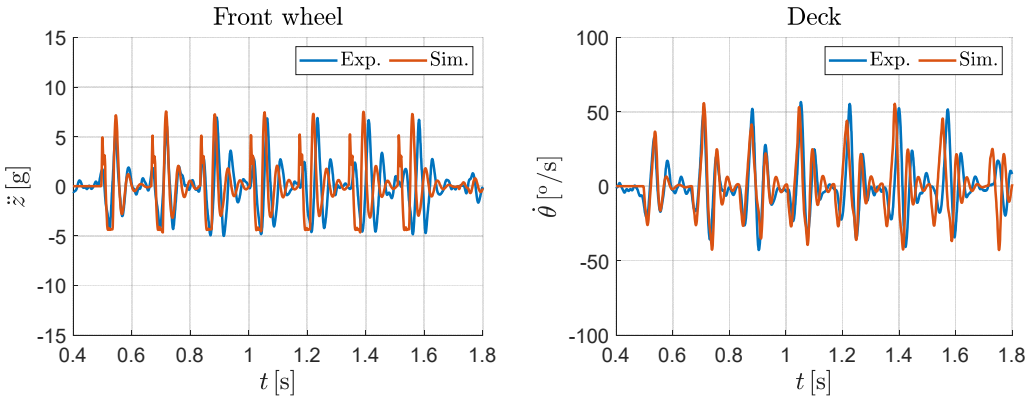

Figure 101 - Front wheel vertical acceleration (left) and deck pitch rate (right) at 15 km/h

The results proposed in Figure 101 are obtained replacing the human body system with a forced corresponding to the rider's weight applied on the deck floor. The location of the applied force is identified in order to ensure the right static load in correspondence of the tyre (Table 13). This simplification in the model allows achieving a better correlation with the experimental evidence, thus suggesting that the dynamics of the rider tends to be decoupled from the dynamics of the e-scooter for high velocity. This behaviour of the rider can be an involuntary action to experience a lower level of vibrations due to the road univenesses. From the vehicle point of view, the only effect due to the rider at higher speeds is the human body weight: no inertial effect due to the rider's mass is detected. The same effect could be obtained keeping the anatomical model of the rider and actively controlling the joints to minimise its inertial forces caused by bounce and pitch motions. Since no interaction in terms of force exchange between the human body and the handlebar is required to achieve the reported results, it is concluded that the pitch equilibrium of the rider can be reached only by the effect of the lower limb joints and by the upper limb joints. Even at 15 km/h a slight misalignment can be highlighted due to the variation of the vehicle velocity in experimental tests. Figure 102 refers to the comparison at 25 km/h.

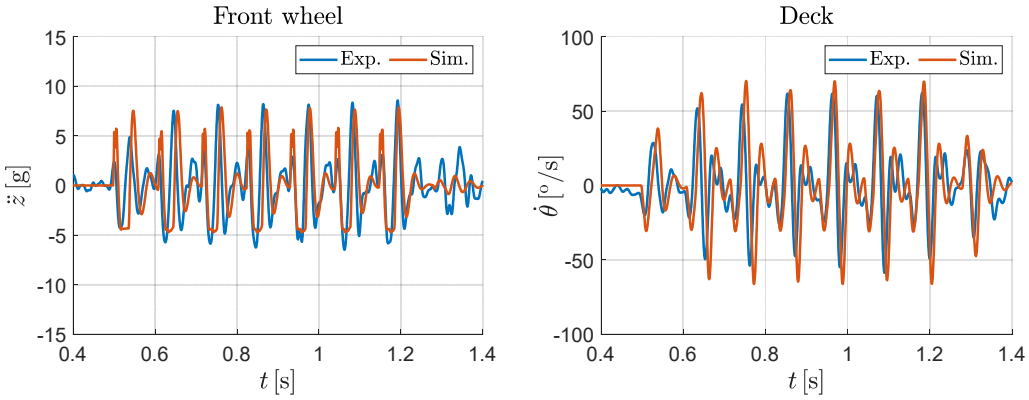

Figure 102 - Front wheel vertical acceleration (left) and deck pitch rate (right) at 25 km/h

Even in this case the good comparison is obtained replacing the human body system with the equivalent force due to the rider's weight confirming that the dynamics of the rider is decoupled from the dynamics of the e-scooter. As general comment regarding the analyses at 5, 15 and 25 km/h, both amplitudes and frequencies of the numerical results are in agreement with the acquired signals. It can be concluded that the tyre and road modelling which are firstly developed for ride comfort analysis in the automotive field are also suitable for this kind of vehicle simulation. For sake of completeness, the experimental-numerical comparison at 5 km/h is reported in Figure 103 adopting the standard (green solid line) and the advanced (red solid line) version of magic formula tyre model. The standard version, which does not include the rigid ring model and the road enveloping function, is not able to correctly reproduce the system response due to the dimensions of the road obstacle and the involved frequencies.

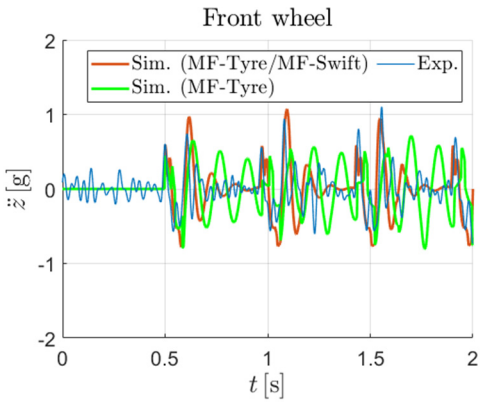

Figure 103 - Front wheel vertical acceleration at 5 km/h using standard and advanced version of the magic formula tyre model

Chapter 7

Conclusions

The presented PhD dissertation aims at assessing the ride performances of electric kick scooters through experimental testing and numerical modelling. A special focus is given to the effect of human body dynamics on the rider/vehicle system. Two commercial electric kick scooters, characterised by different design solutions, are involved for this purpose.

The preliminary analyses and the longitudinal tests allow to identify the main features of the vehicles, such as the inertias, the tyre radial stiffness, the electric motor characteristics in driving and regeneration, how the braking is guaranteed through the mechanical system and the electric motor. A simplified lumped parameter model is tuned on the basis of the experimental evidence and exploited to verify the effect of the rider's motion during light and heavy braking manoeuvres in terms of vehicle longitudinal acceleration.

The second part of this research activity is focused on vertical dynamics and ride comfort. A significant difference between the two electric scooters both on lumped road irregularities and homogeneous surfaces is highlighted by an experimental comparing campaign. The gap depends both on tyre properties (size and stiffness) and the presence of the suspension system. The methodology provided by ISO 2631-1 and ISO 5349-1 to assess comfort quality turns out to be an efficient instrument to compare vehicles but does not offer a univocal benchmark to evaluate a single case. Velocity is a parameter which strongly affects ride comfort and pavé road emphasises the difference between the

vehicles. The final comfort indexes related to the hand-transmitted and the whole-body vibrations are similar in terms of general trend but are differently scaled according to the original vibrations and the frequency weightings. However, it is suggested to pursue the evaluation of both quantities in future studies. CREST factors seem independent of velocity; they provide indications of isolated phenomena and result to be not useful to evaluate vehicle comfort or verify the goodness of the method for the comfort assessment.

The vibrations perceived by riders driving on lumped road irregularities, are the objective of a statistical analysis conducted on a sample of young unexperienced riders. The experimental campaign requires monitoring the vibrations both on vehicle and human body. The root mean square of the acceleration norms has proved to be a suitable parameter to statistically assess vibrations, more than the peak values. A significant influence of driving velocity on the vibration level is generally underlined. Low velocity allows to better highlight differences between subject categories. Gender, dominant limbs and foot position do not relevantly influence the vibration transmissibility. The parameter which mostly influences the vibrations transmitted from vehicle to rider is the human body's mass.

In parallel to the experimental part of the research activity, a multibody model of one of the two electric scooters, the rider and an advanced tyre model has been developed with the aim of accurately describing the system in heavy braking (longitudinal dynamics) and driving on a road characterised by the presence of bumps (vertical dynamics). In the model tuning phase, it is demonstrated that the steering column flexibility relevantly affects the vibrations at the handlebar. Adopting a viscous-elastic bushing instead of an ideal revolute joint in the steering mechanism allows to properly consider this aspect.

As regards the simulation of the braking manoeuvre, the model including a passive rider is able to accurately represent both the vehicle magnitudes and the kinematics of the main human body segments. An optimisation process aiming at minimising the difference between some simulated and experimental signals is followed with the goal of tuning the rider joint response. Preliminary hypotheses are necessary to reduce the size of the optimisation problem. The method proves to be efficient and needs reasonable computational time. It is found that the rider motion, which is a compound combination of the angular motion of upper and lower limb joints, affects the vehicle longitudinal acceleration. Acting on the shoulder is sufficient to control the kinematic of the upper limbs. Even hip and

knee stiffnesses are important to get the correct motion of the rider. In general, it can be concluded that the rider under analysis in this specific manoeuvre behaves as a sort of passive system. It is supposed that the characteristics of the anatomical joints and the associated dynamic response can change performing the same test with different riders and adopting different braking levels.

The simulation of the tests on the road with the bumps reveals that the rider tends to be more rigid at low velocity, probably to maintain the roll equilibrium. At high velocity, the rider seems to be dynamically decoupled with respect to the vehicle. This evidence is probably an instinctive response of the human body to experience a lower level of vibrations. Thus, the rider aims at actively minimising the angular pitching and the vertical bouncing. The pitch equilibrium is mainly obtained by the lower limb joints without the assistance of higher limbs driving at constant velocity, even on small unevennesses.

The presented PhD work intends to be a starting point for a larger research activity aimed at improving the safety and the comfort of electric kick scooters and, generally speaking, electric micro-vehicles for urban mobility. Further investigation on electric kick scooters can lead to:

- the integration of joint actuators and control logics in the rider multibody model able to reproduce the human body response in realistic manoeuvres such as the standing start and driving on uneven roads;
- a better understanding of the role of tyres and suspensions on transmitted vibrations driving electric kick scooters on real roads;
- the extension of the experimental campaign and the multibody model to the lateral dynamics focussing on manoeuvrability and stability;
- a statistical analysis aiming at evaluating the driving behaviour of riders with a fair level of expertise;
- an experimental comparison in terms of comfort with other electric micro-vehicles as e-bikes.

References

[1] S. Boglietti, B. Barabino, G. Maternini, Survey on e-powered micro personal mobility vehicles: Exploring current issues towards future developments, Sustainability. 13 (2021) 3692.

[2] D.J. Reck, H. Martin, K.W. Axhausen, Mode choice, substitution patterns and environmental impacts of shared and personal micro-mobility, Transp Res D Transp Environ. 102 (2022) 103134.

[3] J. Zagorskas, M. Burinskienė, Challenges caused by increased use of e-powered personal mobility vehicles in European cities, Sustainability. 12 (2019) 273.

[4] A.D. Bozzi, A. Aguilera, Shared E-scooters: A review of uses, health and environmental impacts, and policy implications of a new micro-mobility service, Sustainability. 13 (2021) 8676.

[5] L. Butler, T. Yigitcanlar, A. Paz, W. Areed, How can smart mobility bridge the first/last mile gap? Empirical evidence on public attitudes from Australia, J Transp Geogr. 104 (2022) 103452.

[6] V. Štefancová, A. Kalašová, K. Čulík, J. Mazanec, M. Vojtek, J. Mašek, Research on the impact of COVID-19 on micromobility using statistical methods, Applied Sciences. 12 (2022) 8128.

[7] M. Alliance, Guidelines & Recommendations to create the foundations for a thriving MaaS Ecosystem, MaaS Alliance AISBL: Brussels, Belgium. (2017).

[8] A. Kubik, CO2 Emissions of Electric Scooters Used in Shared Mobility Systems, Energies (Basel). 15 (2022) 8188.

[9] A. Kubik, The Energy Consumption of Electric Scooters Used in the Polish Shared Mobility Market, Energies (Basel). 15 (2022) 8193.

[10] H. Moreau, L. de Jamblinne de Meux, V. Zeller, P. D'Ans, C. Ruwet, W.M.J. Achten, Dockless e-scooter: A green solution for mobility? Comparative case study between dockless e-scooters, displaced transport, and personal e-scooters, Sustainability. 12 (2020) 1803.

[11] J. Hollingsworth, B. Copeland, J.X. Johnson, Are e-scooters polluters? The environmental impacts of shared dockless electric scooters, Environmental Research Letters. 14 (2019) 084031.

[12] M.H. Almannaa, H.I. Ashqar, M. Elhenawy, M. Masoud, A. Rakotonirainy, H. Rakha, A comparative analysis of e-scooter and e-bike usage patterns: Findings from the City of Austin, TX, Int J Sustain Transp. 15 (2021) 571–579.

[13] J. Leoni, M. Tanelli, S.C. Strada, S.M. Savaresi, Assessing e-scooters safety and drivability: a quantitative analysis, IFAC-PapersOnLine. 55 (2022) 260–265.

[14] National Association of City Transportation Officials (Nacto), Guidelines for Regulating Shared Micromobility, New York, 2019.

[15] A. Hosseinzadeh, M. Algomaiah, R. Kluger, Z. Li, E-scooters and sustainability: Investigating the relationship between the density of E-scooter trips and characteristics of sustainable urban development, Sustain Cities Soc. 66 (2021) 102624.

[16] H. Badia, E. Jenelius, Shared e-scooter micromobility: review of use patterns, perceptions and environmental impacts, Transp Rev. (2023) 1–27.

[17] A.Y. Chang, L. Miranda-Moreno, R. Clewlow, L. Sun, Trend or fad, Deciphering the Enablers of Micromobility in the US. (2019).

[18] G. McKenzie, Spatiotemporal comparative analysis of scooter-share and bike-share usage patterns in Washington, DC, J Transp Geogr. 78 (2019) 19–28.

[19] C.S. Kopplin, B.M. Brand, Y. Reichenberger, Consumer acceptance of shared e-scooters for urban and short-distance mobility, Transp Res D Transp Environ. 91 (2021) 102680.

[20] F. Mehzabin Tuli, A. Nishita Nithila, S. Mitra, Examining the Impact of the Covid-19 Pandemic on Shared E-Scooter Usage: A Spatial Panel Model, Arna and Mitra, Suman, Examining the Impact of the Covid-19 Pandemic on Shared E-Scooter Usage: A Spatial Panel Model (November 12, 2022). (2022).

[21] D. Li, J. Lasenby, Investigating impacts of COVID-19 on urban mobility and emissions, Cities. (2023) 104246.

[22] G. Dias, E. Arsenio, P. Ribeiro, The role of shared E-Scooter systems in urban sustainability and resilience during the COVID-19 mobility restrictions, Sustainability. 13 (2021) 7084.

[23] D. Glavić, A. Trpković, M. Milenković, S. Jevremović, The e-scooter potential to change urban mobility—Belgrade case study, Sustainability. 13 (2021) 5948.

[24] J. Glenn, M. Bluth, M. Christianson, J. Pressley, A. Taylor, G.S. Macfarlane, R.A. Chaney, Considering the potential health impacts of electric scooters: an analysis of user reported behaviors in Provo, Utah, Int J Environ Res Public Health. 17 (2020) 6344.

[25] B. Şengül, H. Mostofi, Impacts of E-Micromobility on the sustainability of urban transportation—a systematic review, Applied Sciences. 11 (2021) 5851.

[26] K. Kazemzadeh, M. Haghani, F. Sprei, Electric scooter safety: An integrative review of evidence from transport and medical research domains, Sustain Cities Soc. (2022) 104313.

[27] F.W. Siebert, M. Ringhand, F. Englert, M. Hoffknecht, T. Edwards, M. Rötting, Braking bad–Ergonomic design and implications for the safe use of shared E-scooters, Saf Sci. 140 (2021) 105294.

[28] K.-J. Lee, C.H. Yun, M.H. Yun, Contextual risk factors in the use of electric kick scooters: an episode sampling inquiry, Saf Sci. 139 (2021) 105233.

[29] J. Todd, D. Krauss, J. Zimmermann, A. Dunning, Behavior of electric scooter operators in naturalistic environments, SAE Technical Paper, 2019.

[30] A. Badeau, C. Carman, M. Newman, J. Steenblik, M. Carlson, T. Madsen, Emergency department visits for electric scooter-related injuries after introduction of an urban rental program, Am J Emerg Med. 37 (2019) 1531–1533.

[31] M. Aizpuru, K.X. Farley, J.C. Rojas, R.S. Crawford, T.J. Moore Jr, E.R. Wagner, Motorized scooter injuries in the era of scooter-shares: a review of the national electronic surveillance system, Am J Emerg Med. 37 (2019) 1133–1138.

[32] G. la Torre, E. van Beeck, G. Bertazzoni, W. Ricciardi, Head injury resulting from scooter accidents in Rome: differences before and after implementing a universal helmet law, Eur J Public Health. 17 (2007) 607–611.

[33] A. Badeau, C. Carman, M. Newman, J. Steenblik, M. Carlson, T. Madsen, Emergency department visits for electric scooter-related injuries after introduction of an urban rental program, Am J Emerg Med. 37 (2019) 1531–1533.

[34] T. Scquizzato, L. Gamberini, F. Stella, A. Paoli, A. Gazzato, A. Forti, F. Semeraro, Analysis of road traffic accidents involving standing electric scooters reported in newspapers in Italy, Clin Exp Emerg Med. 9 (2022) 36.

[35] O. Lavoie-Gagne, M. Siow, W. Harkin, A.R. Flores, P.J. Girard, A.K. Schwartz, W.T. Kent, Characterization of electric scooter injuries over 27 months at an urban level 1 trauma center, Am J Emerg Med. 45 (2021) 129–136.

[36] M.N.Z. Bekhit, J. le Fevre, C.J. Bergin, Regional healthcare costs and burden of injury associated with electric scooters, Injury. 51 (2020) 271–277.

[37] N.K. Namiri, H. Lui, T. Tangney, I.E. Allen, A.J. Cohen, B.N. Breyer, Electric scooter injuries and hospital admissions in the United States, 2014-2018, JAMA Surg. 155 (2020) 357–359.

[38] J.B. Cicchino, P.E. Kulie, M.L. McCarthy, Severity of e-scooter rider injuries associated with trip characteristics, J Safety Res. 76 (2021) 256–261.

[39] T.K. Trivedi, C. Liu, A.L.M. Antonio, N. Wheaton, V. Kreger, A. Yap, D. Schriger, J.G. Elmore, Injuries associated with standing electric scooter use, JAMA Netw Open. 2 (2019) e187381–e187381.

[40] T.J. Puzio, P.B. Murphy, J. Gazzetta, H.A. Dineen, S.A. Savage, E.W. Streib, B.L. Zarzaur, The electric scooter: a surging new mode of transportation that comes with risk to riders, Traffic Inj Prev. 21 (2020) 175–178.

[41] British Standard, Light motorized vehicles for the transportation of persons and goods and related facilities and not subject to type-approval for onroad use - Personal light electric vehicles (PLEV) - Requirements and test methods, BS EN 1728:2020, 2020.

[42] A. Santacreu, G. Yannis, O. de Saint Leon, P. Crist, Safe micromobility, (2020).

[43] C.M.R. Garman, S.G. Como, I.C. Campbell, J. Wishart, K. O'Brien, S. McLean, Micro-mobility vehicle dynamics and rider kinematics during electric scooter riding, SAE Technical Paper, 2020.

[44] P. Brunner, A. Löcken, F. Denk, R. Kates, W. Huber, Analysis of experimental data on dynamics and behavior of e-scooter riders and applications to the impact of automated driving functions on urban road safety, in: 2020 IEEE Intelligent Vehicles Symposium (IV), IEEE, 2020: pp. 219–225.

[45] M. Paudel, F. Fah Yap, Front steering design guidelines formulation for e-scooters considering the influence of sitting and standing riders on self-stability and safety performance, Proceedings of the Institution of Mechanical Engineers, Part D: Journal of Automobile Engineering. 235 (2021) 2551–2567.

[46] M. Paudel, An investigation into the design for rideability of small wheel single-track bicycles and e-scooters, Nanyang Tecnological University, 2019.

[47] Q. Ma, H. Yang, A. Mayhue, Y. Sun, Z. Huang, Y. Ma, E-Scooter safety: The riding risk analysis based on mobile sensing data, Accid Anal Prev. 151 (2021) 105954.

[48] J.D. Cano-Moreno, M.E. Islán, F. Blaya, R. D'Amato, J.A. Juanes, E. Soriano, E-scooter vibration impact on driver comfort and health, Journal of Vibration Engineering & Technologies. (2021) 1–15.

[49] J.D. Cano-Moreno, J.M. Cabanellas Becerra, J.M. Arenas Reina, M.E. Islán Marcos, Analysis of e-scooter vibrations risks for riding comfort based on real measurements, Machines. 10 (2022) 688.

[50] S. Boglietti, A. Ghirardi, C.T. Zanoni, R. Ventura, B. Barabino, G. Maternini, D. Vetturi, First experimental comparison between e-kick scooters and e-bike's vibrational dynamics, Transportation Research Procedia. 62 (2022) 743–751.

[51] M. Asperti, M. Vignati, F. Braghin, Modeling of the Vertical Dynamics of a Kick e-Scooter on Distributed Road Irregularity, in: Advances in Dynamics of Vehicles on Roads and Tracks II: Proceedings of the 27th Symposium of the International Association of Vehicle System Dynamics, IAVSD 2021, August 17–19, 2021, Saint Petersburg, Russia, Springer, 2022: pp. 1070–1080.

[52] M. Asperti, M. Vignati, F. Braghin, Modelling of the vertical dynamics of an electric kick scooter, IEEE Transactions on Intelligent Transportation Systems. 23 (2021) 9266–9274.

[53] E. Arslan, Ç. Uyulan, Analysis of an e-scooter and rider system dynamic response to curb traversing through physics-informed machine learning methods, Proceedings of the Institution of Mechanical Engineers, Part D: Journal of Automobile Engineering. (2022).

[54] S. Michelangelo-Gulino, G. Vichi, G. Zonfrillo, D. Vangi, Comfort assessment for electric kick scooter decks, in: IOP Conf Ser Mater Sci Eng, IOP Publishing, 2022: p. 012043.

[55] C. Schedlinski, M. Link, A survey of current inertia parameter identification methods, Mech Syst Signal Process. 15 (2001) 189–211.

[56] A.D. Vella, A. Vigliani, Research on the Longitudinal Dynamics of an Electric Scooter, SAE Int J Veh Dyn Stab NVH. 7 (2022) 35–51.

[57] G. Bishop, G. Welch, An introduction to the kalman filter, Proc of SIGGRAPH, Course. 8 (2001) 41.

[58] R.E. Kalman, A new approach to linear filtering and prediction problems, (1960).

[59] H. Pacejka, Tire and vehicle dynamics, Elsevier, 2005.

[60] S. Acarer, E. Arslan, Ç. Uyulan, Aerodynamic investigation of an e-scooter and rider system through computational fluid dynamics approach, in: 10th International Automotive Technologies Congress, 2020.

[61] A.J. Day, D. Bryant, Braking of road vehicles, Butterworth-Heinemann, 2022.

[62] International Standard, Mechanical vibration and shock - Evaluation of human exposure to whole-body vibration - Part 1: General Requirements, BS ISO 2631-1:1997, (1997).

[63] International Standard, Mechanical vibration - Measurement and evaluation of human exposure to hand-transmitted vibration - Part 1: General requirements, BS EN ISO 5349-1:2001, (2001).

[64] International Standard, Mechanical vibration and shock - Evaluation of human exposure to whole-body vibration - Part 5: Method for evaluation of vibration containing multiple shocks, ISO 2631-5:2018-07, (2018).

[65] S.S. Sawilowsky, Nonparametric tests of interaction in experimental design, Rev Educ Res. 60 (1990) 91–126.

[66] D.W. Zimmerman, B.D. Zumbo, Relative power of the Wilcoxon test, the Friedman test, and repeated-measures ANOVA on ranks, The Journal of Experimental Education. 62 (1993) 75–86.

[67] D.G. Pereira, A. Afonso, F.M. Medeiros, Overview of Friedman's test and post-hoc analysis, Communications in Statistics-Simulation and Computation. 44 (2015) 2636–2653.

[68] J. Cuzick, A Wilcoxon-type test for trend, Stat Med. 4 (1985) 87–90.

[69] P.E. McKnight, J. Najab, Mann-Whitney U Test, The Corsini Encyclopedia of Psychology. (2010) 1.

[70] V. Cossalter, R. Lot, M. Massaro, An advanced multibody code for handling and stability analysis of motorcycles, Meccanica. 46 (2011) 943–958.

[71] S. Zhu, S. Murakami, H. Nishimura, Motion analysis of a motorcycle taking into account the rider's effects, Vehicle System Dynamics. 50 (2012) 1225–1245.

[72] A. Doria, M. Tognazzo, V. Cossalter, The response of the rider's body to roll oscillations of two wheeled vehicles; experimental tests and biomechanical models, Proceedings of the Institution of Mechanical Engineers, Part D: Journal of Automobile Engineering. 227 (2013) 561–576.

[73] G. Sequenzia, S.M. Oliveri, G. Fatuzzo, M. Calì, An advanced multibody model for evaluating rider's influence on motorcycle dynamics, Proceedings of the Institution of Mechanical Engineers, Part K: Journal of Multi-Body Dynamics. 229 (2015) 193–207.

[74] R. Barbagallo, G. Sequenzia, S.M. Oliveri, A. Cammarata, Dynamics of a high-performance motorcycle by an advanced multibody/control co-simulation, Proceedings of the Institution of Mechanical Engineers, Part K: Journal of Multi-Body Dynamics. 230 (2016) 207–221.

[75] V.E. Bulsink, A. Doria, D. van de Belt, B. Koopman, The effect of tyre and rider properties on the stability of a bicycle, Advances in Mechanical Engineering. 7 (2015) 1687814015622596.

[76] P. Lugner, H. Pacejka, M. Plöchl, Recent advances in tyre models and testing procedures, Vehicle System Dynamics. 43 (2005) 413–426.

[77] A. Eichberger, M. Schittenhelm, Implementations, applications and limits of tyre models in multibody simulation, Vehicle System Dynamics. 43 (2005) 18–29.

[78] M. Gipser, FTire: a physically based application-oriented tyre model for use with detailed MBS and finite-element suspension models, Vehicle System Dynamics. 43 (2005) 76–91.

[79] C. Oertel, Ride comfort simulations and steps towards life time calculations RMOD-K tyre model and ADAMS, in: International ADAMS Users' Conference, Berlin, 1999, 1999.

[80] A.J.C. Schmeitz, I.J.M. Besselink, S.T.H. Jansen, Tno mf-swift, Vehicle System Dynamics. 45 (2007) 121–137.

[81] A.J.C. Schmeitz, S.T.H. Jansen, H.B. Pacejka, J.C. Davis, N.N. Kota, C.G. Liang, G. Lodewijks, Application of a semi-empirical dynamic tyre model for rolling over arbitrary road profiles, International Journal of Vehicle Design. 36 (2004) 194–215.

[82] Siemens Digital Industries Software, MF-Tyre/MF-Swift User Manual Version 2021.1, 2021.

[83] S. Kitazaki, M.J. Griffin, Resonance behaviour of the seated human body and effects of posture, J Biomech. 31 (1997) 143–149.

[84] N. Bourdet, R. Willinger, Coupled head–neck–torso and seat model for car seat optimization under rear-end impact, J Sound Vib. 313 (2008) 891–907.

[85] F. Ruoxun, L. Jie, L. Jun, W. Weijun, Presentation of an approach on determination of the natural frequency of human lumbar spine using dynamic finite element analysis, Appl Bionics Biomech. 2019 (2019).

[86] R. Meijer, E. Van Hassel, J. Broos, H. Elrofai, L. Van Rooij, P. Van Hooijdonk, Development of a multi-body human model that predicts active and passive human behaviour, in: Proceedings of the International Conference on Biomechanics of Impact Ircobi, Dublin-Ireland, 2012: pp. 622–636.

[87] M. Bova, M. Massaro, N. Petrone, A three-dimensional parametric biomechanical rider model for multibody applications, Applied Sciences. 10 (2020) 4509.

[88] H. Imaizumi, T. Fujioka, M. Omae, Rider model by use of multibody dynamics analysis, JSAE Review. 17 (1996) 75–77.

[89] G. Wu, S. Siegler, P. Allard, C. Kirtley, A. Leardini, D. Rosenbaum, M. Whittle, D. D D'Lima, L. Cristofolini, H. Witte, ISB recommendation on definitions of joint coordinate system of various joints for the reporting of human joint motion—part I: ankle, hip, and spine, J Biomech. 35 (2002) 543–548.

[90] G. Wu, F.C.T. van der Helm, H.E.J.D. Veeger, M. Makhsous, P. van Roy, C. Anglin, J. Nagels, A.R. Karduna, K. McQuade, X. Wang, ISB recommendation on definitions of joint coordinate systems of various joints for the reporting of human joint motion—Part II: shoulder, elbow, wrist and hand, J Biomech. 38 (2005) 981–992.

[91] W.R. Santschi, J. Dubois, C. Omoto, Moments of inertia and centers of gravity of the living human body, NORTH AMERICAN AVIATION INC LOS ANGELES CA, Los Angeles, 1963.

[92] J.G. Hay, Moment of inertia of the human body, Kinesiology IV. 4 (1974) 43–52.

[93] A. Schmeitz, W. Versteden, T. Eguchi, Road load simulation using the mf-swift tire and OpenCRG road model, SAE Technical Paper, 2011.

[94] Association for Standardization of Automation and Measuring Systems, OpenCRG, (2020). www.asam.net/standards/detail/opencrg/ (accessed February 14, 2023).

[95] E. Bakkar, L. Nyborg, H.B. Pacejka, A new tyre model with an application in vehicle dynamic studies, SAE Trans.: Jrnl. of Passenger Cars. 98 (1989).

[96] E. Bakker, L. Nyborg, H.B. Pacejka, Tyre modelling for use in vehicle dynamics studies, SAE Transactions. (1987) 190–204.

[97] H.B. Pacejka, E. Bakker, The magic formula tyre model, Vehicle System Dynamics. 21 (1992) 1–18.

[98] H.B. Pacejka, I.J.M. Besselink, Magic formula tyre model with transient properties, Vehicle System Dynamics. 27 (1997) 234–249.

[99] I.J.M. Besselink, A.J.C. Schmeitz, H.B. Pacejka, An improved Magic Formula/Swift tyre model that can handle inflation pressure changes, Vehicle System Dynamics. 48 (2010) 337–352.

[100] P.W.A. Zegelaar, The dynamic response of tyres to brake torque variations and road unevennesses, PhD Thesis TU Delft. (1998).

[101] P.W.A. Zegelaar, H.B. Pacejka, The in-plane dynamics of tyres on uneven roads, Vehicle System Dynamics. 25 (1996) 714–730.

[102] J.P. Maurice, P.W.A. Zegelaar, H.B. Pacejka, The influence of belt dynamics on cornering and braking properties of tyres, Vehicle System Dynamics. 29 (1998) 299–311.

[103] J.P. Maurice, Short wavelength and dynamic tyre behaviour under lateral and combined slip conditions, PhD Thesis TU Delft. (2000).

[104] A.J.C. Schmeitz, A semi-empirical three-dimensional model of the pneumatic tyre rolling over arbitrarily uneven road surfaces., PhD Thesis TU Delft. (2004).

[105] TNO Automotive, MF-Tyre/MF-Swift 6.1.2 Manual, 2010.

[106] A.J.C. Schmeitz, I.J.M. Besselink, J. de Hoogh, H. Nijmeijer, Extending the Magic Formula and SWIFT tyre models for inflation pressure changes, Vdi Berichte. 1912 (2005) 201.

Appendices

Appendix A - Sensor characteristics

In this appendix the electronic devices used during the experimental campaign are listed and discussed.

Siemens SCADAS XS

Siemens SCADAS XS is the acquisition system used in all the on-road tests conducted within this research work. The device can work in three different modalities:

- the frontend mode, i.e., connected to the PC via USB or via LAN;
- the tablet mode, i.e., remotely controlled by a tablet connected via Wi-Fi;
- the standalone mode, i.e., using a preconfigured measurement template.

In particular, the tablet mode is used in the experimental tests related to the longitudinal dynamics (Chapter 3) and the standalone mode in the experimental tests related to the vertical dynamics (Chapter 4 and Chapter 5). In both the cases, the measurement template is preliminarily created in Simcenter Testlab Scope app of the tablet. The acquired signals are stored into a Micro SD card within the acquisition system and exported after the testing sessions. LMS Test.Lab Recorder Data Conversion toll is used to convert the data in Matlab format in order to be processed. Figure 104 represents the acquisition system and the measuring input ports.

Figure 104 - Siemens SCADAS XS

In the following, the input ports involved in the experimental campaigns are described.

- Four LEMO ports are dedicated to the acquisition of the analogue signals. Each port is able to read three ± 10 V inputs. They are used to connect the four IEPE accelerometers (three analogue channel each). SCADAS XS manages TEDS sensors: the characteristics of the accelerometers are automatically read without the user's intervention. The input range, i.e., the maximum acceleration which can be measured by the system, is set to 30 g for all the LEMO ports. This setting is used to optimise the measuring scale and to increase the signal accuracy. The acquisition frequency of these ports is set to 3200 Hz.
- TACHO port requires a ± 10 V signal as input signal. It is used to acquire and compute the wheel angular velocities. To do so, the pulse per revolution as well the trigger level for the detection of the voltage wave must be assigned. The output frequency follows LEMO setting while the acquisition frequency is automatically set by the acquisition system.
- GNSS port is used to connect the antenna. Starting from the latitude and longitude, the system computes an estimation of the velocity

components (northwards, eastwards and upwards). The GNSS acquisition frequency is 4 Hz and cannot be modified.

- CAN port is used to acquire signals transmitted via CAN protocol. The acquisition system needs the baud rate, i.e., the data transmission rate, and the database to decipher the data packs. The sampling rate is determined by the connected sensor.

All the acquisitions are conducted in free-run mode, i.e., the user has to manually start and stop the recording.

SBG Ellipse A

SBG Ellipse is a MEMS (micro-electro-mechanical system) sensor belonging to SBG series of AHRS[2]. Version A, which is used in in the experimental campaigns to monitor the e-scooter dynamics, includes a three-axis gyroscope, a three-axis accelerometers and a three-axis magnetometer. Figure 105 shows the operation diagram of the sensors belonging to SBG Ellipse series. Green ticks underline the characteristics included in SBG Ellipse A.

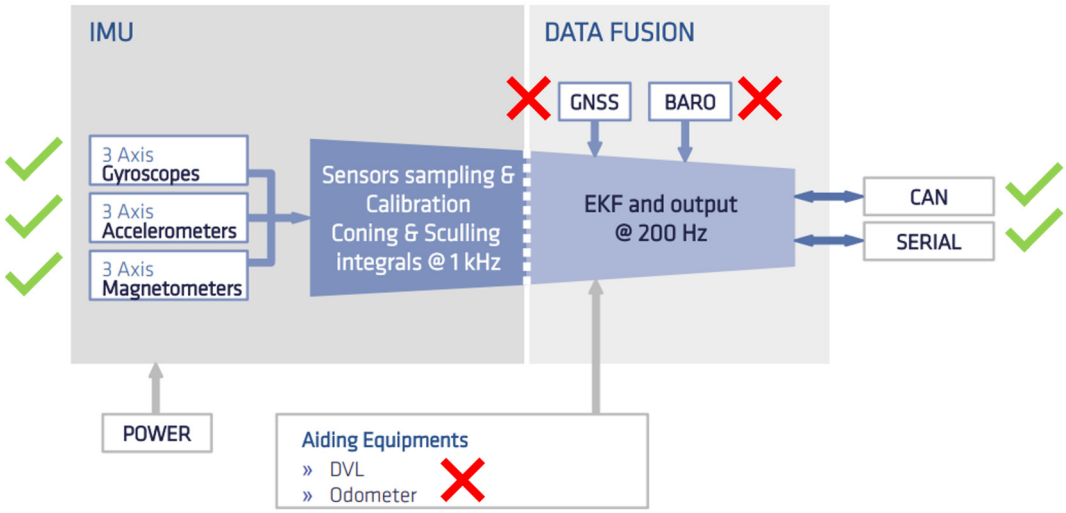

Figure 105 - SBG Ellipse sensor operation diagram

[2] Inertial Measurement Unit (IMU): sensor constituted by a 3-axis accelerometer and a 3-axis gyroscope.

Attitude Heading Reference System (AHRS): sensor constituted by an IMU and a 3-axis magnetometer.

Inertial Navigations System (INS): sensor constituted by an AHRS and a Global Navigation Satellite System (GNSS).

Figure 106 represents the main dimensions of the sensor and the position of the reference measurement frame.

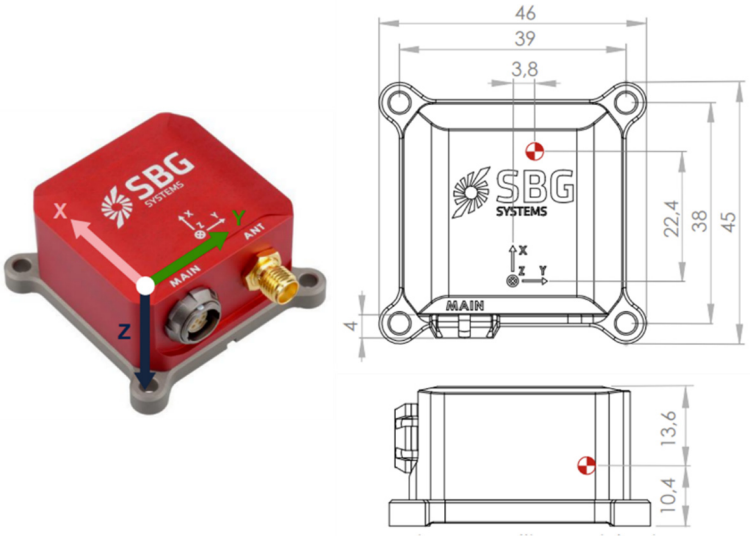

Figure 106 - SBG Ellipse A dimensions and measurement frame

The main technical specifications of the sensor are reported in Table 58.

Table 58 - Technical specifications of SBG Ellipse A

Magnitude	**Accelerometer**	**Gyroscope**	**Magnetometer**
Sampling rate	4 kHz	10 kHz	100 Hz
Bandwidth	390 Hz	133 Hz	22 Hz
Full scale	16 g	450 °/s	50 Gauss

The mass of the sensor is of 0.045 kg. Output signals are provided at the frequency of 200 Hz. The power consumption at 12 V is equal to 250 mW and the powering voltage must be between 5 V and 36 V. In the experimental campaigns, the sensor is powered with a LiPo battery. SBG Ellipse A is configured connecting the RS-232 serial port to the PC and using sbgCentre tool. During the experimental tests, the sensor is connected to the acquisition system by CAN 2.0A connection at a rate equal to 10^6 baud. One end of the CAN cable

includes the sensor connector while the other end is open: it is used for the signal acquisitions and the sensor powering. Figure 107 represents the connection scheme.

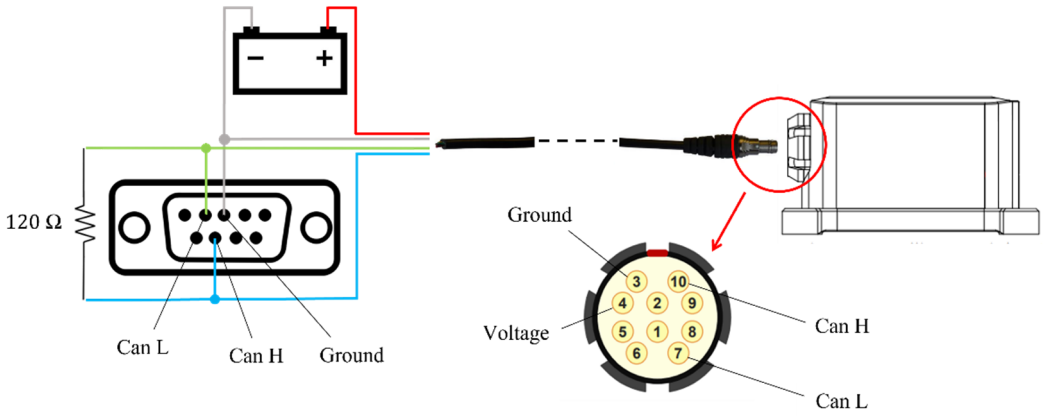

Figure 107 - SBG Ellipse A connection scheme

Accelerometers

Four IEPE Kistler accelerometers are used in the experimental analyses to acquire the vibrations in correspondence of the e-scooter wheels, the deck and the handlebar. The model number is 8766A050BTH. The accelerometer case consists of a titanium cube whose mass is equal to 0.01 kg. The main dimensions and the reference measurement frame are represented in Figure 108.

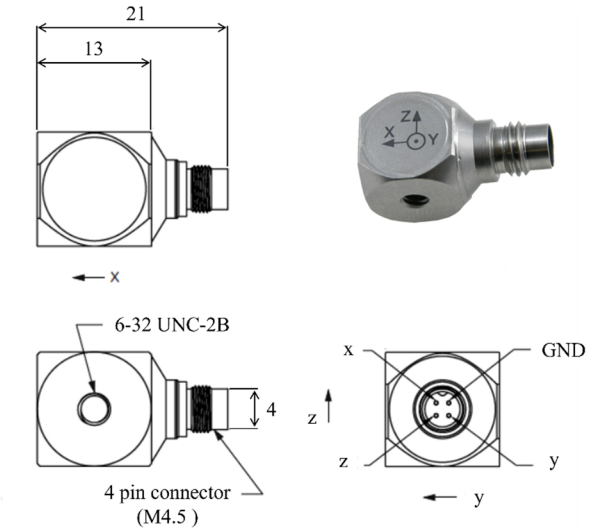

Figure 108 - Dimensions of the accelerometers and measurement frame

The technical specifications of the accelerometers are reported in Table 59.

Table 59 - Technical specifications of Kistler accelerometers

Acceleration range	± 50 g
Acceleration limit	± 100 g
Sensitivity at 100 Hz	100 mV/g
Resonant frequency	> 20 kHz
Linear frequency response ($\pm 5\%$)	$1 - 5000$ Hz

The four sensors are TEDS, i.e., their datasheet is memorised within the transducer and automatically read by the acquisition system.

Tachometer

Gebildet LJ12A3-4-Z proximity sensor is readapted as tachometer. It is originally designed for the detection of metallic objects at a distance smaller than 4 mm from the sensor head. It must be powered by a direct current in the voltage range between 6 and 36 V. In the experimental campaigns, the sensor is powered with a LiPo battery. Figure 109 represents the proximity sensor and its circuit.

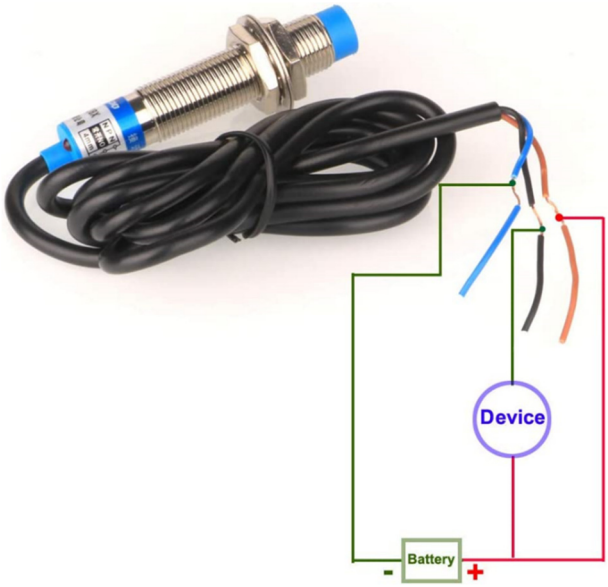

Figure 109 - Gebildet LJ12A3-4-Z proximity sensor and its operating circuit

Red and blue wires are connected to the positive and negative poles of the battery. The measure is performed between black and red wires. The circuit is normally open (no object detected): it is measured a voltage equal to 0 V. If a metal object is close to the sensor head, the voltage of the battery is measured. The proximity sensor is clamped to the e-scooters frame by some support brackets while some bolts fixed on the wheel spokes are used as trigger. Figure 110 represents the experimental setup related to the tachometer on Xiaomi Pro II and Aprilia ESR2.

Figure 110 - Proximity sensor mounted on the rear wheel of Xiaomi Pro II and on the front wheel of Aprilia ESR2

Battery

The LiPo battery used in the experimental tests is reported in Figure 111.

Figure 111 - LiPo battery

It is used to power SBG Ellipse A and the tachometer sensor and consists of a lithium polymer (LiPo) battery. The main characteristics are reported in Table 60.

Table 60 - Specifications of the battery

Model	50C reactionDYNB3800
Voltage	7.4 V
Capacity	4000 mAh (29.6 Wh)
Maximum charge rate	3C
Maximum discharge rate	50C

Opal APDM system

The inertial system Opal APDM consists in five wireless wearable units which include a tri-axial accelerometer, a tri-axial gyroscope, and a tri-axial magnetometer. Each sensor is equipped with a velcro strip to be fastened on a human body segment. The communication between the sensors and the PC is via Bluetooth. The proprietary acquisition software is Motion Studio. Figure 112 represent the entire Opal APDM system.

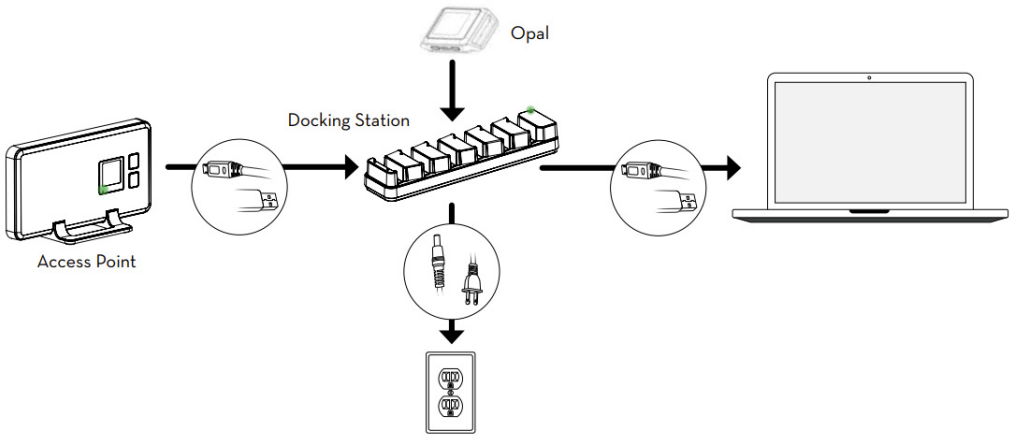

Figure 112 - OPAL APDM system

Figure 113 represents a single Opal unit with its reference system.

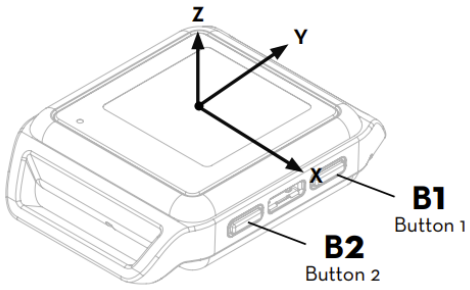

Figure 113 - Opal unit and its reference system

The main technical specifications of each sensor are reported in Table 61.

Table 61 - Technical specifications of OPAL APDM units.

Magnitude	**Accelerometer**	**Gyroscope**	**Magnetometer**
Sampling rate	200 Hz	200 Hz	200 Hz
Bandwidth	50 Hz	50 Hz	32.5 Hz
Full scale	200 g	2000 °/s	8 Gauss

Appendix B – Kalman filter algorithm for vehicle speed estimation

This Appendix is focused on the Kalman filter algorithm [57,58]: it is used to estimate the vehicle velocity starting from GNSS data and the longitudinal acceleration in the experimental tests carried out for the longitudinal dynamics investigation (Chapter 3). A generic problem in the State Space can be written according to Sys. (51). Terms in Sys. (51) are defined in Table 62.

$$\begin{cases} \dot{\boldsymbol{q}} = \boldsymbol{A}\boldsymbol{q} + \boldsymbol{B}\boldsymbol{u} + \boldsymbol{w} \\ \boldsymbol{p} = \boldsymbol{C}\boldsymbol{q} + \boldsymbol{D}\boldsymbol{u} + \boldsymbol{v} \end{cases} \tag{51}$$

Table 62 - Vectors and matrices of the state space problem

Symbol	Definition	Dimension
$\boldsymbol{q}$	State vector	q × 1
$\boldsymbol{u}$	Control input vector	u × 1
$\boldsymbol{p}$	Measurement vector	p × 1
$\boldsymbol{w}$	Process noise	w × 1
$\boldsymbol{v}$	Measurement noise	v × 1
$\boldsymbol{A}$	State matrix	q × q
$\boldsymbol{B}$	Input matrix	q × u
$\boldsymbol{C}$	Output matrix	p × q
$\boldsymbol{D}$	Direct transmission matrix	p × u

Table 63 reports the Kalman filter magnitudes used in the data processing discussed in Chapter 3.

Table 63 - Kalman filter vectors and matrices applied to the experimental data

$\boldsymbol{A}$	$\begin{bmatrix} 0 & 1 & 0 \\ 0 & 0 & 1 \\ 0 & 0 & 0 \end{bmatrix}$
$\boldsymbol{C}$	$\begin{bmatrix} 1 & 0 & 0 \\ 0 & 1 & 0 \\ 0 & 0 & 1 \end{bmatrix}$
$\boldsymbol{q}$	$[x \quad \dot{x} \quad \ddot{x}]^T$
$\boldsymbol{p}$	$[x_G \quad \dot{x}_G \quad \ddot{x}_S]^T$
$\boldsymbol{w}$	$[10^{-4} \quad 10^{-3} \quad 10^{-4}]^T$
$\boldsymbol{v}$	$[10^{-4} \quad 10^{3} \quad 10^{-4}]^T$

Vectors $\boldsymbol{w}$ and $\boldsymbol{v}$ are generally identified in the filter tuning phase. Since in the current analysis the velocity is not directly measured, $\boldsymbol{w}$ and $\boldsymbol{v}$ are assigned to reduce the delay between the estimated velocity and the acceleration. Discretising Sys. (51) and including the magnitudes reported in Table 63, the state space problem can be rewritten according to Sys. (52),

$$\begin{cases} \dot{\boldsymbol{q}}_{k+1} = \boldsymbol{A}_d \boldsymbol{q}_k + \boldsymbol{w}_k \\ \boldsymbol{p}_k = \boldsymbol{C}\boldsymbol{q}_k + \boldsymbol{v} \end{cases} \tag{52}$$

where k is the time counter and Δt is the time step.

$$\boldsymbol{A}_d = \boldsymbol{A}\Delta t + \boldsymbol{I} \tag{53}$$

Matrices $\boldsymbol{Q}$ and $\boldsymbol{R}$ are built from vectors $\boldsymbol{w}$ and $\boldsymbol{v}$.

$$\boldsymbol{Q} = \begin{bmatrix} w_1 & & \\ & w_2 & \\ & & w_3 \end{bmatrix} \qquad \boldsymbol{R} = \begin{bmatrix} v_1 & & \\ & v_2 & \\ & & v_3 \end{bmatrix}$$

(54)

The Kalman filter algorithm consists of five equations to be solved for each time step. The set of two equations in Sys. (55) represents the prediction phase (*a priori* estimation). The set of three equations in Sys. (56) represents the measurement updating phase (*a posteriori* estimation). ($\bar{}$) symbol indicates the *a priori* estimated quantities.

$$\begin{cases} \bar{\boldsymbol{q}}_k = \boldsymbol{A}_d \boldsymbol{q}_{k-1} \\ \bar{\boldsymbol{P}}_k = \boldsymbol{A}_d \boldsymbol{P}_{k-1} \boldsymbol{A}_d^T + Q \end{cases}$$

(55)

$$\begin{cases} \boldsymbol{K}_k = \bar{\boldsymbol{P}}_k \boldsymbol{C}^T (\boldsymbol{C} \bar{\boldsymbol{P}}_k \boldsymbol{C}^T + \boldsymbol{R})^{-1} \\ \boldsymbol{q}_k = \boldsymbol{K}_k (\boldsymbol{p}_k - \boldsymbol{C} \bar{\boldsymbol{q}}_k) \\ \boldsymbol{P}_k = (\boldsymbol{I} - \boldsymbol{K}_k \boldsymbol{C}) \bar{\boldsymbol{P}}_k \end{cases}$$

(56)

Figure 114 represents the comparison between three estimations of the vehicle velocity performed by:

- the acquisition system starting from the GNSS data (blue line);
- the wheel angular velocity measured by the tachometer, which is available in the experimental tests discussed in Chapter 4 and Chapter 5 (black line);
- the Kalman filter algorithm starting from GNSS data and the longitudinal acceleration (red line).

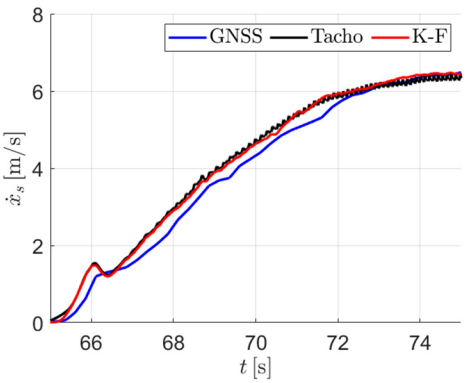

Figure 114 - Velocity comparison

As evident in Figure 114, the Kalman filter estimation is in line with the velocity computed from tachometer signal, which is considered a reliable reference. A significant delay between the tachometer estimation and the velocity computed by the acquisition system starting from GNSS information is detected (0.2 s on average, which corresponds roughly to the acquisition time of the GNSS).

Appendix C - MF-Tyre/MF-Swift mode

In this appendix, an historical overview of Pacejka tyre model is given first. Then, the main MF-Tyre/MF-Swift settings in the Simscape mask are explained.

Overview of Pacejka tyre model

Pacejka Magic Formula was presented for the first time in 1987 as a semi-empirical model able to reproduce tyre forces and moments in steady-state conditions for handling applications [95–97]. Relaxation length and combined slip were introduced in [98], taking into account transient response of the tyre up to 8 Hz. Figure 115 represents the convention of forces $F_{x/y/z}$ and moments $M_{x/y/z}$ exerted by the tyre on the ground in the contact point C while Figure 116 represents the inputs and the outputs of the model.

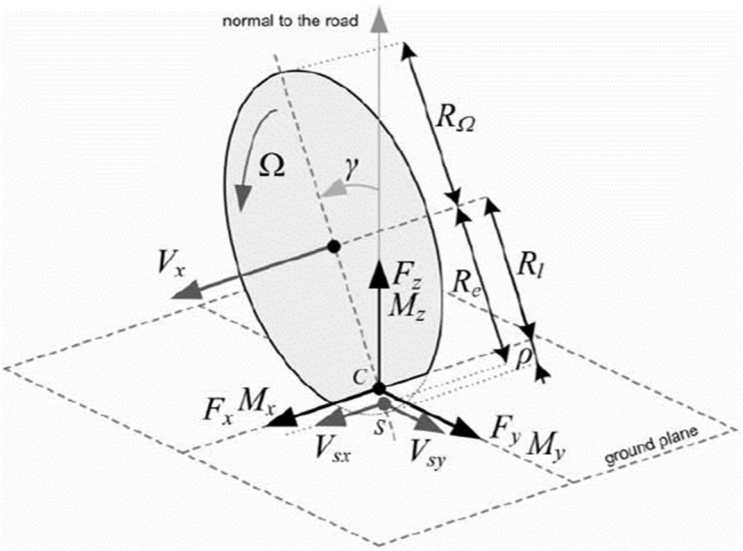

Figure 115 - ISO convention for tyre variables [99]

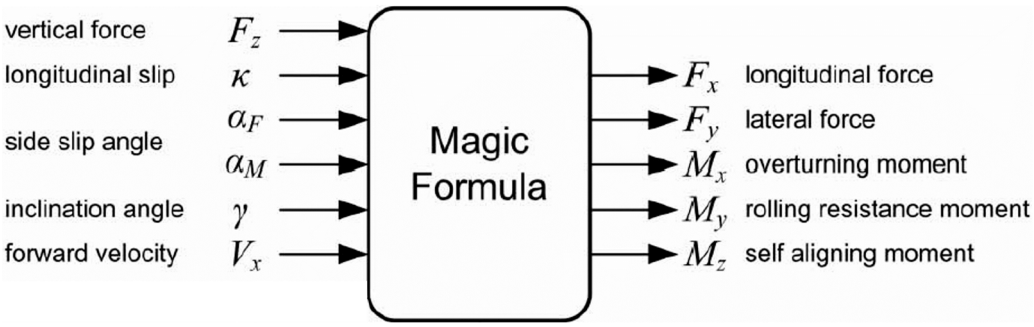

Figure 116 - Inputs and outputs of MF-Tyre model [99]

The interest in tyre-uneven road interaction came from the need to develop active control systems in traction, braking and turning manoeuvres, considering frequencies up to 30 Hz. At Delft University of Technology, the research work conducted by three PhD students under the supervision of Professor Pacejka brought to the development of a rigid ring tyre model called SWIFT (Short Wavelength Intermediate Frequency Tyre) able to represent relatively high frequency phenomena under pure and combined slip conditions. In-plane and out-of-plane tyre behaviours are respectively studied by Zegelaar [100,101] and Maurice [102,103]. The interaction between the tyre model and a 3D road is studied by Schmeitz [104]. The method developed by Schmeitz is based on a grid of elliptical cams able to calculate an equivalent vertical elevation of the road averaging at the contact patch in the longitudinal and transverse direction. Figure 117 represents a longitudinal tandem of two cams able to identify a road bump and compute an equivalent road profile.

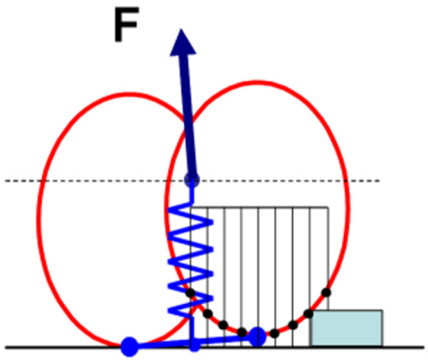

Figure 117 - Sketch of a cam tandem for the computation of an equivalent road profile [105]

In 2005, Besselink and Schmeitz [99] presented the new version of the tyre model called MF-Tyre/MF-Swift 6.1 and its improvements with respect to the

previous version, TNO MF-Tyre 5.2. The modifications dealt with the formulation in large camber angle condition, the rolling resistance, the air pressure influence on the tyre parameters [106] and the enveloping properties. Moreover, rigid ring model became consistent with the simple first order relaxation length formulation adding residual stiffnesses. Combining the rigid ring tyre model and the road enveloping method in the so-called MF-Swift, the tyre model became able to assess ride comfort and durability, the frequency range was extended up to 100 Hz and short wavelength road unevennesses were considered. Figure 118 represents a sketch of the new rigid ring tyre model.

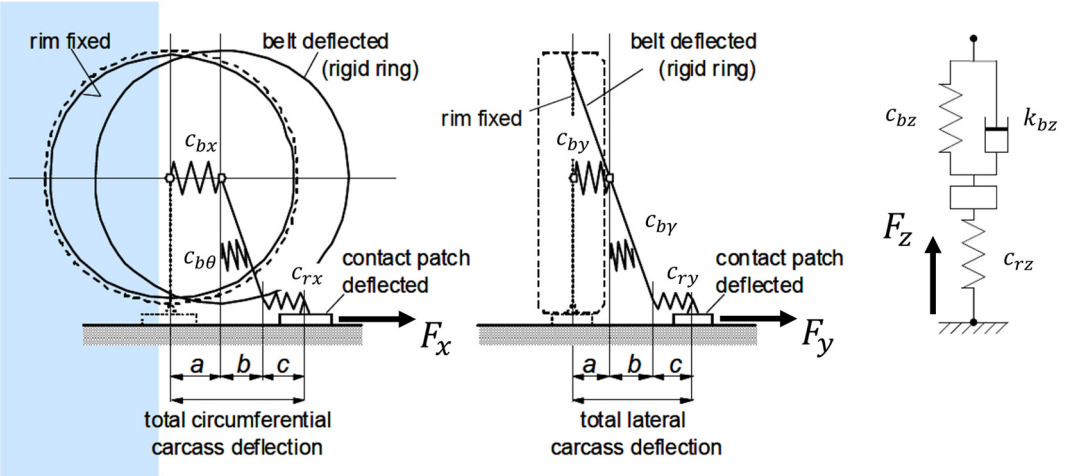

Figure 118 - Sketch of the rigid ring model [105]

In 2017 MF-Tyre/MF-Swift became a Siemens product after the acquisition of TASS International including TNO/TASS Delft-Tyre portfolio [82]. MF-Tyre model together with the first version of MF-Swift extension has been commercially available in Matlab/Simulink since 2000.

MF-Tyre/MF-Swift settings

Table 64 - MF-Tyre/MF-Swift parameters and options

Parameters	Options
Rim inertias $[m \quad J_x \quad J_y]$	
Tyre property file name (.tir)	
Tyre side	Left Right Symmetric Mirror
Road method	Flat Opencrg External
Road name (.crg)	
Contact method	Smooth road Moving road Enveloping
Dynamics	Steady-state Relaxation behaviour Non-linear relaxation behaviour Rigid-ring
Slip forces	None Longitudinal Lateral Uncombined Combined Combined and turnslip

Table 64 reports the MF-Tyre/MF-Swift mask in Simscape. Temperature and velocity options are not mentioned since they are not used in the current analyses.

- The “Rim inertias” are the rim mass and moments of inertias (diametral and polar).
- The “Tyre property file name” is a text string containing the name of the file which stores the fundamental set of tyre parameters.
- The “Tyre side” refers to the asymmetric behaviour, typical of tyres belonging to four-wheeled vehicle, due to conicity and plies. It must be specified if the tyre is mounted at the left, at the right or if the asymmetries must be neglected.
- The “Road method” deals with the road definition. It can be perfectly “Flat”, “Opencrg” or “External” (defined within the simulation environment). If “Opencrg” is selected, the “Road name” corresponding to the crg file must be included.
- The “Contact method” can be “Smooth road”, generally adopted for handling simulation or if the wavelength of the unevennesses is much longer than the length of the contact patch, “Moving road”, used to simulate a roller bench, or “Enveloping”, used to calculate an effective road surface for the short wavelength obstacles. Focusing on the road and the contact methods, not every combination is possible: “External” road option is indeed not available in combination with the “Enveloping” contact mode.
- The “Dynamics” option allows to progressively increase the model complexity. “Steady-state” option implies no dynamic behavior of the tyre. The “Relaxation behaviour” option includes the empirically determined tyre relaxation length. The “Non-linear relaxation behaviour” option uses the compliance of the tyre carcass to determine the lag. This approach allows to represent the lag dependency of slip, vertical load and velocity. Both the relaxation behaviour modes are able to capture phenomena up to 10 Hz. Adopting the “Rigid-ring” option, equivalent springs and dampers are introduced between the rim and the belt and inertial properties in the “Tyre property file” are considered. The tyre dynamic behavior is accurately modelled up to 100 Hz.
- The “Slip forces” option deals with the longitudinal and lateral tyre forces and their combination. The model can manage the force components as standalone or introduce a combined slip formulation.